Comprehensive analysis of cellular specializations that initiate parallel auditory processing pathways in mice

Junzhan Jing[1, 2,*], Ming Hu[1, 2, *], Tenzin Ngodup[3,*], Qianqian Ma[1, 2], Shu-Ning Natalie Lau[1, 2], Cecilia Ljungberg[1, 4], Matthew J. McGinley[1, 2], Laurence O. Trussell[3, †] and Xiaolong Jiang[1, 2, 5†]

Summary

The cochlear nuclear complex (CN) is the starting point for all central auditory processing and comprises a suite of neuronal cell types that are highly specialized for neural coding of acoustic signals. To examine how their striking functional specializations are determined at the molecular level, we performed single-nucleus RNA sequencing of the mouse CN to molecularly define all constituent cell types and related them to morphologically- and electrophysiologically-defined neurons using Patch-seq. We reveal an expanded set of molecular cell types encompassing all previously described major types and discover new subtypes both in terms of topographic and cell-physiologic properties. Our results define a complete cell-type taxonomy in CN that reconciles anatomical position, morphological, physiological, and molecular criteria. This high-resolution account of cellular heterogeneity and specializations from the molecular to the circuit level illustrates molecular underpinnings of functional specializations and enables genetic dissection of auditory processing and hearing disorders with unprecedented specificity.

[1]Jan and Dan Duncan Neurological Research Institute at Texas Children's Hospital, Houston, TX, USA.
[2]Department of Neuroscience, Baylor College of Medicine, Houston, TX, USA
[3]Oregon Hearing Research Center and Vollum Institute, Oregon Health and Science University, Portland, OR, USA
[4]Department of Pediatrics, Baylor College of Medicine, Houston, TX, USA
[5]Department of Ophthalmology, Baylor College of Medicine, Houston, TX, USA
*Equally contributed
[†]Correspondence to xiaolonj@bcm.edu, trussell@ohsu.edu

Keywords: Cochlear nucleus, snRNA-seq, Patch-seq, phenotype, bushy cells, stellate cells, octopus cells, fusiform cells, interneurons, transcriptome.

Introduction

Auditory signals are encoded by cochlear hair cells and transmitted to the first processing station in the brain, the cochlear nuclear complex (CN). From the diversity of CN cell types arises a remarkable richness of neural circuitry and the foundation of all higher-level parallel auditory pathways (Oertel et al., 2009). Classical studies, using histology, in-vivo and in-vitro recording, and pathway tracing, have identified the general classes of CN projection neurons: the bushy, T-stellate, fusiform, and octopus cells, which each carry distinct ascending signals needed for high-level sound processing (Palmer, 1987; Rhode and Greenberg, 1992; Yin et al., 2019). Multiple classes of interneurons within CN determine the pattern and magnitude of signals that ascend through the neuraxis (Yin et al., 2019). We term these classes of projection and interneurons "established cell classes". However, numerous lines of evidence suggest that the established cell classes do not capture the true range of cell types and their functions, thus preventing a full understanding of central auditory processing, even at its initiation. For example, in vivo recordings document diverse patterns of acoustic response within a given class of neurons, suggesting an underlying cellular diversity (Blackburn and Sachs, 1989; Doucet and Ryugo, 2006; Hancock and Voigt, 2002a). Moreover, recent in vitro physiological studies using Cre mouse lines and optogenetics have suggested the existence of previously undescribed cell types in CN (Ngodup et al., 2020; Xie and Manis, 2014). Because a comprehensive molecular census of CN cell types is lacking, and cell-type specific markers are few, the complete contribution of any given cell type in CN to sound representations in higher brain regions is unknown. Moreover, it is uncertain even whether existing definitions of cell classes have sufficient resolution to account for the variety of downstream anatomical projections and physiological responses.

Recent advances in single-cell RNA sequencing offer a new approach to define cell types in the brain (Macosko et al., 2015; Saunders et al., 2018; Zheng et al., 2017), and transcriptomically defined cell types ('T-type') are now available for many brain regions (Callaway et al., 2021; Kozareva et al., 2021; Mickelsen et al., 2019; Tasic et al., 2018). However, a list of molecularly defined cell types

alone is insufficient; rather what is needed is to relate each T-type to the established cell types with accepted morphological and electrophysiological criteria ('ME-type'), a correspondence essential to inferring and exploring their putative functions. Indeed, it is likely that the definition of a "cell-type" likely requires such an integrated approach (Mukamel and Ngai, 2019). We therefore employed unbiased single-nucleus RNA sequencing (snRNA-seq) analysis of CN to generate a transcriptomic taxonomy of cell types, and then related these molecular cell types defined by transcriptomic profiling with established CN types using Patch-seq (Cadwell et al., 2016), a method that allowed multimodal analysis of individual cells. Combined with validation methods including fluorescent in situ hybridization (FISH) and transgenic mouse lines, we established a clear correspondence between molecularly defined cell types and all previously established CN cell types. Importantly, we also find that transcriptomic classifications can be used to reveal hitherto unresolved distinctions in the morphology and physiology of cell types, indicating conventional categories may not be robust enough to account for true cellular heterogeneity (Gates et al., 1996; Hancock and Voigt, 2002b). Moreover, the molecular characterization of neurons with well-studied physiological phenotypes permits a comprehensive analysis of the molecular underpinnings of their biophysical and synaptic features.

Results

Identification of transcriptionally distinct cell populations in mouse CN

To investigate transcriptional and cellular heterogeneity within the CN, we performed RNA sequencing on individual nuclei isolated from CN of male and female C57BL/6 mice (postnatal day (P) 22-28) (Figure S1A). Our final dataset contained 61,211 CN nuclei (Methods; Method S1 and Data S1), and analysis of sequence reads revealed ~4,000 uniquely detected transcripts from ~1,900 genes for each nucleus. Following data integration, unsupervised dimensionality reduction techniques identified 14 major transcriptionally distinct cell populations (Figure S1B). By inspection of known markers, we identified all non-neuronal cell types in CN (Figure S1C; Table S1). Using the pan-neuronal marker *Snap25*, we identified 31,639 neuronal nuclei expressing either the gene for vesicular glutamate

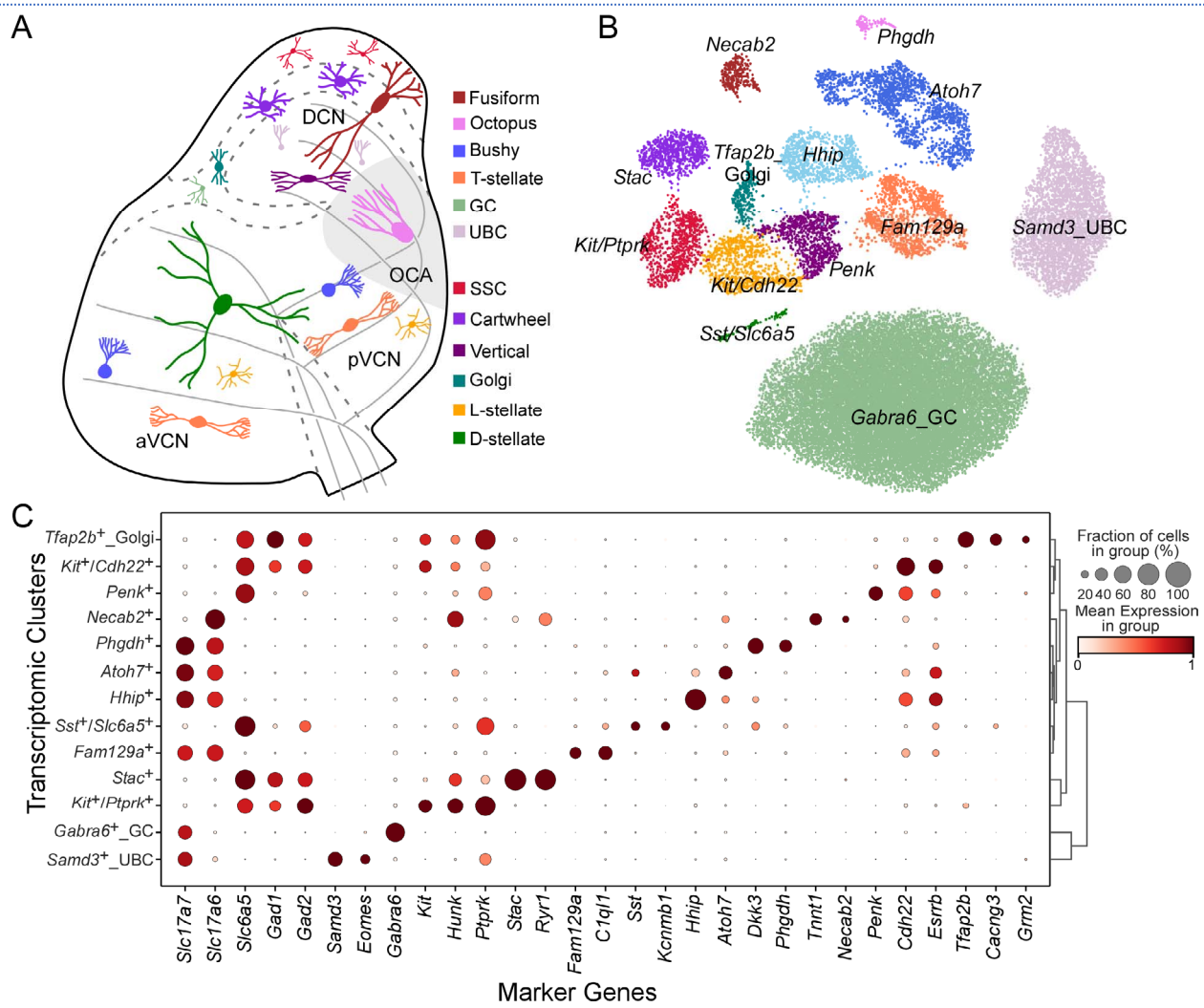

Figure 1. Comprehensive transcriptional profiling of cell types across the mouse CN. (**A)** Depiction of neuronal cell types across mouse CN, colored by cell type identity. (**B)** UMAP visualization of 31,639 nuclei from CN neurons clustered by over-dispersed genes, colored by cluster identity. Each cluster labeled by key marker genes. **(C)** Right: dendrogram indicating hierarchical relationships between clusters. Left: dot plot of scaled expression of selected marker genes for each cluster shown in (**B**); see Table S1. Circle size depicts percentage of cells in the cluster in which the marker was detected (≥ 1 UMI), and color depicts average transcript count in expressing cells. See Figure S1 and Data S1 for more technical details and annotations.

transporters *Slc17a7* or *Slc17a6* or the gene for the glycine transporter *Slc6a5*, thus separating glutamatergic and glycinergic populations (Figure S1). Clustering analysis of neuronal nuclei resulted in 13 molecularly distinct populations including seven glutamatergic/excitatory clusters (*Slc17a7*$^+$ and/or *Slc17a6*$^+$) and six glycinergic/inhibitory clusters (*Slc6a5*$^+$, Figure 1B). Based on known markers, we assigned three clusters to known CN cell types. Two glutamatergic clusters that expressed only *Slc17a7* (not *Slc17a6*) were either enriched with *Gabra6*, a marker gene for granule cells (GCs)(Campos et al., 2001; Varecka et al., 1994), or with *Tbr2*/*Eomes* and *Samd3* (Figure 1B-D), gene markers for unipolar brush cells (UBCs) (Englund et al., 2006; Kozareva et al., 2021), thus

corresponding to GCs and UBCs in CN, respectively (Figures 1B-C, S1D). The UBC cluster was further validated with RNA fluorescent in situ hybridization (FISH) staining for *Samd3* (Figure S1D) and characterized by graded and inversely correlated expression of glutamate excitatory signaling pathways and inhibitory pathways, reminiscent of UBCs in cerebellum (Figure S1E) (Borges-Merjane and Trussell, 2015; Guo et al., 2021; Kozareva et al., 2021). One glycinergic cluster was enriched with *Grm2* (Figure 1C), a marker gene for Golgi cells in CN (in addition to UBCs) (Irie et al., 2006; Yaeger and Trussell, 2015), thus corresponding to auditory Golgi cells (Figure 1B-C). Differentially expressed gene (DEG) analysis identified *Cacng3* and *Tfap2b* as more specific marker genes for auditory Golgi cells (Figure 1B-C), which were validated with FISH (Figure S1F). Other major clusters are unknown with respect to their correspondences to well-studied CN cell types (Figure 1A), but could be labeled by one or two candidate gene markers identified via DEG analysis (Figure 1B-C; Table S1).

Molecular profiles of CN excitatory neurons

To identify the unknown clusters with respect to known CN cell types, we performed Patch-seq, starting with four major excitatory projection neurons, bushy, T-stellate, octopus, and fusiform cells (Rhode and Greenberg, 1992), targeting each by their known anatomical location aided by transgenic mouse lines (see Methods). Their characteristic electrophysiological responses to current injections were recorded, cytosol and nucleus mRNA were extracted and reverse transcribed, and the resulting cDNA was sequenced (Data S1, Methods). The morphology of each neuron was post hoc recovered and reconstructed. Based on their stereotypical morphological/electrophysiological properties, each neuron could be readily identified and assigned to a type, a process we term “expert classification” (Figures 1A, 2A-B; Table S2) (Manis et al., 2019). To validate expert classification and support cell-type assignment of each Patch-seq neuron, we used a random forest classifier or clustering-based k-means classifier based on either electrophysiology or morphology to distinguish between any two types of CN excitatory neurons as labeled manually, resulting in successful separation of almost all cell type pairs (Figures 2C-D, Data S2), supporting our expert classification. UMAP projection of these

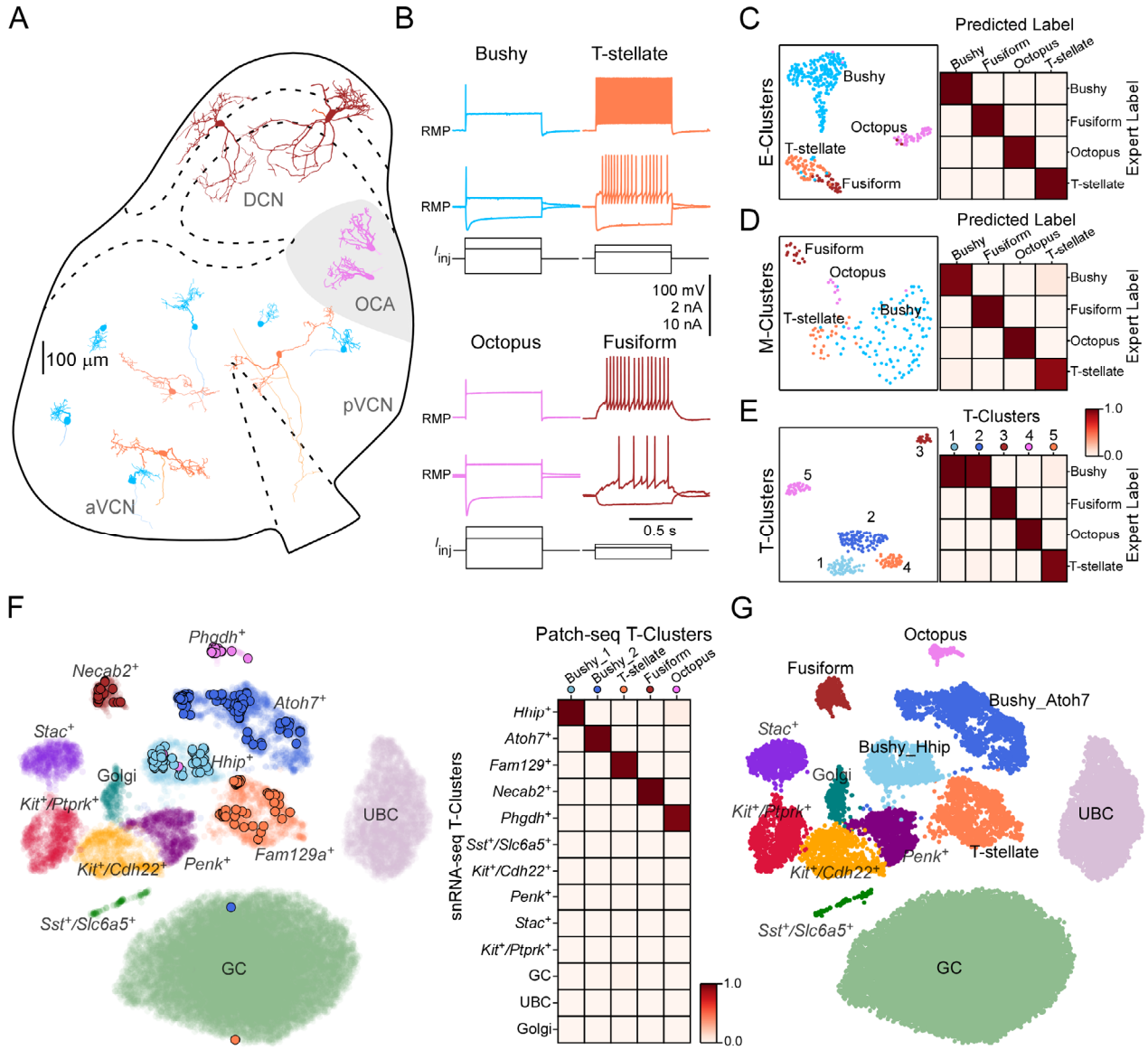

Figure 2. Using Patch-seq to identify transcriptomic correspondences for excitatory neurons. (**A**) Representative morphology of excitatory neurons in mouse CN (sagittal view), colored by cell type identity. (**B**) Example responses of CN excitatory cell types to current steps. Bottom traces show the injected currents. Scalebar: 100 mV for potential, 2 nA for injected currents for all cells except octopus cells (10 nA). (**C**) Left: UMAP visualization of 404 CN excitatory neurons clustered by over-dispersed physiological features (E-cluster), colored by expert cell type. n=243 for bushy, n=67 for T-stellate, n=58 for octopus, n=36 for fusiform. Right: Confusion matrix shows performance (an average of 99.2% accuracy) by the cell-type classifier trained with physiological features. (**D**) Left: UMAP visualization of 157 CN excitatory neurons clustered by over-dispersed morphological features (M-cluster), colored by expert cell type. n=105 for bushy, n=16 for T-stellate, n=10 for octopus, n=26 for fusiform. Right: Confusion matrix shows the performance (an average of 95.5% accuracy) by the classifier trained with morphological features. (**E**) Left: UMAP visualization of 293 Patch-seq excitatory neurons clustered by over-dispersed genes, colored by transcriptomic cluster (T-cluster). Right: the matrix shows proportion of Patch-seq cells assigned to a specific cell type (the expert classification) in each T-cluster. All cells in T-cluster 1 (n= 67/67) and almost all cells in T-cluster 2 (n=111/113) are bushy cells; all cells in T-cluster 3 are fusiform cells (n=22/22); all cells in T-cluster 4 are octopus cells (n=43/43); almost all cells in T-cluster 5 are T-stellate cells (n=46/48). (**F**) Left: Patch-seq cells (n=187) mapped to snRNA-seq UMAP space as shown in Figure 1B. Right: matrix shows proportion of Patch-seq cells assigned to each T-cluster in (**E**) mapped to one of 13 clusters in UMAP space. (**G**) Annotation of each molecular cell type with established morpho/electrophysiological types in CN. See Data S2 for more details.

Patch-seq cells resulted in five transcriptomic clusters, and the cells labeled as the same type clustered together and were only rarely confused with another cluster (Figure 2E), except for bushy cells, which

clearly fell into the two prominent clusters. Using the gene expression profiles, we mapped these Patch-seq neurons to the transcriptomic clusters identified via snRNA-seq (Figure 1B)(Cadwell et al., 2020; Scala et al., 2018), demonstrating close correspondence in the two datasets and identifying transcriptomic clusters for the established excitatory cell types (Fig 2F-G). Importantly, those Patch-seq bushy cells clustering together as Cluster 1 in Patch-seq UMAP space (Figure 2E) were all mapped

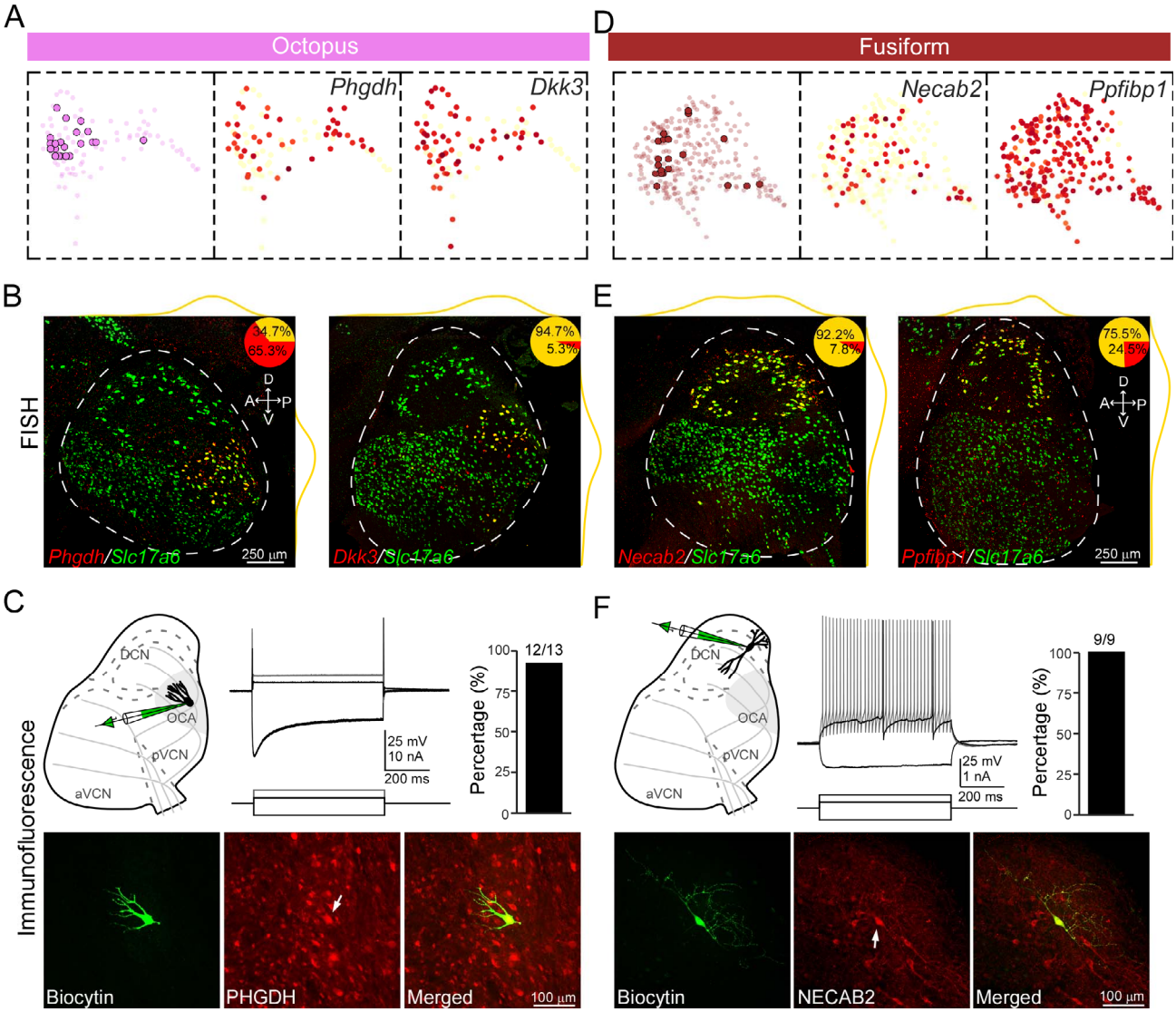

Figure 3. **Novel marker genes for CN excitatory neurons**. (**A)** UMAP visualization of the *Phgdh*$^+$ cluster (n=88) and all Patch-seq octopus cells positioned on UMAP space (left). Middle and Right: UMAP visualization of normalized expression of two discriminatory markers for octopus cell cluster. **(B**) FISH co-staining for *Slc17a6* and *Phgdh* (left), or *Slc17a6* and *Dkk3* (right) in sagittal CN sections. D, dorsal; V, ventral; A, anterior; M, posterior. Inset pie charts show proportion of double-labeled cells in single-labeled cells (*Phgdh*$^+$ or *Dkk3*$^+$). Yellow lines along images show density of double-labeled neurons along two axes of CN. **(C)** Top-left: diagram showing patch recording and labeling with biocytin for octopus cells. Top-middle: example responses of an octopus cell to current steps. Top-right: proportion of octopus cells immunopositive for Phgdh. Bottom: example octopus cell filled with biocytin (green) positive for Phgdh (red). **(D)** UMAP visualization of *Necab2*$^+$ cluster (n=274) and all Patch-seq fusiform cells positioned on UMAP space (left). Middle and Right: UMAP visualization of normalized expression of two discriminatory markers for fusiform cells. **(E)** FISH co-staining for *Slc17a6* and *Necab2* (left), or *Slc17a6* and *Ppfibp1* (right) in CN sagittal sections. Inset pie charts show proportion of double-labeled cells in single-labeled cells (*Necab2*$^+$ or *Ppfibp1*$^+$). **(F)** Top-left: diagram showing patch recording and labeling for fusiform cells. Top-middle: example responses of a fusiform cell to current steps. Top-right: proportion of fusiform cells immunopositive for Necab2. Bottom: example fusiform neuron filled with biocytin (green) shows positive for Necab2 (red).

to the *Hhip*$^+$ cluster (Figure 2F), while almost all bushy cells in Cluster 2 (Figure 2E) were mapped to the *Atoh7*$^+$ cluster (Figure 2F). Thus, our analysis not only reveals a strong congruence across three modalities in CN excitatory neuron classification, but also molecular heterogeneity among bushy cells (see below).

DEG analysis was performed to find marker genes for each cell type (or cluster, Table S1), while FISH and immunohistochemistry validated their expression and cell type-specificity with the known anatomical location of each cell type (Methods). With these approaches, a suite of novel discriminatory markers was identified for octopus cells (Figures 3A-B, S2-3, Data S3, and Table S1), a major projection neuron (Lu et al., 2022; McGinley et al., 2012). Antibodies to one of these markers, Phgdh, labeled neurons (i.e., cells with a large soma) restricted to the octopus cell area (OCA) (Figure S3C1). Indeed, when patch-clamp recordings from the OCA to label octopus cells with biocytin and *post hoc* immunostaining performed for Phgdh, most labeled cells (12/13) were immunopositive for Phgdh (Figure 3C). Similarly, *Necab2* and *Pbfibp1*, among other genes, were confirmed as major markers for fusiform cells of the DCN (Figures 3D-E, S2B, D, S3B, Data S3 and Table S1). Immunostaining combined with patch-clamp analysis provided translation-level evidence for *Necab2* as a highly selective marker for the entire population of fusiform cells (Figure 3F, Figure S3C2).

Two molecular subtypes of bushy cell

In anatomical and physiological studies, bushy cells have been divided into two populations, spherical and globular bushy cells (SBCs and GBCs, respectively), based largely on differences in their axonal projections (Lauer et al., 2013). Generally, SBCs are located anteriorly in VCN while GBCs are more posterior (Yin et al., 2019). Some investigators have proposed two subtypes of SBCs (small and large), based on their axonal targets in lateral and medial superior olive (Yin et al., 2019), although it is not clear how distinct are these populations. Our initial analysis identified two transcriptomically distinct bushy cell populations marked by high levels of *Hhip* or *Atoh7* (*Atoh7*$^+$ and *Hhip*$^+$, Figure 4A), which

may correspond to SBCs and GBCs. We therefore performed FISH staining for *Atoh7* and *Hhip* to determine the spatial location of these cell groups. Given that *Sst* is specifically expressed in the *Atoh7*

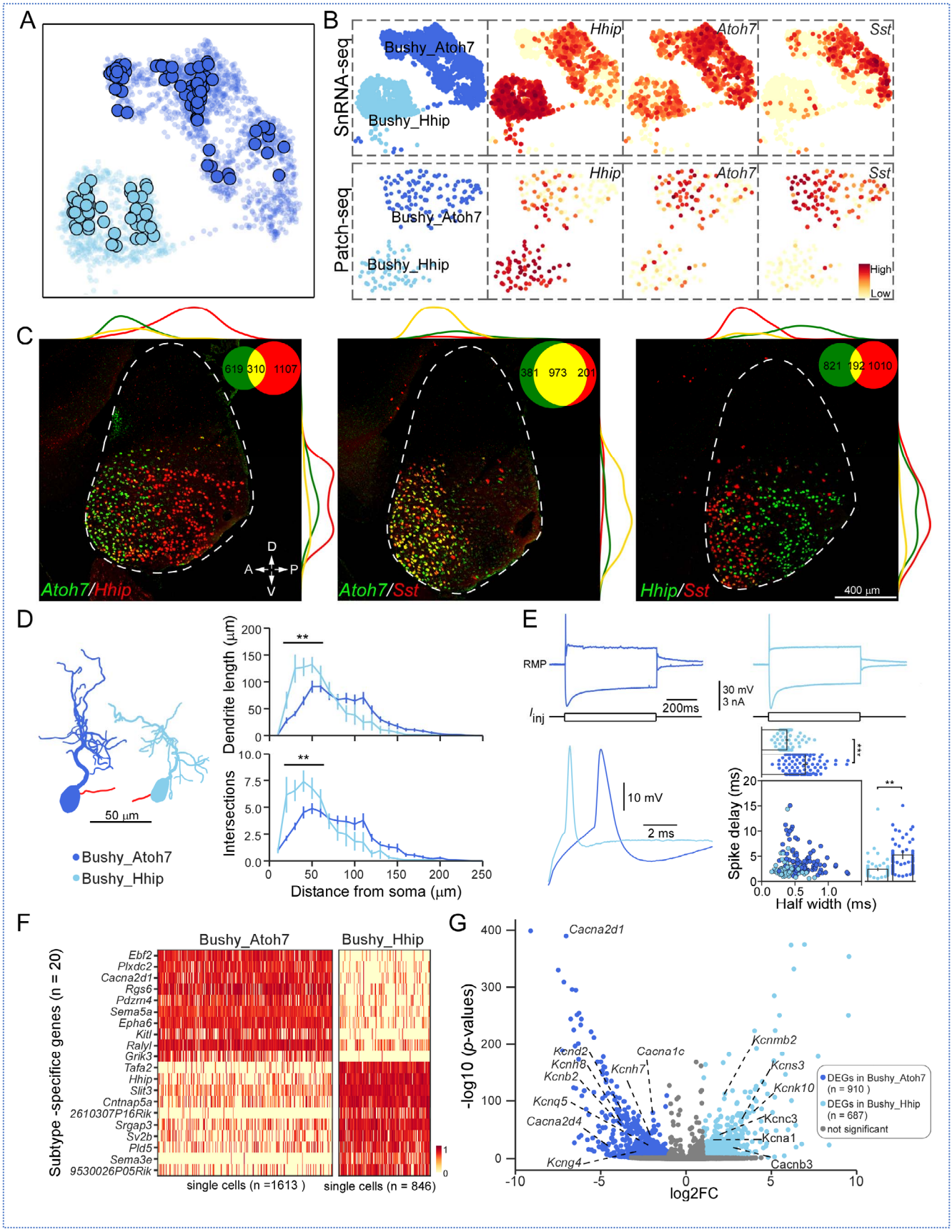

Figure 4. Two molecular subtypes of bushy cell. (**A)** UMAP visualization of *Hhip*$^+$ and *Atoh7*$^+$ clusters and distribution of Patch-seq bushy cells in UMAP space, colored by cluster. (**B**) UMAP visualization of two bushy cell clusters and normalized expression of their marker genes, *Hhip*, *Atoh7,* and *Sst*. Top: snRNA-seq, Bottom: Patch-seq. (**C)** FISH co-staining for *Atoh7* and *Hhip* (left), *Atoh7* and *Sst* (middle), or *Hhip* and *Sst* (right) in CN sagittal sections. Insets show total number of single-labeled cells and double-labeled cells. The lines along images show density of single-labeled or double-labeled cells along two axes of CN. Scalebar applies to all images. **(D)** Left: A representative morphology of *Hhip*$^+$ or *Atoh7*$^+$ bushy cell. Axon in red is truncated. Right: Sholl analysis of *Hhip*$^+$ or *Atoh7*$^+$ bushy cell dendrites. $^{**}p < 0.01$, with two-way mixed model ANOVA. (**E)** Top: example responses of *Atoh7*$^+$ bushy cell (left) or *Hhip*$^+$ bushy cell (right) to hyperpolarized current step and near-threshold depolarizing current step. Bottom-left: individual APs from the *Hhip*$^+$ and *Atoh7*$^+$ cells shown above, aligned with onset of depolarizing current. Bottom-right: two most-discriminating features for *Hhip*$^+$ cells and *Atoh7*$^+$ cells, spike delay and spike duration (half-width). Plotting spike delay against half-width separates the majority of *Hhip*$^+$ cells from *Atoh7*$^+$ cells. $^{**}p < 0.01$; $^{***}p < 0.001$; t-test. (**F**) Heat map showing normalized expression of the top 20 DEGs for two subtypes. Scalebar: Log2 (Expression level). The cell number in each subcluster is indicated below the figure. (**G**) Volcano plot showing the log2 fold change (log2FC) and -log10(p-values) of detected genes comparing two subtypes. Among DEGs are 14 genes encoding voltage-gated ion channels. See Figure S4 for more analysis.

subtype rather than the *Hhip* subtype (Figure 4B) and is expressed preferentially in SBCs rather than GBCs in VCN (Romero, 2021), we also performed FISH labeling for *Sst* and *Atoh7*, and for *Sst* and *Hhip*. Both *Atoh7* and *Hhip* signals were almost exclusively restricted to VCN (Figure 4C), in line with our snRNA-seq data (Figure S2A-B, S2D) and Allen ISH data (Data S3). Furthermore, *Atoh7*$^+$ cells were predominantly localized in the rostral anterior VCN (AVCN), while *Hhip*$^+$ cells densely populated the posterior VCN (PVCN) and caudal AVCN, and less so rostrally (Figure 4C), similar to SBCs and GBCs in terms of their typical locations (Lauer et al., 2013; Martin, 1981; Webster and Trune, 1982). In addition, *Sst* signals mostly overlapped with *Atoh7* and much less so with *Hhip*, and double-labeled cells (*Sst*$^+$*/Atoh7*$^+$and *Sst*$^+$*/Hhip*$^+$) were restricted to rostral AVCN (Figure 4C), further validating two molecularly distinct bushy cell subtypes marked by *Atoh7* or *Hhip*. Based on the preferential location of each molecular subtype with differential *Sst* expression, the *Atoh7* subtype may correspond to SBCs, while the *Hhip* subtype may correspond to GBCs.

To determine if molecular subtypes of bushy cells are associated with unique physiological and morphological features, we examined the properties of each Patch-seq cell that was assigned to the *Hhip* or *Atoh7* subtype. Two subtypes exhibited similar soma size and shape, but there were differences in their dendritic arborization (Figure 4D and Table S3). While the majority of *Hhip* bushy cells have only one primary dendrite (85%, 17 out of 20 cells), more than half of *Atoh7* bushy cells have two or even three primary dendrites (~53%, 27 out of 51 cells), each with its own secondary and filamentous branches (Table S3). In addition, *Hhip* bushy cells had short dendritic trunks capped with

relatively compact dendritic tufts, while *Atoh7* bushy cells had longer dendritic trunks that bifurcated and sent off diffuse, thin dendritic processes (Figure 4D and Table S3). Dendrites of either *Atoh7* bushy cells or *Hhip* bushy cells were not oriented in any particular direction within the VCN.

Electrophysiologically, *Hhip* and *Atoh7* bushy cells are largely distinguishable exhibiting significant differences in numerous features with spike delay and half-width being the most prominent (Figure 4E, S4A, Table S3). Bushy cells are biophysically specialized for encoding precise timing by expressing a prominent low-threshold K^+ current and a hyperpolarization-activated current, which together bestow single-spike firing, and low input resistance and short time constants enabling brief and sharply timed synaptic responses (Cao et al., 2007; Manis and Marx, 1991; Rothman and Manis, 2003). *Hhip* bushy cells had lower input resistances and shorter membrane time constant (thus shorter delays to firing onset), deeper and quicker voltage sags in responding to hyperpolarizing currents, and fewer spikes in response to suprathreshold depolarizing currents than *Atoh7* bushy cells (Figure 4E and Table S3), indicative of larger near-rest outward current with faster kinetics. These properties were paralleled by higher expression of ion channels active in that voltage range (*Kcna1, Hcn1)* in *Hhip* bushy cells (Figure 4F-G, Figure 7B)(Cao and Oertel, 2011; Cao et al., 2007). In addition, *Hhip* bushy cells had faster depolarization and repolarizations (larger dV/dt) resulting in narrower spikes (Figure 4E and Table S3), matching their enrichment in Kv3 (*Kcnc3*) (Figure 4F-G), a potassium channel enabling brief APs for auditory neurons to follow high-frequency input with temporal precision (Brew and Forsythe, 1995; Perney and Kaczmarek, 1997; Wang et al., 1998a). In contrast, *Atoh7*$^+$ cells had a higher expression of Kv2 (*Kcnb2*) in addition to a lower expression of Kv1 (Figure 4F-G, Figure 7B), which may enable them to fire more spikes than *Hhip*$^+$ cells (Johnston et al., 2008).

However, even within these two main subtypes of bushy cells, further bushy cell-type molecular heterogeneity was observed, including three subpopulations in *Atoh7*$^+$ bushy cells (*Atoh7*/*Dchs2*,

Atoh7/*Tox*, and *Atoh7*/*Sorcs3*) (Figure S4B) and two subpopulations in *Hhip*$^{+}$ bushy cells (*Hhip*/*Calb1*

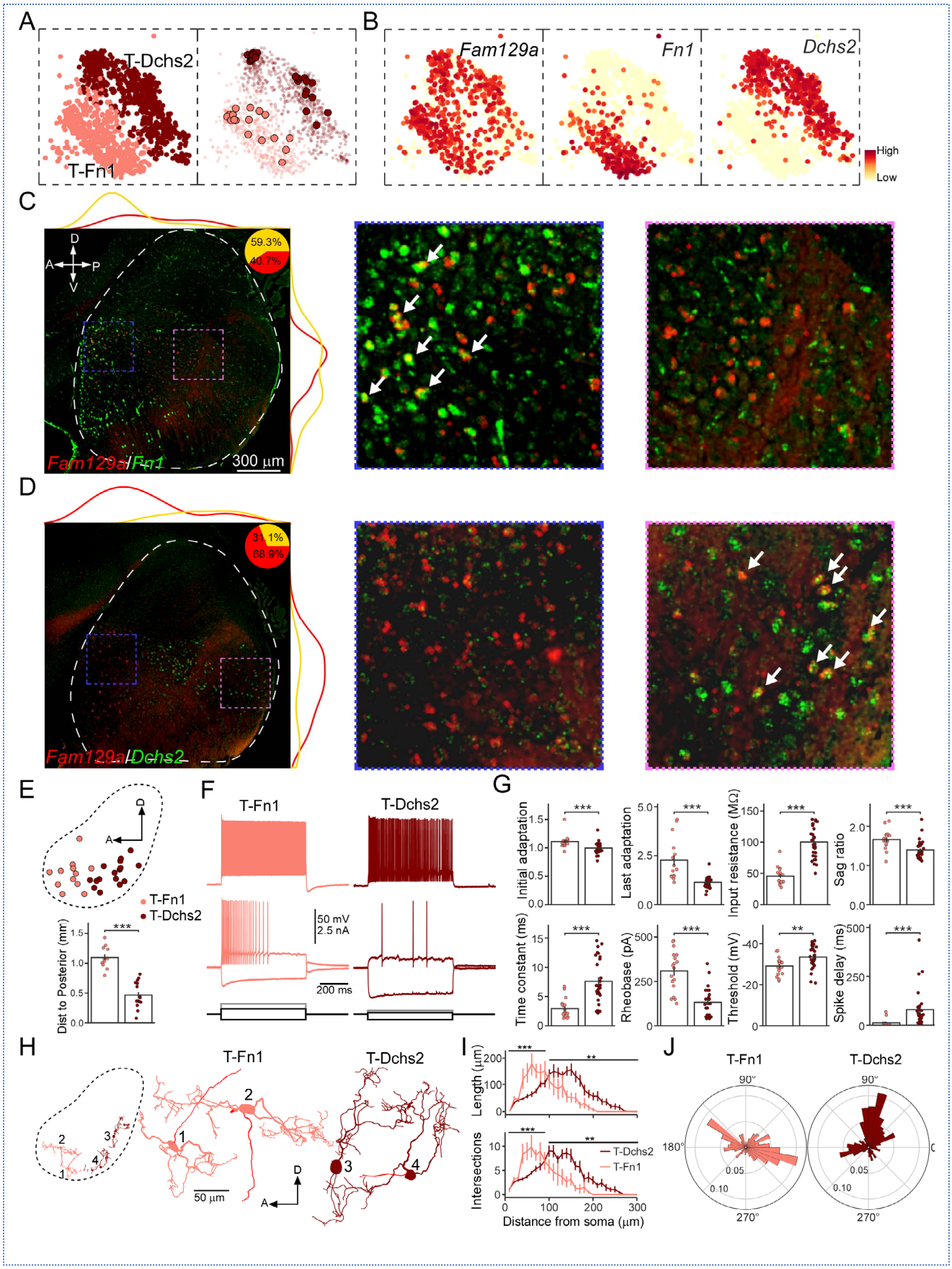

Figure 5. **Two subtypes of T-stellate cells**. (**A**) Left: UMAP visualization of two subclusters of *Fam129a*$^+$ neurons (marked by high expression of *Dchs2* or *Fn1*:T-Fn1 and T-Dchs2), colored by subcluster. Right: All Patch-seq cells mapped to *Fam129a*$^+$ cluster on left. (**B**) UMAP visualization of normalized expression of discriminatory markers for all T-stellate cells and its two subclusters (*Fam129a*, *Fn1*, *Dchs2*). (**C**) FISH co-staining for *Fam129a* and *Fn1* in CN sagittal section. Inset pie chart: proportion of double-labeled cells in single-labeled *Fam129a*$^+$ cells. The lines along images show density of single-labeled or double-labeled neurons along the two axes of CN. Two images on right are zoom-in views of boxed regions on left. Arrows indicate double-labeled cells. (**D**) FISH co-staining for *Fam129a* and *Dchs2* in a CN sagittal section. Two images on right are zoom-in views. (**E**) Top: 2D spatial projection of Patch-seq T-Fn1 cells and T-Dchs2 cells to a sagittal view of CN, colored by the subtypes. Bottom: Comparing the distance to CN posterior edge between T-Fn1 and T-Dchs2. ***p< 0.001, t-test. (**F**) Example responses of two subtypes (T-Fn1, T-Dchs2) to current steps. (**G**) Electrophysiological features between two T-stellate subtypes. **p< 0.01, ***p< 0.001 with the t-test.(**H**) Left: Representative morphology of two *Fn1*$^+$ cells and two *Dchs2*$^+$ cells in CN sagittal view (soma locations). Axons in red. Right: zoom-in of four T-stellate cells shown on left. (**I**) Sholl analysis of T-Fn1 and T-Dchs2 dendrites. **p< 0.01, ***p< 0.001, two-way mixed model ANOVA. (**J**) The polar distribution histograms of the termination points of dendritic branches with respect to soma of T-Fn1 and T-Dchs2. The terminal distribution of T-Fn1 has two peaks at 145° and 345°, while the terminal distribution of T-Dchs2 has two peaks at 75° and 195°. p<0.001 for difference between the distributions with Kolmogorov-Smirnov statistic.

and *Hhip*/*Galnt18*) (Figure S4F). To support these subpopulations, we examined the properties of Patch-seq cells that were assigned to each subcluster, including their anatomical locations. In *Atoh7*$^+$ bushy cells, *Atoh7*/*Dchs2* cells appear to be restricted to be the nerve root area and PVCN, while *Atoh7*/*Sorcs3* cells and *Atoh7*/*Tox* cells appear to have less spatial preferences (Figure S4C). Electrophysiologically, *Atoh7*/*Dchs2* cells had distinct firing properties from *Atoh7*/*Sorcs3* cells and *Atoh7*/*Tox* cells, while *Atoh7*/*Sorcs3* and *Atoh7*/*Tox cells* shared similar firing properties (Figure S4D, Table S3). Morphologically, *Atoh7*/*Dchs2* cells in general had the longest dendritic trunks (stem) among three subclusters (Figure S4E, Table S3). In *Hhip*$^+$ bushy cells, *Hhip*/*Calb1* cells were preferentially localized in the posteroventral VCN, while *Hhip*/*Galnt18* cells were preferentially localized in the dorsoanterior VCN (Figure S4G). *Hhip/Calb1* cells had distinct firing properties from *Hhip*/*Galnt18* (Figure S4H, Table S3). In addition, the *Hhip/Calb1* cells in general had the shorter dendritic projections, but more complex dendritic tufts than *Hhip*/*Galnt18* cells (Figure S4I, Table S3). These analyses support functionally and topographically distinct subpopulations within each bushy cell subtype.

Two subtypes of T-stellate cell

Patch-seq mapping indicated that the *Fam129a*$^+$ cluster corresponds to T-stellate cells (Figure 2F-G). However, this cluster comprised two visibly separate lobes on the UMAP, suggesting two sub-populations of T-stellate cells (Figure 1B, 5A). With more than 1100 DEGs identified between two

putative sub-populations, we focused on *Dchs2* and *Fn1*, two top DEGs expressed almost exclusively in one of the two sub-populations with high coverage (Figures 5A-B, S5A-B). To validate their expression and determine how well these two genes separate T-stellate cell subpopulations, we performed FISH co-labeling for *Fam129a* and *Dchs2*, and for *Fam129a* and *Fn1*. *Fam129a* signals were restricted to VCN (Figure 5C-D) and almost exclusively expressed in excitatory neurons (data not shown), thus validating *Fam129a* as a general marker for T-stellate cells (Figures 2F, S2A-B, S2D, S5C, Data S3). Only a subset of *Fam129a*$^+$ neurons co-expressed *Fn1* (*Fam129a*$^+$/*Fn1*$^+$), and these double-labeled neurons were exclusively localized in the AVCN (Figure 5C). Similarly, only a subset of *Fam129a* $^+$ neurons co-expressed *Dchs2*, and these *Fam129a*$^+$/*Dchs2*$^+$ neurons were restricted to the VCN nerve root area and to PVCN (Figure 5D). These data suggest two spatially separated subpopulations of T-stellate cells. To substantiate this conclusion, we examined the location of Patch-seq cells assigned as T-stellate cells. These cells were mapped to either *Dchs2*$^+$ subcluster or the *Fn1*$^+$ subcluster almost equally (Figure 5A), allowing for an unbiased comparison of their spatial locations. *Fn1*$^+$ T-stellate cells were restricted to the AVCN, while *Dchs2*$^+$ T-stellate cells were predominantly localized in the PVCN and the nerve root area of the VCN. Importantly, these two subpopulations were spatially non-overlapping in the VCN (Figure 5E), indicating that T-stellate cells could be classified into two subtypes by their anatomical locations.

Two T-stellate cell subtypes were further supported by their distinct morpho/electrophysiological properties. While both *Fn1*$^+$ or *Dchs2*$^+$ T-stellate cells exhibited typical morphology of T-stellate cells (Figure 5H) (Oertel et al., 1990), there were subtle differences in their dendritic arborization (Table S4). The dendrites of *Fn1*$^+$ cells in general branched earlier and more profusely around the soma compared to that of *Dchs2*$^+$ cells, while the dendrites of *Dchs2*$^+$ cells arborized more extensively away from the soma with more branched, complex endings (Figure 5H-I, Table S4). In addition, the major dendrites and the terminal arbors of *Fn1*$^+$ and *Dchs2*$^+$ cells had distinct preferential angles with respect to their soma (Figure 5J). Given that the major dendrites and the terminal arbors of T-stellate cells in

general run parallel to tonotopically arranged ANFs (Figure 5H) (Doucet and Ryugo, 1997; Xie and Manis, 2017) whose direction in each subregion is well-established, such differences between two subtypes reflect their distinct anatomical locations in the VCN, further substantiating the conclusion that the subtypes of T-stellate cells are defined by their anatomical locations.

Both *Fn1*$^+$ and *Dchs2*$^+$ T-stellate cells fired tonically as reported previously (Cao and Oertel, 2011; Lin and Xie, 2019), but they were physiologically distinguishable with differences in numerous features (Figure 5F-G, S5E, Table S4). Among these, spike delay (latency to first spike at rheobase), time constant, and input resistance alone separated almost all *Dchs2*$^+$ cells from *Fn1*$^+$ cells (Figure S5D). Such striking physiological distinctions were well aligned with the top DEGs distinguishing two subtypes being dominated by numerous genes encoding potassium channels (Figure S5A-B). Notably, *Fn1*$^+$ cells were enriched for expression of multiple leak K^+ channels including K_{2P}9.1 (*Kcnk9*), K_{2P}10.1 (*Kcnk10*), and K_{2P}12.1 (*Kcnk12*) and subthreshold-operating Kv channels including Kv7.4 (*Kcnq4*), Kv10.2 (*Kcnh5*) and Kv12.1 (*Kcnh8*), matching their lower input resistance and smaller time constant compared to *Dchs2*$^+$ cells (Bauer and Schwarz, 2018; Zou et al., 2003)(Figures 5G, S5B). In contrast, *Dchs2*$^+$ cells were enriched for expression of Kv2 and Kv3 (*Kcnb2*, *Kcnc2*), two potassium channels required for auditory neurons to maintain high-frequency repetitive firing (Johnston et al., 2008; Rudy and McBain, 2001; Wang et al., 1998a), matching their more 'fast-spiking' phenotype (no adaption) compared to *Fn1*$^+$ cells.

Molecular profiles of inhibitory cell types in CN

Among the six glycinergic/inhibitory clusters (including Golgi cells), four expressed both *Slc6a5* and genes for GABA synthetic enzymes (*Gad1/2*, Figure 1C), consistent with dual transmitter phenotypes described in CN (Apostolides and Trussell, 2014; Kolston et al., 1992; Yaeger and Trussell, 2015). Other two clusters, *Slc6a5*$^+$/*Sst*$^+$ and *Penk*$^+$ cluster, expressed only *Slc6a5* and no *Gad1/2*, indicative of pure glycinergic populations (Figure 1C). Notably, the *Slc6a5*$^+$/*Sst*$^+$ cluster likely corresponds to D-

stellate cells in VCN, a known pure glycinergic population with specific expression of *Sst* (Kolston et al., 1992; Ngodup et al., 2020). A definitive correspondence of glycinergic clusters to established

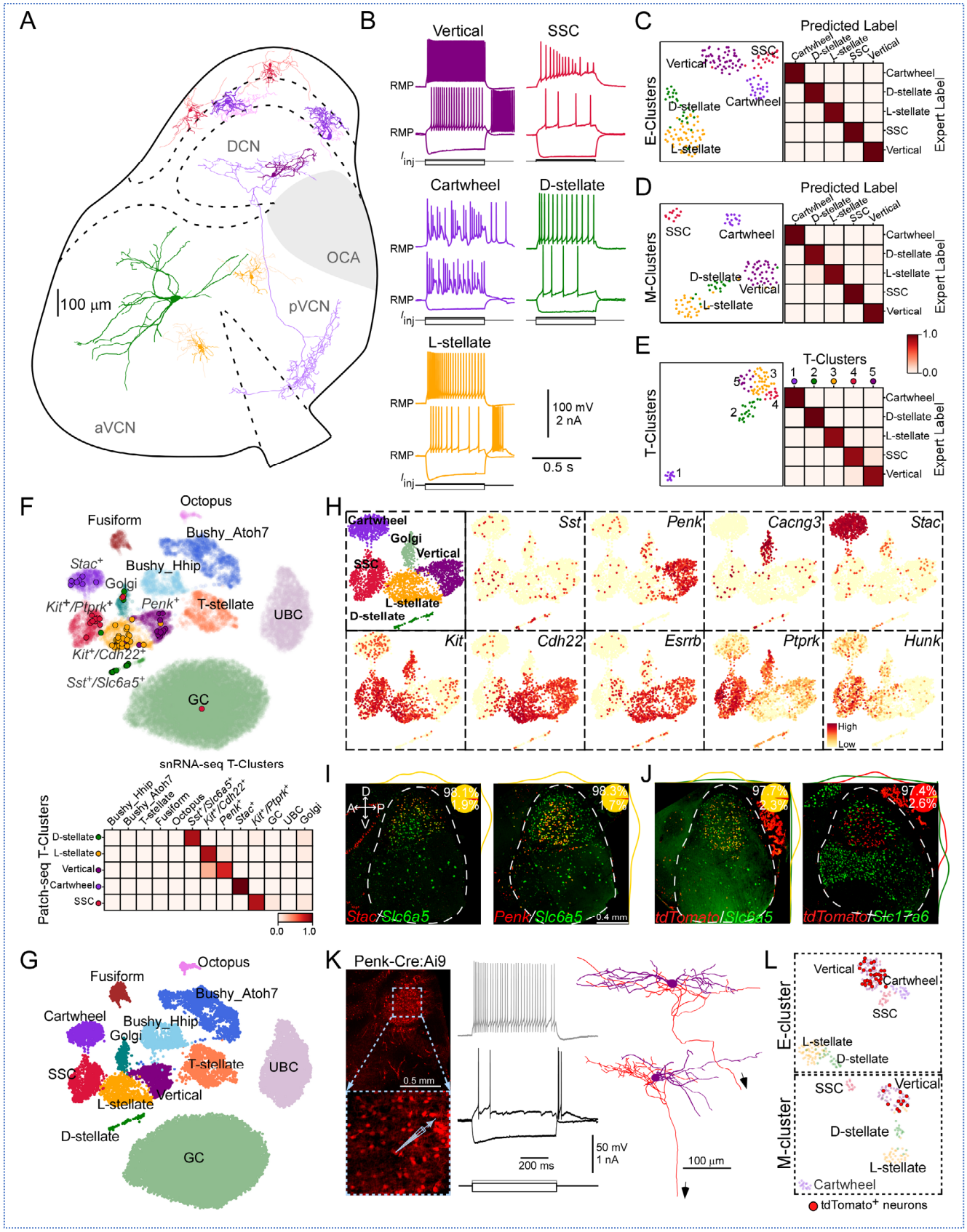

Figure 6. Annotation of molecularly distinct glycinergic cell types in CN. (A) Representative morphology of inhibitory cells in mouse CN (sagittal view), colored by cell type identity. **(B)** Example responses of CN inhibitory cells to current steps. **(C)** Left: UMAP visualization of 163 inhibitory neurons clustered by electrophysiological features and anatomic locations. n=41 for Vertical, n=21 for SSC, n=22 for cartwheel, n=26 for D-stellate, n=53 for L-stellate. Each cell type is colored as in (**C**). For anatomic locations, 0 represents VCN and 1 represents DCN in the cluster analysis. Right: Confusion matrix shows performance (an average of 97.8% accuracy) by the classifier trained with electrophysiological features and anatomic locations. Colored by the expert classification. See Data S2 for the analysis with electrophysiological features only. **(D)** Left: UMAP visualization of 95 CN inhibitory neurons clustered by select morphological features (M-cluster). n=17 for Vertical, n=13 for SSC, n=15 for Cartwheel, n=17 for D-stellate, n=33 for L-stellate. Right: Confusion matrix shows classification performance (average of 95.5% accuracy) by a classifier trained with morphological features. **(E)** Left: UMAP projection of 94 Patch-seq inhibitory neurons clustered by over-dispersed genes, colored by transcriptomic clusters (T-clusters). Right: The matrix shows proportion of Patch-seq cells in each T-cluster assigned to a specific cell type. All cells in T-cluster 1 are cartwheel cells (n=12/12); almost all cells in T-cluster 2 are D-stellate cells (n=20/21); all cells in T-cluster 3 are L-stellate cells (n=35/35); almost all cells in T-cluster 4 are SSCs (n=10/12), and almost all cells in T-cluster 5 are vertical cells (n=12/14). **(F)** Left: Patch-seq cells (n=95) mapped to snRNA-seq UMAP space as shown in Figure 1B. Right: Matrix shows proportion of Patch-seq cells assigned to each T-cluster in (**E**) mapped to one of 13 distinct clusters in UMAP space. **(G)** Annotation of each molecular cluster with ME-types. **(H)** UMAP visualization of all glycinergic neurons and normalized expression of marker genes for each cell type. Each cluster is annotated by Patch-seq. **(I)** FISH co-staining for *Slc6a5* and *Stac* (left), or for *Slc6a5* and *Penk* (right) in sagittal sections. Inset pie charts show proportion of double-labeled cells in single-labeled cells. Yellow lines along images show density of double-labeled neurons along two axes of CN. **(J)** FISH co-staining for *Slc6a5* and *tdTomato* (left), or for *Slc17a6* and *tdTomato* (right) in CN sagittal sections in Penk-Cre:Ai9 mice. Inset pie charts show proportion of double-labeled cells in all *tdTomato*$^+$ cells. (**K**) Left: micrographs show labeled cells in Penk-Cre:Ai9 mice targeted for recording. Middle: example responses of a labeled neuron to current steps. Right: two morphologies of labeled neurons. Arrows indicate axonal trajectory toward VCN. (**L**) Top: Distribution of labeled cells (red circle) in electrophysiological UMAP space as shown in Figure 6C. Almost all labeled cells (30/31) clustered with vertical cells. Bottom: Distribution of labeled cells in morphological UMAP space as shown in Figure 6D. All labeled cells clustered with vertical cells.

inhibitory cell types (Figures 1A, 6A) was then determined by targeting glycinergic cell types for Patch-seq (see Methods). These included vertical, cartwheel, and superficial stellate cells (SSC) in DCN, and L- and D-stellate cells in VCN (Figures 1A, 6A), each of which resides in distinct anatomical locations (except for L- and D-stellate cells) and exhibited unique morphoelectric features (Figure 6A-B). As with excitatory neurons, we validated the expert classification and cell-type assignment of each Patch-seq cell (Figures 6B-D; Data S2). In general, the random forest classifier and clustering-based k-means classifier based on either electrophysiology or morphology distinguished each cell type pair with high accuracy, especially with additional location supervision (Figures 6C-D, Data S2), supporting cell-type assignment of each Patch-seq cell. UMAP projection of these Patch-seq cells resulted in 5 clusters which were then mapped onto the snRNA-seq dataset, successfully identifying transcriptomic clusters for established inhibitory cell types (Figure 6E-G).

With FISH, we validated the molecular correspondences to inhibitory neurons as we did with excitatory neurons. We validated the *Stac*$^+$ cluster as cartwheel cells by FISH staining for *Stac* or *Kctd12,* two major putative marker genes for cartwheel cells (Figures 6H, 6I, S2, Table S1, and Data

S3). FISH staining for *Penk* in wild-type mice and Cre-positive cells in an existing Penk-Cre mouse line validated the *Penk*$^+$ cluster as vertical cells (Figures 6H, 6I, S6E), consistent with these inhibitory neurons being pure glycinergic (Saint Marie et al., 1991; Wickesberg and Oertel, 1990). FISH staining also validated Penk-Cre mice as a specific Cre driver for vertical cells, and thus electrophysiology and morphology of Cre-positive cells in DCN all matched with vertical cells (Figure 6K-L). Interestingly, in addition to labeling vertical cells, *Penk* expression was also enriched in glycinergic neurons in the 'small-cell cap' (Figures 6I-K, Data S3), a narrow CN region between the granule-cell and magnocellular domains of the VCN (Cant, 1993). This topographically unique inhibitory subgroup was devoid of *Gad1* (i.e., purely glycinergic, Figure S6F), and thus genetically more similar to vertical cells than to other small glycinergic neurons in VCN (i.e., *Gad1*$^+$ L-stellate cells, Figures 1C, S6F, also see below). The *Penk*$^+$ cluster thus includes both vertical cells and glycinergic cells in the small-cell cap.

FISH staining further validated the *Sst*$^+$/*Slc6a5*$^+$ cluster as D-stellate cells that could be discriminated with a combination of two genes or even single genes (Ngodup et al., 2020) (Figures S6A1-A2, S2E, and Table S1). To validate *Kit*$^+$/*Cdh22*$^+$cluster as L-stellate cells, we performed co-labeling for *Kit* and *Cdh22*, and for *Kit and Esrrb*, two combinations predicted to distinguish L-stellate cells (Figures 6F-H, S2E). In line with snRNA-seq (Figures 1C, 6H, S2E,), *Kit*$^+$ cells were almost exclusively glycinergic with a smaller soma size compared to *Kit*$^-$ glycinergic neurons (Figure S6D1-D2), and *Kit*$^+$ neurons that were labeled by *Cdh22* or *Essrb* transcripts (*Kit*$^+$/*Cdh22*$^+$ or *Kit*$^+$/*Essrb*$^+$) were mainly detected in the VCN (Figure S6B1-B2), consistent with the location of L-stellate cells. Interestingly, double-labeled glycinergic neurons were sparsely detected in DCN as well (Figure S6B1-B2), suggesting that the *Kit*$^+$/*Cdh22*$^+$ cluster may also include glycinergic neurons in the main body of DCN that are neither cartwheel cells nor vertical cells (Figure S6C1-C1, S6D1-D2), a hitherto undescribed cell type. Finally, to validate *Kit*$^+$/*Ptprk*$^+$ clusters as SSCs, we performed co-staining for *Kit* and *Ptprk*, and for *Kit* and *Hunk,* two potential combinations to discriminate SSCs (Figures 1C, 6F-H, S2E). In line with our analysis, double-labeled glycinergic neurons (*Kit*$^+$/*Ptprk*$^+$ or *Kit*$^+$/*Hunk*$^+$) were mostly detected in the

molecular layer of the DCN (Figure S6B3-B4). Double-labeled cells were also sparsely detected at the VCN, likely reflecting the expression of *Hunk* or *Ptprk* in a small subset of L-stellate cells (Figures 6H, S6B3-B4).

Molecular underpinnings of functional specialization of CN neurons

Our combined dataset provided molecular definitions for all previously defined cell types in CN through their quantitative transcriptomes (Figure 6G). The cell type-specific genome-wide expression patterns implicitly underpin the functional specializations of CN neurons (Leão, 2019). We first analyzed the expression of genes encoding voltage-sensitive ion channels, many of which are cell-type specific and likely contribute to the highly specialized biophysical features of CN neuron (Figures 7A, S7A-B, Data S4). To substantiate this relationship, we take advantage of the bimodal gene expression and physiological data in the Patch-seq dataset and performed sparse reduced-rank regression to identify gene transcripts that were highly predictive of firing properties of excitatory projection neurons (Kobak et al., 2021; Scala et al., 2021). These neurons exhibited either the phasic (single-spike, bushy cell and octuple cells) or tonic firing property (T-stellate and fusiform cells), each characterized by a set of physiological features (Figures 2B, 7B, S7C, Table S2). Our sparse reduced-rank regression model identified two sets of ion channel transcripts that are highly predictive of these physiological hallmarks, particularly when our analysis was restricted to voltage-sensitive ion channels (Method, Figures 7B, S7C). One set of transcripts, including *Kcna1* (Kv1.1), *Hcn1* (HCN1) and *Kcnq4* (Kv7.4), correlated with physiological features defining single-spike firing property (sparse spiking, large voltage sag, low input resistance, short time constant, and a high rheobase and threshold for spike generation), and inversely correlated with tonic firing property (Figures 7B, S7D). This analysis substantiated Kv1.1 and HCN1 as molecular determinants of single-spike firing, in line with prior evidence (Bal and Oertel, 2000, 2001; Cao et al., 2007; Golding et al., 1999; Manis and Marx, 1991; Rothman and Manis, 2003), but also uncovered another putative subthreshold-operating K^+

conductance required for single-spike firing property in CN neurons, Kv7.4-mediated conductance

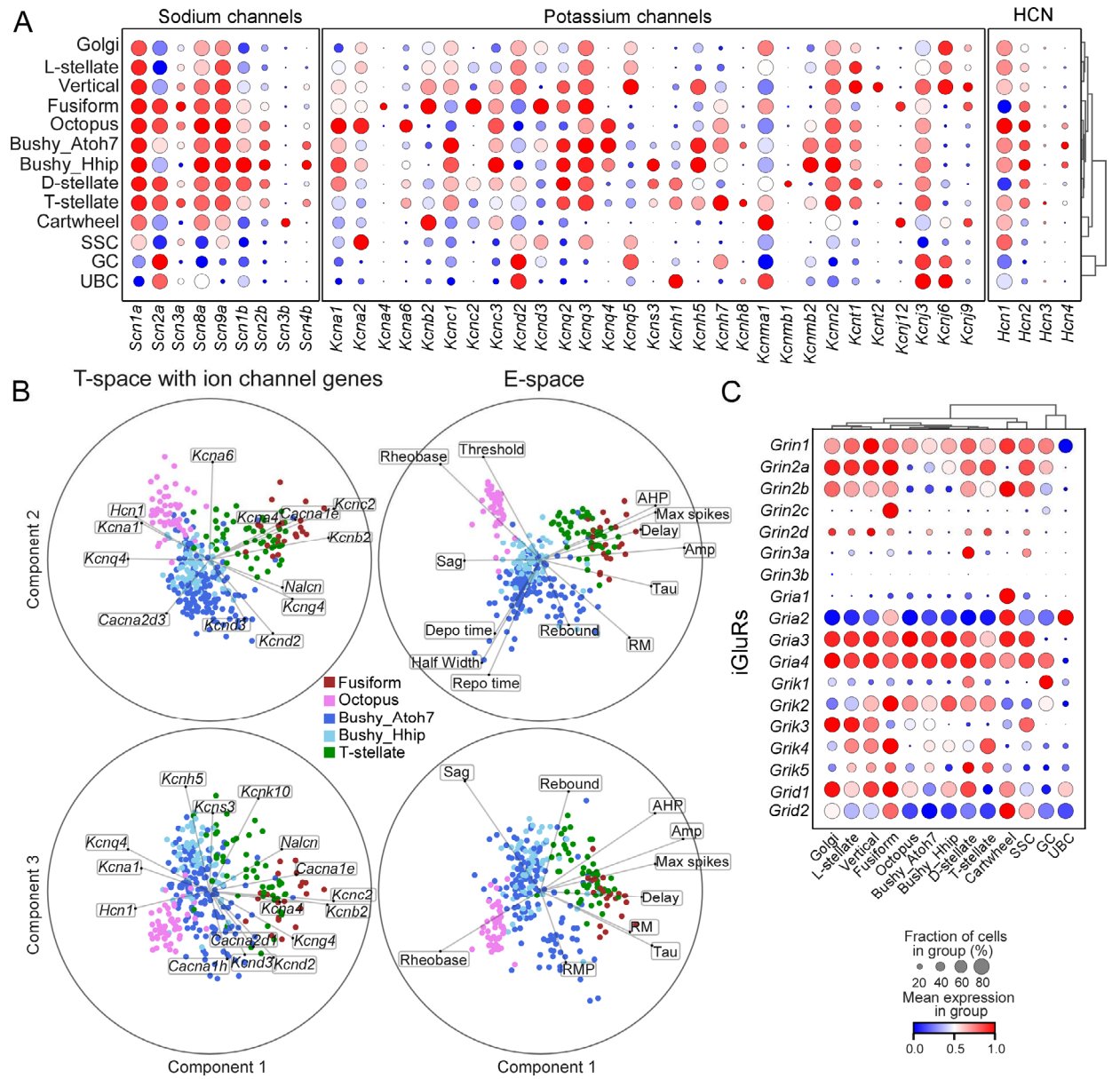

Figure 7. Single-cell transcriptomes provide insights into functional specializations of CN neurons. (A) Dot plots showing scaled expression of the genes encoding ion channels across CN cell type (from snRNA-seq dataset). Those sodium and potassium channel subtypes or subunits with low expression levels (< 20% fraction of the cell in any cell type) were not included in the figure. The size of each circle depicts the percentage of cells in the cluster in which the marker was detected (≥ 1 UMI), and its color depicts the average transcript count in expressing cells. **(B)** Sparse reduced-rank regression (RRR) model to predict electrophysiological features by the expression patterns of 119 ion channel genes (middle, cross-validated $R^2 = 0.32$). The models selected 25 genes. The cross-validated correlations between the first three pairs of projections were 0.81, 0.64, and 0.62 The cross-correlation results were presented as a pair of biplots or bibiplot (left: transcriptome, right: electrophysiology). In each biplot, lines represent correlations between a feature (gene expression or electrophysiology) and two latent components; the circle corresponds to the maximum attainable correlation (r =1). Only features with an average correlation above 0.4 are shown. **(C)** Dot plots showing scaled expression of genes encoding ionotropic glutamate receptors in each CN cell type. See also Figure S7.

(Eatock et al., 2008; Heidenreich et al., 2012; Kalluri et al., 2010; Watanabe et al., 2017). In contrast, a distinct set of transcripts including *Kcnb2* (Kv2.2) and *Kcnc2* (Kv3.2) inversely correlated with the single-spike firing, but correlated with high-frequency tonic firing (T-stellate cells and fusiform cells)

characterized by high-frequency firing, large AHP, short repolarization time, short AP half-width (Figure 7B, S7C, S7D), matching the role of these channels enabling repetitive high-frequency firing (by expediting AP repolarization and speeding the recovery of Na^+ channels from inactivation) (Johnston et al., 2010; Johnston et al., 2008; Lau et al., 2000; Rudy and McBain, 2001; Wang et al., 1998a). Among other relevant transcripts selected, three encoding potassium channels for transient A-type current, *Kcnd2* (Kv4.2), *Kcnd3* (Kv4.3), and *Kcna4* (Kv1.4), correlated with AP delay (Figure 7B, S7C, S7D), matching the transient nature of A-type current that mediates the delay to AP onset (Connor and Stevens, 1971; Kanold and Manis, 1999; Shibata et al., 2000). Thus, Kv1.4 could be the major channel mediating prominent A-currents in fusiform cells that determine their three distinct response patterns ("pauser", "buildup", and "chopper") (Kanold and Manis, 1999; Rhode et al., 1983).

In addition to biophysical specializations, CN neurons rely on specialized structural and synaptic features to fulfill their tasks (Manis et al., 2011; Trussell, 1999). Bushy cells, for example, require large presynaptic terminals (endbulbs of Held) with fast-gating AMPA receptors to enable precise spike timing with AN inputs (Manis et al., 2011). These AMPA receptors form by GluR3 (*Gria3*) and GluR4 (*Gria4*), devoid of GluR2 (*Gria2*), which confers calcium permeability, large conductance and exceptionally rapid gating kinetics (Petralia et al., 2000; Rubio et al., 2017; Wang et al., 1998b). By examining expression patterns of ionotropic receptors across cell type (Figure 7C), we found that such exceptional AMPARs were also expressed in other CN cell types targeted by ANFs (i.e., T-stellate cells, octopus cells, vertical cells), but not in cell types targeted by non-ANF fibers, matching the observation that the very fastest synaptic currents are found only in neurons of the auditory system (Trussell, 1999). Thus, cartwheel cells, targeted by parallel fibers only, mainly expressed GluR1 (*Gria1*) and GluR2 (*Gria2*) (Petralia et al., 1996), an AMPAR composition with slow gating kinetics and calcium impermeability, while AMPARs in UBC, targeted by the mossy fibers, formed almost exclusively by GluR2 (*Gria2*, Figure 7C), an uncommon form of native AMPAR (Zhao et al., 2019). Furthermore, fusiform cells, targeted by both ANF and parallel fibers, have mixed slow (GluR2) and

fast AMPAR (GluR3/4) composition (Figure 7C) (Gardner et al., 1999, 2001). This observation thus supports that postsynaptic AMPAR is specialized according to the source of synaptic input, likely illustrating a general rule governing synaptic specialization across the brain (Gardner et al., 1999, 2001; Petralia et al., 1996). As for other two types of ionotropic glutamate receptors (iGluRs; kainate and NMDA receptors), the expression of these relatively slow kinetic receptors were in general low in time-coding neurons, a necessary feature for fast high-fidelity transmission (Bellingham et al., 1998; Futai et al., 2001). CN neurons are subject to cell type-specific synaptic inhibition and neuromodulation to achieve or refine their functional specialization (Goyer et al., 2016; Trussell, 2019; Xie and Manis, 2013). Our analysis determined cell-type specific expression patterns of a wide variety of receptors for glycine, GABA, and neuromodulators in CN, generally in agreement with previous cellular and systems-level physiological observations (Data S4).

Finally, more than half of known deafness genes showed expression in single types or small sets of cell types, suggestive of their essential roles for central auditory processing (Figure S7E). Our dataset thus could provide a starting point to illustrate central components of hereditary deafness, and to differentiate poorly recognized central causes of deafness from peripheral causes (Figure S7E) (Griffiths, 2002; Kopp-Scheinpflug and Tempel, 2015).

Discussion

One of the biggest challenges in defining a cell-type taxonomy of the brain is to meaningfully reconcile definitions of cell types across the many modalities of measurement typically used to characterize brain cells (Zeng and Sanes, 2017). In the CN, the first relay station in the auditory system, we here succeeded by first defining neuronal populations using transcriptomic profiling, and then relating these populations to anatomical, physiological, and morphological features using Patch-seq combined with histology and FISH. We reveal a direct correspondence between molecularly defined cell populations and all previously defined cell types with known behavioral significance, as

well as discover multiple new subtypes of the major projection neurons in the CN. We thus built a comprehensive and thoroughly validated atlas of cell types in the CN that harmonizes the cell type definitions across all modalities.

Neurons in the CN are highly specialized for processing different aspects of acoustic information and initiating distinct parallel pathways that encode sound location, intensity, pitch, and spectrotemporal modulations (Chi et al., 2005; Grothe et al., 2010). Our analysis indicates that such functional specializations are bestowed by unique transcriptomic programs, and that these programs can be leveraged to define, discriminate, target, and manipulate cell types. Given that parallel sensory maps have been defined in the brainstem for most sensory systems, we expect the emergence of similar basic discoveries that extend our understanding of cellular specializations in other sensory systems and outside of the CN (Young, 1998). Molecular definitions of cell types that initiate parallel pathways in sensory systems in general, and the auditory system in particular, open up new avenues for functional dissections of parallel processing. To date, no molecular tools are available to manipulate cell types in the cochlear nucleus to determine the impact on downstream sound processing and behavior. The novel marker genes identified and validated for each cell type here will ensure the rational design of a molecular toolbox (including the novel Cre lines and in vivo cell type-specific phototagging (Clayton et al., 2021)) to link the activity of brainstem microcircuits to cortex population response patterns, and to perceptual learning or performance. In addition, a cellular and transcriptomic atlas of CN as we generated here provides a comprehensive multi-modal reference and resource to investigate and identify hitherto unknown central components of hearing disorders and to illustrate central consequences of hearing loss at a molecular level (Butler and Lomber, 2013; Griffiths, 2002), as well as facilitate the rational design of auditory brainstem implants (Wong et al., 2019).

Identification of novel cell types in mouse CN

Our combined snRNA-seq/Patch-seq approach molecularly defined all previously described excitatory cell types, with the exception of the rare giant cells, which may share the same molecular identity as fusiform cells (Martin and Rickets, 1981; Schweitzer and Cant, 1985). This approach also revealed molecular subtypes within the classically defined cell classes. By using transcriptomic clustering to parse electrophysiological and morphological datasets into different groups, we were able to identify subtypes of bushy cells and T-stellate cells with distinct properties. Two molecular subtypes of bushy cells have distinct anatomical preference and response kinetics, reminiscent of GBC and SBC, a conventional category of bushy cells with distinct projection targets and functions (Brownell, 1975; Liberman, 1991; Tolbert et al., 1982). We also found that within the groupings of *Atoh*$^+$ and *Hhip*$^+$ bushy cells, distinct variation exists in transcriptomic, topographic, and electrophysiological features, supporting the concept that SBCs and GBCs are broad cell classes that each may contain distinct subtypes. More generally, using transcriptomic clusters to parse cells of similar electrophysiological features proved to be a powerful approach for extracting important biological meaning from the variance in a set of physiological measurements.

T-stellate cells play remarkably diverse roles in auditory function, having axonal projections within the CN and but also extending to multiple downstream nuclei as far as the auditory midbrain (Yin et al., 2019). Such broad projections suggest diverse physiological functions, yet there has been little prior information to support subtypes of the T-stellate cell class. Our finding that T-stellate cells comprise two groups with strikingly distinct gene expression, intrinsic properties, and topography within the CN provides the first, clear evidence for subtypes of T-stellate cells. In vivo recordings refer to T-stellate cells as “choppers”, based on a frequency-independent, regular pattern of spikes observed in spike histograms. Interestingly, several classes of choppers have been distinguished in a wide variety of species including mice, with sustained and transient response patterns being the most common (Roos and May, 2012). It is possible that the two T-stellate subtypes in the present study correspond to these different classes of chopper. Beyond morphological and electrophysiological properties, studies of

these novel subtypes of bushy and T-stellate cells in terms of their synaptic inputs and axonal projections may reveal new principles of auditory coding.

Until recently, the greatest diversity of inhibitory interneurons of CN was thought to be in the DCN (Trussell and Oertel, 2018). The recent discovery of L-stellate cells of VCN indicated that VCN may also harbor multiple interneuron subtypes besides D-stellate cells (Ngodup et al., 2020). Here, we show that L-stellate cells, defined simply as small glycinergic neurons of the VCN, are molecularly diverse. Those glycinergic neurons in the small cell cap resemble vertical cells in DCN (*Penk*$^+$, purely glycinergic), differ from other L-stellate cells (dual transmitters, *Penk*$^-$), and thus may comprise a novel class of inhibitory neurons in the VCN. Within the DCN *Penk* and *Stac* were selective markers for vertical and cartwheel cells, respectively. As these two cell types play distinct roles in gating auditory and multisensory signals in DCN, the identification of markers should facilitate future studies of their role in auditory processing. Another important novel interneuron marker is *Kit*, a gene specifically labeling those small glycinergic neurons across CN (Figures 6, S6) (i.e., excluding vertical cells, cartwheel cells, and D-stellate cells), and its mutations cause deafness suggestive of an important functional role in CN interneurons (Figure S7E) (Ruan et al., 2005; Spritz and Beighton, 1998). Guided by *Kit* expression, we observed small glycinergic neurons in the DCN that are neither vertical cells nor cartwheel cells, suggesting a hitherto unrecognized inhibitory cell type in the DCN. These glycinergic neurons in the DCN appear to be genetically similar to L-stellate cells in the VCN with dual transmitter phenotypes (Figures 1C, 6, S6).

Molecular underpinnings of functional specializations

Our snRNA-seq/Patch-seq dataset provides a resource and reference to systematically explore molecular underpinnings of structural, morphological, synaptic, and intrinsic specializations required for CN neurons to encode the different spectral and temporal features of the sound. As the first step, we used the gene expression dataset combined with regression analysis to identify molecular identities

underlying biophysiological and synaptic properties of CN neurons. We identified three transcripts including *Kcna1*, *Hcn1,* and *Kcnq4* as molecular determinants for single-spike firing property, a property required for time-coding neurons to encode precise AP timing for binaural sound detection (Leão, 2019), in line with the observations that mutations of these genes impair binaural hearing (Bleakley et al., 2021; Ison et al., 2017; Karcz et al., 2015; Tomlinson et al., 2013) (Figure S7E). Kv7.4-mediated currents in time-coding neurons have not been previously described despite the strong *Kcnq4* expression in CN, but their role enabling single-spike property in concert with Kv1 has been confirmed in many other cell types (Eatock et al., 2008; Heidenreich et al., 2012; Kalluri et al., 2010; Watanabe et al., 2017), and *Kcnq4* mutations causes profound hearing loss in human DFNA2 that could not be solely explained by hair cell dysfunctions (Beisel et al., 2005; Kharkovets et al., 2000). Another important ion channel for CN projection neurons is high-threshold Kv3, and these neurons appear to employ distinct subunits of this family to achieve their distinct biophysical needs. While Kv3.2 is critical for tonic firing of T-stellate and fusiform cells, Kv3.3 is specifically enriched in time-coding neurons (Figure 7A) to possibly mediate their fast spike repolarization, a necessary feature for the use of both temporal and rate coding in acoustic processing (Perney and Kaczmarek, 1997; Wang et al., 1998a). This could explain why SCA13 patients (due to *KCNC3* mutations) are unable to resolve interaural timing or intensity (Middlebrooks et al., 2013) (Figure S7E). Interestingly, our analysis did not support the contribution of sodium channel diversity to biophysical properties of CN projection neurons (Yang et al., 2016). The expression of α subunits was similar among projection neurons, characterized by a high expression of *Scn1a, Scn2a* and *Scn6a* but also *Scn9a* (Figure 7A), a subunit thought to be expressed only in the peripheral system (Yu and Catterall, 2003). The contribution of ion channel diversity including sodium channel diversity to the interneuron biophysical properties needs to be further explored.

Acknowledgments

We thank the members of Jiang and Trussell labs for technical assistance, discussions, and comments on the manuscript. Research reported in this publication is supported by research grants R01 MH122169, R01 MH120404, R01 NS110767 (to X.J.), R01 DC004450, R35NS116798 (to L.O.T.), and R01 DC017797 (to M.J.M) from the National Institutes of Health. Research reported in this publication was also supported by the Main Street America Fund, a Shared Instrumentation grant from the NIH (1S10OD016167), and by the Eunice Kennedy Shriver National Institute of Child Health & Human Development of the National Institutes of Health under Award Number P50HD103555 for use of the Microscopy Core facilities and the RNA In Situ Hybridization Core facility at Baylor College of Medicine. We thank Drs. Lisa Goodrich and Arpiar Saunders for the comments on the manuscript and Dr. Dmitry Kobak, Philipp Berens, and Yves Bernaerts for helping with the initial data analysis. The content is solely the responsibility of the authors and does not necessarily represent the official views of the National Institutes of Health.

Author Contributions

J.J., T.N., X.J., Q.M., S.L., C.L. performed the experiments, J.J., M.H., X.J., T.N. analyzed the data. X.J., L.T. M.M. supervised all experiments and data analyses. X.J., L.T. prepared the manuscript with input from all co-authors.

Declaration of interests

The authors declared no competing interests.

Figure legend

Figure 1. Comprehensive transcriptional profiling of cell types across the mouse CN.

(**A)** Depiction of neuronal cell types across mouse CN, colored by cell type identity.

(**B)** UMAP visualization of 31,639 nuclei from CN neurons clustered by over-dispersed genes, colored by cluster identity. Each cluster labeled by key marker genes.

(C) Right: dendrogram indicating hierarchical relationships between clusters. Left: dot plot of scaled expression of selected marker genes for each cluster shown in (**B)**; see Table S1. Circle size depicts percentage of cells in the cluster in which the marker was detected (≥ 1 UMI), and color depicts average transcript count in expressing cells. See Figure S1 and Data S1 for more technical details and annotations.

Figure 2. Using Patch-seq to identify transcriptomic correspondences for excitatory neurons.

(**A)** Representative morphology of excitatory neurons in mouse CN (sagittal view), colored by cell type identity.

(**B**) Example responses of CN excitatory cell types to current steps. Bottom traces show the injected currents. Scalebar: 100 mV for potential, 2 nA for injected currents for all cells except octopus cells (10 nA).

(**C**) Left: UMAP visualization of 404 CN excitatory neurons clustered by over-dispersed physiological features (E-cluster), colored by expert cell type. n=243 for bushy, n=67 for T-stellate, n=58 for octopus, n=36 for fusiform. Right: Confusion matrix shows performance (an average of 99.2% accuracy) by the cell-type classifier trained with physiological features.

(**D**) Left: UMAP visualization of 157 CN excitatory neurons clustered by over-dispersed morphological features (M-cluster), colored by expert cell type. n=105 for bushy, n=16 for T-stellate, n=10 for octopus, n=26 for fusiform. Right: Confusion matrix shows the performance (an average of 95.5% accuracy) by the classifier trained with morphological features.

(**E**) Left: UMAP visualization of 293 Patch-seq excitatory neurons clustered by over-dispersed genes, colored by transcriptomic cluster (T-cluster). Right: the matrix shows proportion of Patch-seq cells assigned to a specific cell type (the expert classification) in each T-cluster. All cells in T-cluster 1 (n= 67/67) and almost all cells in T-cluster 2 (n=111/113) are bushy cells; all cells in T-cluster 3 are fusiform cells (n=22/22); all cells in T-cluster 4 are octopus cells (n=43/43); almost all cells in T-cluster 5 are T-stellate cells (n=46/48).

(**F**) Left: Patch-seq cells (n=187) mapped to snRNA-seq UMAP space as shown in Figure 1B. Right: matrix shows proportion of Patch-seq cells assigned to each T-cluster in (**E**) mapped to one of 13 clusters in UMAP space.

(**G**) Annotation of each molecular cell type with established morpho/electrophysiological types in CN. See Data S2 for more details.

Figure 3. **Novel marker genes for CN excitatory neurons**

(**A)** UMAP visualization of the *Phgdh*$^+$ cluster (n=88) and all Patch-seq octopus cells positioned on UMAP space (left). Middle and Right: UMAP visualization of normalized expression of two discriminatory markers for octopus cell cluster.

(B) FISH co-staining for *Slc17a6* and *Phgdh* (left), or *Slc17a6* and *Dkk3* (right) in sagittal CN sections. D, dorsal; V, ventral; A, anterior; M, posterior. Inset pie charts show proportion of double-labeled cells

in single-labeled cells (*Phgdh*$^+$ or *Dkk3*$^+$). Yellow lines along images show density of double-labeled neurons along two axes of CN.

(C) Top-left: diagram showing patch recording and labeling with biocytin for octopus cells. Top-middle: example responses of an octopus cell to current steps. Top-right: proportion of octopus cells immunopositive for Phgdh. Bottom: example octopus cell filled with biocytin (green) positive for Phgdh (red).

(D) UMAP visualization of *Necab2*$^+$ cluster (n=274) and all Patch-seq fusiform cells positioned on UMAP space (left). Middle and Right: UMAP visualization of normalized expression of two discriminatory markers for fusiform cells.

(E) FISH co-staining for *Slc17a6* and *Necab2* (left), or *Slc17a6* and *Ppfibp1* (right) in CN sagittal sections. Inset pie charts show proportion of double-labeled cells in single-labeled cells (*Necab2*$^+$ or *Ppfibp1*$^+$).

(F) Top-left: diagram showing patch recording and labeling for fusiform cells. Top-middle: example responses of a fusiform cell to current steps. Top-right: proportion of fusiform cells immunopositive for Necab2. Bottom: example fusiform neuron filled with biocytin (green) shows positive for Necab2 (red).

Figure 4. Two molecular subtypes of bushy cells.

(**A)** UMAP visualization of *Hhip*$^+$ and *Atoh7*$^+$ clusters and distribution of Patch-seq bushy cells in UMAP space, colored by cluster.

(**B**) UMAP visualization of two bushy cell clusters and normalized expression of their marker genes, *Hhip*, *Atoh7,* and *Sst*. Top: snRNA-seq, Bottom: Patch-seq.

(**C)** FISH co-staining for *Atoh7* and *Hhip* (left), *Atoh7* and *Sst* (middle), or *Hhip* and *Sst* (right) in CN sagittal sections. Insets show total number of single-labeled cells and double-labeled cells. The lines along images show density of single-labeled or double-labeled cells along two axes of CN. Scalebar applies to all images.

(D) Left: A representative morphology of *Hhip*$^+$ or *Atoh7*$^+$ bushy cell. Axon in red is truncated. Right: Sholl analysis of *Hhip*$^+$ or *Atoh7*$^+$ bushy cell dendrites. $^{**}p < 0.01$, with two-way mixed model ANOVA.

(**E)** Top: example responses of *Atoh7*$^+$ bushy cell (left) or *Hhip*$^+$ bushy cell (right) to hyperpolarized current step and near-threshold depolarizing current step. Bottom-left: individual APs from the *Hhip*$^+$ and *Atoh7*$^+$ cells shown above, aligned with onset of depolarizing current. Bottom-right: two most-discriminating features for *Hhip*$^+$ cells and *Atoh7*$^+$ cells, spike delay and spike duration (half-width). Plotting spike delay against half-width separates the majority of *Hhip*$^+$ cells from *Atoh7*$^+$ cells. $^{**}p < 0.01$; $^{***}p < 0.001$; t-test.

(**F**) Heat map showing normalized expression of the top 20 DEGs for two subtypes. Scalebar: Log2 (Expression level). The cell number in each subcluster is indicated below the figure. (**G**) Volcano plot showing the log2 fold change (log2FC) and -log10(p-value) of detected genes comparing two subtypes. Among DEGs are 14 genes encoding voltage-gated ion channels. See Figure S4 for more analysis.

Figure 5. **Two subtypes of T-stellate cells**.

(**A**) Left: UMAP visualization of two subclusters of *Fam129a*$^+$ neurons (marked by high expression of *Dchs2* or *Fn1*:T-Fn1 and T-Dchs2), colored by subcluster. Right: All Patch-seq cells mapped to *Fam129a*$^+$ cluster on left.

(B) UMAP visualization of normalized expression of discriminatory markers for all T-stellate cells and its two subclusters (*Fam129a*, *Fn1*, *Dchs2*).

(**C**) FISH co-staining for *Fam129a* and *Fn1* in CN sagittal section. Inset pie chart: proportion of double-labeled cells in single-labeled *Fam129a*$^+$ cells. The lines along images show density of single-labeled or double-labeled neurons along the two axes of CN. Two images on right are zoom-in views of boxed regions on left. Arrows indicate double-labeled cells.
(**D**) FISH co-staining for *Fam129a* and *Dchs2* in a CN sagittal section. Two images on right are zoom-in views.
(**E**) Top: 2D spatial projection of Patch-seq T-Fn1 cells and T-Dchs2 cells to a sagittal view of CN, colored by the subtypes. Bottom: Comparing the distance to CN posterior edge between T-Fn1 and T-Dchs2. ***$p < 0.001$, t-test.
(**F**) Example responses of two subtypes (T-Fn1, T-Dchs2) to current steps.
(**G**) Electrophysiological features between two T-stellate subtypes. **$p < 0.01$, ***$p < 0.001$ with the t-test.
(**H**) Left: Representative morphology of two *Fn1*$^+$ cells and two *Dchs2*$^+$ cells in CN sagittal view (soma locations). Axons in red. Right: zoom-in of four T-stellate cells shown on left.
(**I**) Sholl analysis of T-Fn1 and T-Dchs2 dendrites. **$p < 0.01$, ***$p < 0.001$, two-way mixed model ANOVA.
(**J**) The polar distribution histograms of the termination points of dendritic branches with respect to soma of T-Fn1 and T-Dchs2. The terminal distribution of T-Fn1 has two peaks at 145° and 345°, while the terminal distribution of T-Dchs2 has two peaks at 75° and 195°. $p < 0.001$ for difference between the distributions with Kolmogorov-Smirnov statistic.

Figure 6. Annotation of molecularly distinct glycinergic cell types in CN.

(A) Representative morphology of inhibitory cells in mouse CN (sagittal view), colored by cell type identity.

(B) Example responses of CN inhibitory cells to current steps.

(C) Left: UMAP visualization of 163 inhibitory neurons clustered by electrophysiological features and anatomic locations. n=41 for Vertical, n=21 for SSC, n=22 for cartwheel, n=26 for D-stellate, n=53 for L-stellate. Each cell type is colored as in (**C**). For anatomic locations, 0 represents VCN and 1 represents DCN in the cluster analysis. Right: Confusion matrix shows performance (an average of 97.8% accuracy) by the classifier trained with electrophysiological features and anatomic locations. Colored by the expert classification. See Data S2 for the analysis with electrophysiological features only.

(D) Left: UMAP visualization of 95 CN inhibitory neurons clustered by select morphological features (M-cluster). n=17 for Vertical, n=13 for SSC, n=15 for Cartwheel, n=17 for D-stellate, n=33 for L-stellate. Right: Confusion matrix shows classification performance (average of 95.5% accuracy) by a classifier trained with morphological features.

(E) Left: UMAP projection of 94 Patch-seq inhibitory neurons clustered by over-dispersed genes, colored by transcriptomic clusters (T-clusters). Right: The matrix shows proportion of Patch-seq cells in each T-cluster assigned to a specific cell type. All cells in T-cluster 1 are cartwheel cells (n=12/12); almost all cells in T-cluster 2 are D-stellate cells (n=20/21); all cells in T-cluster 3 are L-stellate cells (n=35/35); almost all cells in T-cluster 4 are SSCs (n=10/12), and almost all cells in T-cluster 5 are vertical cells (n=12/14).

(F) Left: Patch-seq cells (n=95) mapped to snRNA-seq UMAP space as shown in Figure 1B. Right: Matrix shows proportion of Patch-seq cells assigned to each T-cluster in (**E**) mapped to one of 13 distinct clusters in UMAP space.

(G) Annotation of each molecular cluster with ME-types.

(H) UMAP visualization of all glycinergic neurons and normalized expression of marker genes for each cell type. Each cluster is annotated by Patch-seq.

(I) FISH co-staining for *Slc6a5* and *Stac* (left), or for *Slc6a5* and *Penk* (right) in sagittal sections. Inset pie charts show proportion of double-labeled cells in single-labeled cells. Yellow lines along images show density of double-labeled neurons along two axes of CN.

(J) FISH co-staining for *Slc6a5* and *tdTomato* (left), or for *Slc17a6* and *tdTomato* (right) in CN sagittal sections in Penk-Cre:Ai9 mice. Inset pie charts show proportion of double-labeled cells in all *tdTomato*$^+$ cells.

(**K**) Left: micrographs show labeled cells in Penk-Cre:Ai9 mice targeted for recording. Middle: example responses of a labeled neuron to current steps. Right: two morphologies of labeled neurons. Arrows indicate axonal trajectory toward VCN.

(**L**) Top: Distribution of labeled cells (red circle) in electrophysiological UMAP space as shown in Figure 6C. Almost all labeled cells (30/31) clustered with vertical cells. Bottom: Distribution of labeled cells in morphological UMAP space as shown in Figure 6D. All labeled cells clustered with vertical cells.

Figure 7. Single-cell transcriptomes provide insights into functional specializations of CN cell types

(**A**) Dot plots showing scaled expression of the genes encoding ion channels across CN cell type (from snRNA-seq dataset). Those sodium and potassium channel subtypes or subunits with low expression levels (< 20% fraction of the cell in any cell type) were not included in the figure. The size of each circle depicts the percentage of cells in the cluster in which the marker was detected ($\geqslant$ 1 UMI), and its color depicts the average transcript count in expressing cells.

(**B**) Sparse reduced-rank regression (RRR) model to predict electrophysiological features by the expression patterns of 119 ion channel genes (middle, cross-validated $R^2 = 0.32$). The models selected 25 genes. The cross-validated correlations between the first three pairs of projections were 0.81, 0.64, and 0.62. The cross-correlation results were presented as a pair of biplots or bibiplot (left: transcriptome, right: electrophysiology). In each biplot, lines represent correlations between a feature (gene expression or electrophysiology) and two latent components; the circle corresponds to the maximum attainable correlation (r =1). Only features with an average correlation above 0.4 are shown.

(**C**) Dot plots showing scaled expression of genes encoding ionotropic glutamate receptors in each CN cell type. See also Figure S7.

STAR METHODS

KEY RESOURCES TABLE

REAGENT or RESOURCE	SOURCE	IDENTIFIER
Experimental Models: Organisms/Strains		
Wildtype (C57BL/6)	Baylor College of Medicine	
GlyT2-EGFP	(Zeilhofer et al., 2005)	RRID:MGI:3835459
Sst-IRES-Cre	Jackson Laboratory	RRID:IMSR_JAX:013044
Penk-IRES2-Cre	Jackson Laboratory	RRID:IMSR_JAX:025112
Gabra6-Cre	MMRRC	RRID:MMRRC_015966-UCD
Ai9 reporter	Jackson Laboratory	RRID:IMSR_JAX:007909
Antibodies		
Anti-Necab2 antibody	Sigma-Aldrich	HPA013998
Anti-Phgdh antibody	Invitrogen	PA5-54360
Goat anti-mouse Alexa-Fluor 633	Invitrogen	A-21052
Goat anti-Rabbit secondary antibody Alexa Fluor™ 647	Invitrogen	A-21244
Chemical and Reagents		
Nextera XT DNA Library Preparation Kit	Illumina	FC-131-1096
Nextera XT index kit v2 Set A/D	Illumina	FC-131-2001/ FC-131-2004
Vectastain ABC HRP Kit	Vector Laboratories	PK-4000
Chromium Next GEM Single cell 3’ Gel Bead V3.1	10x Genomics	PN-1000122
Chromium Next GEM Single cell 3’ GEM Kit V3.1	10x Genomics	PN-1000123
Chromium Next GEM Single cell 3’ Library Kit V3.1	10x Genomics	PN-1000157
Kapa HiFi HotStart ReadyMix	Roche	07958935001
Recombinant RNase Inhibitor	Takara	2313B
Biocytin	Sigma-Aldrich	B4261
N-Methyl-D-glucamine	Sigma-Aldrich	M2004

Superscript II Reverse Transcriptase	Invitrogen	18064071
High Sensitivity DNA Kit	Agilent Technologies	5067-4626
Streptavidin Alexa Fluor™ 568 conjugate	Invitrogen	S11226
Protease Inhibitor Cocktail	Promega	G6521
iodixanol	Sigma-Aldrich	D1556
Software and algorithms		
Patchmaster 2.9.1	HEKA	https://www.heka.com/downloads/downloads_main.html#down_patchmaster
Nest-o-patch	glorfin	https://sourceforge.net/projects/nestopatch/
IDL 8.8	L3Harris Geospatial	https://www.l3harrisgeospatial.com/Software-Technology/IDL
Python 3.7	https://www.python.org	https://www.python.org/downloads/
Scanpy 1.8.1	(Wolf et al., 2018)	https://scanpy.readthedocs.io/en/stable/installation.html
Scvi-tools v0.18.0	(Gayoso et al., 2022)	https://github.com/scverse/scvi-tools
Scrublet	(Wolock et al., 2019)	https://github.com/swolock/scrublet
Scikit-learn 1.0.2	https://scikit-learn.org/	https://scikit-learn.org/stable/install.html
Ploty 5.6.0	https://plotly.com/	https://plotly.com/python/getting-started/
Seaborn 0.11.2	https://seaborn.pydata.org/	https://seaborn.pydata.org/installing.html
Matplotlib 3.4.3	https://matplotlib.org	https://github.com/matplotlib/matplotlib
Cellranger 5.0.1	10x Genomics	https://support.10xgenomics.com/single-cell-gene-expression/software/pipelines/latest/installation

Star 2.7. 7a	(Dobin et al., 2013)	https://github.com/alexdobin/STAR
Featurecounts	(Liao et al., 2014)	http://subread.sourceforge.net/
NLMorphologyConverter 0.9.0	Neuron land	http://neuronland.org/
MorphoPy 0.7.1	(Laturnus et al., 2020)	https://github.com/berenslab/MorphoPy
Neurolucida Ver. 11	MBF Bioscience	https://www.mbfbioscience.com/
Others		
Temperature Controller	Luigs & Neumann	200-100 500 0145
Manipulator	Luigs & Neumann	LN Junior Multipatch
Bioanalyzer	Agilent Technologies	G2939BA
Qubit 4.0 Fluorometer	Thermofisher	Q33238
Amplifier	HEKA	EPC 10 USB Quadro
Micropipette Puller	Sutter	P-1000
Confocal	ZEISS	LSM 710
Mastercycler	Eppendorf	Pro S
Neurolucida Explorer	MBF	Ver. 11

RESOURCE AVAILABILITY

Lead Contact

Requests for further information should be directed to the Lead Contact, Xiaolong Jiang (xiaolonj@bcm.edu).

Data and Code Availability

Original electrophysiological, morphological, and RNA-sequencing data supporting the findings of this study have been deposited to the Mendeley Data (doi:10.17632/2n8m8k6b2g.1). The raw snRNA-seq and patch-seq data are available from the NCBI database with BioProject accession number PRJNA1013912. The original code has been deposited at GitHub (https://github.com/bcmjianglab/cn_project).

EXPERIMENTAL MODEL AND SUBJECT DETAILS

Animals

All experiments were performed according to the guidelines of the Institutional Animal Care and Use Committee (IACUC) of Baylor College of Medicine and Oregon Health and Science University. Wild-type mice or transgenic mice of both sexes on the C57/BL6/J background at the age of postnatal (P) 22-28 were used for single-nucleus RNA sequencing and slice electrophysiology (including Patch-seq). To help distribute our sampling across cell types and to increase the chance of recording certain specific cell types, GlyT2-EGFP mouse line were used to target glycinergic/inhibitory neuronal populations (labeled neurons), while unlabeled cells were targeted for excitatory neuron recording (Ngodup et al., 2020). SST-Cre:Ai9 mouse line was crossed with GlyT2-EGFP mice to identify D-stellate cells and L-stellate cells in the CN for patch clamp recordings (Ngodup et al., 2020). Some recordings from excitatory neurons were performed using wild-type mice as well. In this study, we used 222 mice in total (121 males and 101 females), including 132 wild-type mice, 61 GlyT2-EGFP mice, 17 Penk-Cre:Ai9 mice, and 3 Gabra6-Cre:Ai9 mice. Penk-Cre mice are a gift from Yong Xu Lab at Baylor College of Medicine, while Gabra6-Cre mice are a gift from Susumu Tomita Lab at Yale University. All animals were maintained in the animal facility with a light cycle from 6 am to 6 pm daily, with temperatures ranging from 68 to 72 °F and humidity ranging from 30% to 70%.

METHOD DETAILS

Single nucleus extraction and single-nucleus RNA sequencing (snRNA-seq)

Mice were deeply anesthetized with 3% isoflurane and decapitated immediately, and their brains were immediately removed from the skull and then transferred into an iced oxygenated NMDG solution (93 mM NMDG, 93 mM HCl, 2.5 mM KCl, 1.2 mM NaH_2PO_4, 30 mM $NaHCO_3$, 20 mM HEPES, 25 mM Glucose, 5 mM Sodium Ascorbate, 2 mM Thiourea, 3 mM Sodium Pyruvate, 10mM $MgSO_4$ and 0.5 mM $CaCl_2$, pH 7.4) for further dissection. Cochlear nuclei (CNs) were dissected from each brain under a stereoscopic microscope and then transferred into a 1.5 mL Eppendorf tube, and tubes were immediately immersed in liquid nitrogen. Brain tissues were then transferred into a -80 ºC freezer for

long-term storage. Each tissue sample was pooled from 8 to 10 mice for single-nucleus extraction and single-nucleus RNA sequencing (snRNA-seq).

Single nucleus extraction from brain tissues followed a published protocol (Krishnaswami et al., 2016). Briefly, frozen tissues were homogenized with 2 mL homogenization buffer (HB, 250 mM Sucrose, 25 mM KCl, 5 mM $MgCl_2$, 10 mM Tris, 1mM DTT, 1x Protease Inhibitor, 0.4 units/µL Rnase Inhibitor, 0.1% Triton X-100) in Wheaton Dounce Tissue Grinder. Cell debris and large clump were removed with a 40 µm cell strainer (Flowmi). The homogenate was centrifuged at 1,000 g for 5 min at 4 ºC. The palette was resuspended with 25% iodixanol in the centrifugation buffer (CB: 250 mM sucrose, 25 mM KCl, 5 mM $MgCl_2$, 10 mM Tris) and layered on top of 29% iodixanol. The mixture was centrifuged at 13,500 g for 15-30 min at 4 ºC. The supernatant was carefully removed without disrupting the nuclei pellet. The nuclei pellet was resuspended with the resuspension buffer (RB: 1 % UltraPure BSA in Rnase-free PBS).

Nuclei were counted using a hemocytometer or CellCounter (Countess II, Invitrogen) and diluted to ~ 1,000 nuclei/µL for single-nucleus capture on the 10x Genomics Chromium Next GEM Single Cell 3'v3 system following the standard user guide. Droplet-based snRNA-seq libraries were prepared using the 10x Genomics Chromium Single Cell kit according to the manufacturer's protocol and were sequenced on the Illumina NovaSeq 6000 or Hiseq 4000 platform with a pair-end 150 bp strategy (average depth 40k–50k reads/nucleus). Cell Ranger (version 5.0.1) with the *Mus musculus* genome (GRCm38) and annotation GTF (version M23) was used to generate the output count matrix.

Slice preparation and electrophysiology

Brain slices were prepared from the mouse CN as previously described with a slight modification (Jiang et al., 2015; Ngodup et al., 2015; Yang and Xu-Friedman, 2008). Briefly, mice at P22-28 were deeply anesthetized with 3% isoflurane and then immediately decapitated. The brain was removed and placed in the iced oxygenated NMDG solution (for the recipe, see above). The brain tissue containing

CN was sliced into 200-300 µm thick sections parasagittally in the NMDG solution with a microtome (Leica, VT1200). The slices were transferred into the oxygenated NMDG solution (34 ± 0.5 ºC) for 10 min and then incubated in the artificial cerebrospinal fluid (ACSF, 119 mM NaCl, 2.5 mM KCl, 1 mM NaH_2PO_4, 25 mM $NaHCO_3$, 1 mM $MgCl_2$, 25 mM glucose and 2 mM $CaCl_2$, pH 7.4) at 34 ± 0.5 ºC for 40-60 mins before recording.

Whole-cell recordings were obtained from CN neurons as previously described (Jiang et al., 2015). Borosilicate glass pipettes (3–5 MΩ) were pulled with micropipette pullers (P-1000, Sutter) and filled with intracellular solution containing 120 mM potassium gluconate, 10 mM HEPES, 4 mM KCl, 4 mM MgATP, 0.3 mM Na_3GTP, 10 mM sodium phosphocreatine, and 0.5% biocytin (pH 7.25). Whole-cell recordings were performed at 32 ± 0.5 ºC with the EPC 10 amplifiers (HEKA Electronics, Lambrecht, Germany). PatchMaster (HEKA) was used to operate the recording system and record the electrophysiology data. The membrane potential response of each neuron to increasing current steps (600 ms) every 1s was digitized at 25 kHz. To compare the intrinsic properties and firing pattern across cell type, their membrane responses to a hyperpolarizing current step, to the current step at the rheobase, and to a current step at 2X rheobase were recorded and shown for each cell type (Figure 2-6). Spontaneous synaptic events were recorded at -60 mV for at least 30s. Recorded neurons were then fixed for *post hoc* morphological recovery.

Patch-seq

Patch-seq was performed on CN neurons following our published protocol (Cadwell et al., 2017). Briefly, the RNA was extracted from each neuron upon completion of whole-cell recordings (including recordings of synaptic events) with a modified internal solution (110 mM potassium gluconate, 4 mM KCl, 10 mM HEPES, 0.2 mM EGTA, 4 MgATP, 0.3 Na_2ATP, 5 mM Na_2-phosphocreatine, 0.5% biocytin and 0.48 units/µL RNase inhibitor, pH 7.25). Recorded neurons were then fixed for *post hoc* morphological recovery. The RNA was reverse transcribed with Superscript II Reverse Transcriptase (Invitrogen). The cDNA samples that passed quality control were used to generate sequencing libraries

using the Nextera XT DNA Library Preparation Kit (Illumina), following the user guide. Each library was sequenced at a depth of 1~2 million pair-end 150bp reads on the Illumina NovaSeq 6000 or Hiseq 4000 platform. Raw reads were aligned to the *Mus musculus* genome (GRCm38) with annotation GTF (version M23) using STAR 2.7.7a (Dobin et al., 2013), and an expression matrix was generated with FeatureCounts (Liao et al., 2014).

RNA fluorescence in situ hybridization

RNA fluorescence in situ hybridization (FISH) was performed on 25 µm thick sagittal sections containing the CN at the RNA In Situ Hybridization Core at Baylor College of Medicine, using a previously described in situ hybridization method with slight modifications (Yaylaoglu et al., 2005). Digoxigenin (DIG) and Fluorescein isothiocyanate (FITC) labeled mRNA antisense probes were generated from reverse-transcribed mouse cDNA. Primer sequences for the probes were derived from Allen Brain Atlas (http://www.brain-map.org). DIG-labeled probes were visualized with tyramide-Cy3 Plus and FITC-labeled probes were visualized with tyramide-FITC Plus. Images were captured at 20X magnification using LSM 710 or 880 confocal microscope (Zeiss).

Immunofluorescence staining

GlyT2-EGFP mice at P22-28 were perfused transcardially with 20 mL PBS followed by 20 mL of 4% PFA in 0.1 M PB. The brain was removed, post-fixed in 4% PFA for 1 day, and then sagittally sectioned into 50 µm thick slices in PBS. The slices were washed 3 times in PBS before blocking with 10% goat serum and 1% Triton X in PBS for 1 hour. The slices were incubated first with mouse anti-Phgdh (Invitrogen, 1:400) or rabbit anti-Necab2 (Invitrogen, 1:500) as primary antibodies, and then incubated with Alexa-Fluor goat anti-mouse 633 or goat anti-rabbit Alexa-Fluor 647 (Life Technologies) as secondary antibodies for at least 1 hour. Slices were then mounted with the mounting medium (Abcam, ab104139). To stain Phgdh or Necab2 in recorded neurons, brain slices were immediately fixed after whole-cell recording with 4% PFA for 1 day. The slices were first incubated with primary antibodies (see above) for at least 1 hour, and then incubated with Alexa Fluor 568

conjugates of streptavidin to visualize biocytin together with those secondary antibodies (see above) to visualize putative signals of Phgdh or Necab2 in recorded neurons. Images were captured at 10× or 20× magnification using LSM 710 confocal microscope (Zeiss).

Morphological recovery

Morphological recovery of recorded neurons and light microscopic examination of their morphology were carried out following previously described methods (Jiang et al., 2015). In brief, upon the completion of whole-cell recordings, the slices were immediately fixed in 2.5% glutaraldehyde/4% paraformaldehyde in 0.1M PB at 4 °C for 10-14 days and then processed with an avidin-biotin-peroxidase method with an ABC kit to reveal cell morphology. Recovered neurons were examined and reconstructed using a 100× oil-immersion objective lens and camera lucida system (Neurolucida, MicroBrightField). For morphological feature extraction, only cells with a sufficient morphological recovery were included.

QUANTIFICATION AND STATISTICAL ANALYSIS

Computational analysis of snRNA-seq data

For snRNA-seq data, we used CellRanger (version 5.0.1) to generate a barcode table, gene table, and gene expression matrix. Downstream analysis and visualization were performed using Scvi-tools and SCANPY (Wolf et al., 2018). For preprocessing, we followed the standard protocols used in the field (Luecken and Theis, 2019). Specifically, nuclei with > 5% UMIs mapped to mitochondrial genes and those with less than 200 genes detected were excluded from the analysis. We removed potential doublets sample-by-sample using Scrublet (Wolock et al., 2019). Doublet score and doublet predictions histogram of each sample were manually inspected, adjusted, and then concatenated. A putative single nucleus with a doublet score exceeding the 95th percentile was removed from the downstream analysis. Those putative single nuclei co-expressing multiple canonical marker genes for different cell types as follows were also considered as doublets and were excluded for further analysis: *Mobp/Mog/Mag* (ODC), *Gabra6* (granule cell), *Ptprc/Csf1a/C1qa* (microglia), *Slc1a2/Aqp4/Gja1*

(astrocyte), *Dcn* (fibroblast), *Gad1/Gad2/Slc6a5* (inhibitory neurons), *Flt1/Cldn5* (endothelial). Counts of all the nuclei were normalized by the library size multiplied by 10,000 and then logarithmized. The top 6,000 highly variable genes, which were identified by dispersion-based methods, were used for principal component analysis. Leiden graph-clustering method and UMAP were used for clustering and visualization.

Due to the proximity of the CN to the cerebellum (CB), paramedian lobule (dorsal to the CN), to the principal sensory nucleus of the trigeminal nerve (PSN; ventral to CN), and to the dentate nucleus, our microdissection inevitably includes more or less of these adjoining tissues. To remove potential CB-derived nuclei from our dataset (Method S1), we compared our data to a recently published CB snRNA-seq dataset (Kozareva et al., 2021). By examining the expression of marker genes for each CB cell type (identified by Kozareva et al., 2021) in our snRNA-seq data, we identified several putative neuronal and non-neuronal CB clusters in our dataset. Firstly, two clusters show clear molecular signatures of Bergmann cells and Purkinje cells respectively (Method S1A-B), indicating they are contaminated nuclei from these two CB-specific cell types. Secondly, two large clusters assigned to granule cells (i.e., enriched with the canonical marker gene *Gabra6*) could be discriminated by the expression levels of *Grm4* and *Col27a1* (Method S1C). Based on the molecular signatures of CB granule cells (Kozareva et al., 2021) and Allen Brain Atlas ISH data (Method S1C), we concluded that *Grm4*$^{-}$/*Col27a1*$^{+}$ cluster corresponds to granule cells from CN, while the *Grm4*$^{+}$/*Col27a1*$^{-}$ cluster corresponds to granule cells from CB (CB_Granule). After removing these CB clusters from our dataset, we computationally isolated the neuronal population (except for granule cells and UBC) and then performed subclustering analysis to reveal distinct neuronal clusters (Method S1D). One neuronal cluster enriched with *Htr2c* and two clusters enriched with *Necab2* were first identified (Method S1E-F). As shown on Allen Brain Atlas (Method S1E), *Htr2c* expression is restricted to the dentate nucleus, and thus this *Htr2c*-enriched cluster in our dataset is from the dentate nucleus. Two *Necab2*$^{+}$ clusters

are either *Tnnt1*$^{+}$ or *Tnnt1*$^{-}$, and only the *Tnnt1*$^{+}$ nuclei are from the CN while *Tnnt1*$^{-}$ nuclei are from the PSN, based on Allen ISH data (Method S1E-F) and our FISH data (Figure S3).

We then identified two pure GABAergic clusters (*Gad1*$^{+}$/*Slc6a5*$^{-}$) enriched with *Tfap2b* (Method S1G), reminiscent of MLI1 and MLI2 from the CB (Kozareva et al., 2021). Since pure GABAergic interneurons in the CN are absent or extremely rare (Method S1H), we concluded these two clusters are indeed MLI1 and MLI2 from the CB. We also identified two *Tfap2b*-enriched glycine/GABA combinatorial clusters reminiscent of Golgi cells (Kozareva et al., 2021), which are either *Scrg1*$^{+}$ or *Scrg1*$^{-}$. We concluded that the *Scrg1*$^{+}$ cluster results from contaminated nuclei from Golgi cells in the CB (CB_Golgi) based on the CB snRNA-seq dataset (Kozareva et al., 2021) and our FISH data (Method S1I); only the *Scrg1*$^{-}$ cluster corresponds to CN Golgi cells (CN_Golgi, Method S1I, Figure S2). We also identified a glycine/GABA combinatorial cluster enriched with both *Klhl1 and Slc36a2* (Method S1G), reminiscent of Purkinje layer interneurons (PLIs) from the CB (Kozareva et al., 2021). We conclude that this indeed corresponds to PLIs contaminated from the CB based on the expression patterns of *Klhl1 and Slc36a2* across CN and CB (Method S1J).

Removal of non-neuronal nuclei from adjoining regions was not addressed (except for Bergmann cells) since non-neuronal populations are not the focus of our analysis. Thus, the non-neuronal nuclei as shown in Figure S1B may include those from adjoining regions. The UBC population in our dataset may include CB-derived UBCs, but we believed that this contamination, if any, was minimal. Firstly, using the ratio of the UBC population versus GC population in the CB (~1: 300) (Kozareva et al., 2021), we estimated ~80 UBCs from CB might be included in our dataset (based on 24,118 CB-derived GCs in our dataset). In addition, the region of the CB close to the CN (i.e., CB paramedian lobule) has a smaller population of UBCs compared to other regions of the CB. We thus concluded that out of 3,653 UBCs in our dataset, only a very small number of them may be UBCs from the CB, which would not significantly affect our analysis.

After the removal of the nuclei from adjoining tissues, the remaining 61,211 nuclei were used for further clustering analysis, and each cluster and cell type were annotated with the commonly used marker genes as listed in Table S1 (including the marker genes for CB cell types). Calculation of the local inverse Simpson's index (Korsunsky et al., 2019) demonstrated that these populations were well mixed and contained cells from each sample, indicating successful integration (Data S1). Our initial clustering combined the single-nucleus expression data from male (n = 31,115 nuclei) and female samples (n = 13,140 nuclei); each cluster comprised cells from both sexes, indicating that there were few sex-dependent differences (Data S1). The data from both sexes were thus pooled for subsequent analyses.

Patch-seq data Analysis

In total, we performed Patch-seq from 438 cells (323 excitatory neurons, 115 inhibitory neurons, from 69 mice) that passed initial quality control. Among these sequenced 438 cells, 388 neurons (293 excitatory neurons, 95 inhibitory neurons) passed further quality control, yielding 2.40 ± 0.08 million (mean ± s.e.) reads and 8,025 ± 70 (mean ± s.e.) detected genes per cell (Data S1). Of these neurons, 154 had sufficient biocytin staining for their morphology to be reconstructed (97 excitatory neurons, 57 inhibitory neurons). Patch-seq data were clustered and visualized following a similar method with SCANPY. Cells with a mapping rate of < 60% and gene features of < 4000 were not included in the analysis. We used the batch-balanced KNN method for batch correction (Polański et al., 2019). Patch-seq data were mapped to the snRNA-seq data following a similar protocol as used previously (Scala et al., 2021; Scala et al., 2018). Briefly, using the count matrix of 10x Genomics snRNA-seq data, we selected 3000 "most variable" genes, as described previously (Kobak and Berens, 2019). We then log-transformed all counts with log2(x+1) transformation and averaged the log-transformed counts across all cells in each of the identified clusters in the snRNA-seq dataset to obtain reference transcriptomic profiles of each cluster (N×3000 matrix). Out of these 3,000 genes, 2,575 are present in the mm10 reference genome that we used to align reads in our Patch-seq data. We applied the same log2(x+1)

transformation to the read counts of Patch-seq cells, and for each cell, computed Pearson correlation across the 2,575 genes with all clusters. Each Patch-seq cell was assigned to a cluster to which it had the highest correlation.

DEG analysis and marker gene identification.

To identify the DEGs for clusters and subclusters, we used SCANPY to rank genes using the T-test_overestim_var test with Benjamini–Hochberg correction. SCANPY generated logFC (with the base as 2) and FDR (False discovery rate) corrected P value and DEGs were identified based on p-value < 0.01 and |log2FC| > 1. This method could detect more DEGs in the clusters that have large numbers of cells, while in relatively small cell populations only those with much higher fold changes could be identified as DEGs.

Electrophysiological feature extraction and analysis

Electrophysiological data were analyzed with a python-based GUI named PatchView that we have developed (Ming Hu, 2022) or a custom-made IDL code. To access the IDL code, the raw electrophysiological data was exported to ASCII format using Nest-o-Patch. To highlight the differences in the intrinsic properties and firing patterns, the membrane responses to a hyperpolarizing current step, to the current step at the rheobase, and to a current step at 2X rheobase were shown for each cell type (Figures 2-6). 20 electrophysiological features were extracted from the electrophysiological traces following a similar method as previously described (Method S2) (Scala et al., 2021).

To calculate the time constant (Tau), all the traces in response to negative current steps (from the onset of the current step to the minimal potential during the stimulation period) were fitted with an exponential function as follows:

$$f(t) = ae^{(-t/\tau)} + C$$

Here, *f(t)* is the voltage at the time *t*, τ is the membrane time constant, *a* and *C* are two constants. The

τ was calculated for each trace. Boxplot was used to remove the outliers and the mean averaged across all traces after outlier removal was used as the time constant.

We calculated the sag ratio and rebound voltage using the hyperpolarizing trace elicited by the maximal negative current injection. The sag ratio was defined as the difference between the sag trough of the trace and the resting membrane potential (RMP) (ΔV1), divided by the difference between steady-state membrane voltage and the RMP (ΔV2). The trace from the stimulation offset to the peak of the depolarizing trace following the offset was fitted with an exponential function, and the potential difference between the maximal value of the fitting curve and the RMP was defined as the rebound value.

To calculate the input resistance and RMP, we measured the steady-state membrane potentials (determined by the average values of the last 100 ms of the hyperpolarization) in the traces elicited by the first five negative-going currents in the step protocol, and then plotted these values (y-axis) with each of the corresponding currents (x-axis). We fit the plot with a linear function shown as follows:

$$f(c) = R_m c + V_{rmp}$$

Here, *f(c)* steady-state voltages, c is the injected currents, *Rm* and *Vrmp* are constants that represent the slope of the linear function and the potential at the y-axis intersection, corresponding to the input resistance and the RMP respectively.

Rheobase is defined as the minimum current that could elicit any action potentials (APs) during the step-current injection. To extract the properties of action potential (AP), we used the first AP elicited by our step stimulation protocol. To calculate the threshold of the AP, the trace within 20 ms preceding the AP peak was used to calculate the third derivative and the data point with the maximal third derivative value was defined as the AP threshold (Henze and Buzsaki, 2001). The AP amplitude is the difference between the threshold potential and the peak potential of the AP. The AP half-width was defined as the time difference between the voltage at AP half-height on the rising and falling phase of

the AP. The afterhyperpolarization (AHP) was defined as the potential difference between the AP threshold and the minimal value of the trough after the AP. The time difference from the stimulation onset to the first AP's threshold at the rheobase sweep was defined as the AP delay time. The depolarization time was the time difference from the AP threshold to the overshoot. The time from the overshoot to the repolarizing voltage that equaled the threshold was the AP's repolarization time.

Spike-frequency adaptation was quantified with the membrane potential trace in response to the injection of the step current at 2X Rheobase. The interspike interval (ISI) between the first two APs divided by the ISI between the second and the third APs was the initial adaptation index. The ISI between the first two APs divided by the ISI between the last two APs was the last adaptation index.

Reduced-rank regression

Reduced-rank regression (RRR) was performed as previously reported (Scala et al., 2021). In brief, we used 14 electrophysiological features extracted from 326 Patch-seq excitatory neurons to predict the electrophysiological features from gene expression. The gene counts were log-normalized and the top 1,000 highly variable genes were selected for RRR analysis in the full model. For Figure S7C, we used a model with rank r=5, zero ridge penalty (α=1), and lasso penalty (λ=0.51) tuned to yield a selection of 25 genes. For RRR analysis based on the ion channel genes (the second model, Figure 7B), a list of 330 ion channel genes were obtained from https://www.genenames.org/. Among these genes, 119 genes have expression in at least 10 of the Patch-seq neurons and thus were chosen for RRR analysis. A model with rank r=5, α =1, and λ=0.27 was used to yield 25 genes. Bibiplots were used to show the RRR analysis results (Scala et al., 2021). Only features with an average correlation above 0.4 were shown and each patch-seq cell (each point) was colored by cell types in the bibiplots. The Pearson correlation coefficients between the electrophysiological features and the log-normalized expression of the 25 predicted genes by RRR model were calculated to estimate the correlation between the electrophysiological features and gene expression (Figure S7D).

Morphological reconstruction and analysis

Neuronal morphologies were reconstructed with Neurolucida (MicroBrightField) and analyzed with Neurolucida Explorer (including Sholl analysis of the dendritic arbors and the soma shape analysis). For a more comprehensive morphological feature analysis, each morphology file was converted into the SWC format with NLMorphologyConverter 0.9.0 (http://neuronland.org) for feature extraction using MorphoPy (https://github.com/berenslab/MorphoPy). The features used for M-type clustering analysis were shown in Data S2. See https://github.com/bcmjianglab/cn_project/tree/main/patchseq/M-clusters for a detailed description of the morphological features.

Register the cell's anatomic location

To register each Patch-seq cell to the CN 3-dimensional (3D) location, we first generated a 3D CN reference space based on the Allen Mouse Brain Atlas and then aligned each brain slice used for our Patch-seq recordings to this reference space. We reconstructed a contour on each slice that delineates the entire CN area in that slice, and then iteratively searched for the contour within the 3D CN reference space that best matched the reconstructed contour (i.e., estimating the 3D location and orientation of that slice). Since our slices were cut in the para-sagittal plane, we limited our grid search parameters range: pitch angle (0, -25 radians) and roll angle (0, -20 radians), median to lateral shift (0, 850 μm), in-plane orientation (-90, 90). For each parameter set, we calculated the overlapping area of the reconstructed contour with the corresponding contour in the 3D CN reference space. The parameters that result in a maximal overlapping area were used as the final parameter for estimation. We visually inspected the mapping results to rule out erroneous registration. For some ambiguous slices (i.e., having very small CN regions), we further limited the search parameter range to improve the accuracy. The location of neurons in that slice was then projected into the 3D CN reference space.

Machine learning algorithms

A random forest classifier was used to discriminate cell types based on electrophysiological and

morphological features. Briefly, the electrophysiological or morphological features of each neuron were extracted, normalized, and scaled. The data were split into training and testing datasets randomly, and the classifier was trained with the training data. The accuracy in distinguishing the cell types by the classifier was evaluated with the testing dataset. The accuracy varied with different training datasets used, so we trained the classifier 10,000 times, each with a different training dataset. The classifier settings with the top 100 performance outcomes were used to weigh the electrophysiological or morphological features for cell type discrimination. The overall accuracy in discriminating cell types by the classifier was reported as the mean accuracy within the chosen settings. The top 15 most important features contributing to the performance were used for UMAP visualizations (Data S2). A confusion matrix was used to show the overall accuracy in distinguishing the cell types by the classifier.

FISH image analysis and quantification

Confocal images were captured from FISH-stained brain slices using LSM 710 or 880 confocal microscopes (Zeiss), and the image files (.lsm) containing image stacks were loaded into IDL for analysis of the distribution and co-localization of various mRNA transcripts. From each slice, the images were generated to capture either green fluorescence signals (FITC) or red signals (DIG). The maximum projected image was filtered with a Gaussian filter to remove background signals. To detect a cell with expression signals, cell regions were segmented using a customized IDL code (Method S3). A cell region with an area smaller than 80 μm^2 or larger than 800 μm^2 was not counted as a cell. A cell region with a circularity of less than 0.4 was not counted as a cell either. The circularity of a cell was calculated using the function: $C = 4\pi a^2/p^2$. Here, C is the circularity, a is the area of a cell region and p is the perimeter of the cell region. Cell regions outside the CN area were not included for further analysis. The spatial position of a cell was set as the median of the x or y positions of the pixels within a detected cell region. The fluorescence intensity (F) of a detected cell (either green or red) was set as the mean intensity of all pixels within a detected cell region. After removing fluorescence intensity

values within a cell region, the images of each channel were then smoothed by a 60 μm length smoothing window. The smooth images were counted as the background signals of each channel. The background signals (F_0) of a detected cell were set as the mean values of the background intensities within a cell region. The intensity differences (ΔF) between F and F_0 divided by F_0 of a detected cell from both channels (green and red) were used to generate a 2-D scatter plot in Python, with each axis representing either channel. From this scatter plot, we used a method similar to the Flow Cytometry gated analysis to determine whether a cell was single-labeled or double-labeled (Method S3). The number of single-labeled and double-labeled cells was counted across 5-8 consecutive sagittal sections of CN. The distribution of labeled cells (single or double) across CN were quantified through the A-to-P and D-to-V axis with Jointplot from Seaborn python package. See https://github.com/bcmjianglab/cn_project/tree/main/FISH_analysis for more details about FISH image analysis.

ISH images in Data S3 were acquired from the Allen Mouse Brain Atlas (www.mouse.brain-map.org/)(Lein et al., 2007). Single discriminatory markers were shown for each cell type, with several ISH images being repeated. ISH images were acquired with minor contrast adjustments as needed to maintain image consistency.

Supplemental figures and legends

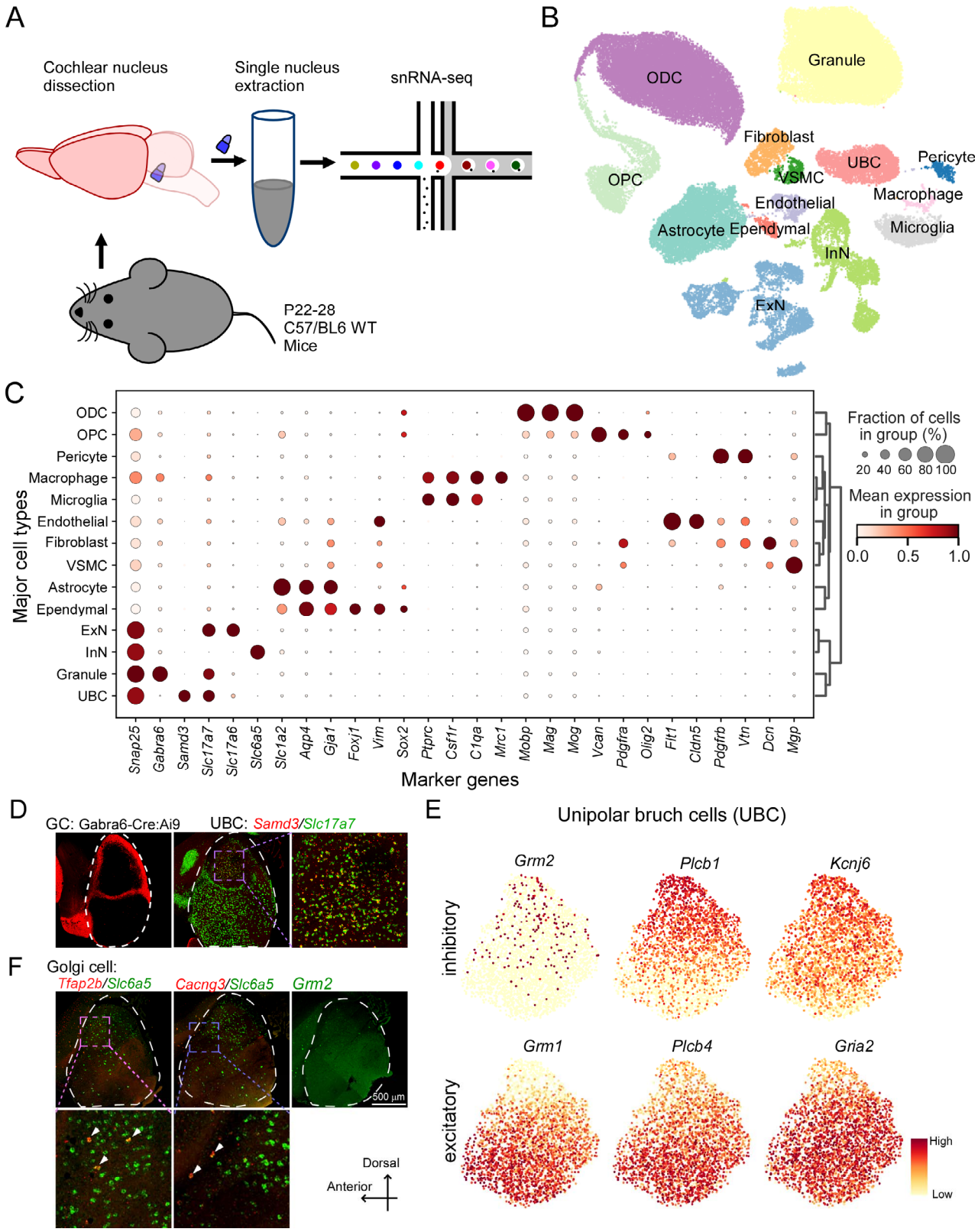

Figure S1. Single-nucleus transcriptomic profiling of mouse CN. Related to Figure 1.

(A) Method flowchart.

(B) UMAP visualization of 61,211 nuclei from the CN (after profile quality control, removing nuclei from adjoining brain tissues, and cell type annotation; Methods), colored by cell type identity. ODC,

oligodendrocyte; OPC, oligodendrocyte precursor cell; ExN: excitatory neurons; InN: inhibitory neurons; VSMC: vascular smooth muscle cells; Endothelial: endothelial cells; Fibroblast: fibroblast-like cells; Ependymal: ependymal cells; Granule: granule cells; UBC: unipolar brush cells.

(C) Dendrogram indicating hierarchical relationships between cell types (right) with a dot plot (left) of scaled expression of marker genes for major cell types as shown in (**B**). Cell type assignments, based on the expression of known marker genes, are indicated on the right (also see Table S1). Circle size depicts the percentage of cells in the cluster in which the marker was detected (≥ 1 UMI), and the color depicts the average transcript count in expressing cells.

(D) Left: A representative confocal micrograph showing labeled cells in the CN of Gabra6-Cre:Ai9 mice. Note: labeled cells are restricted to granule cell layer. Middle: FISH co-staining for *Slc17a7* and *Samd3* in a representative CN sagittal section. Note: *Samd3*$^+$ excitatory neurons (*Samd3*$^+$/*Slc17a7*$^+$, yellow signals) were restricted to the deep layer of DCN. Right: zoom-in of boxed region of the image in the middle.

(E) UMAP visualization of normalized expression of glutamate inhibitory signaling pathways (*Grm2, , Plcb1,*and *Kcnj6*, genes enriched in OFF UBCs) and glutamate excitatory signaling pathways (*Grm1, Plcb4,* and *Gria2,* genes enriched in ON UBC).

(F) Top: FISH co-staining for *Tfap2b* and *Slc6a5* (left), or for *Cacng3* and *Slc6a5* (middle), and FISH single-staining for *Grm2* (right) in CN sagittal sections. Bottom: zoom-in of boxed region of the images on the top. Arrows indicate double-labeled cells.

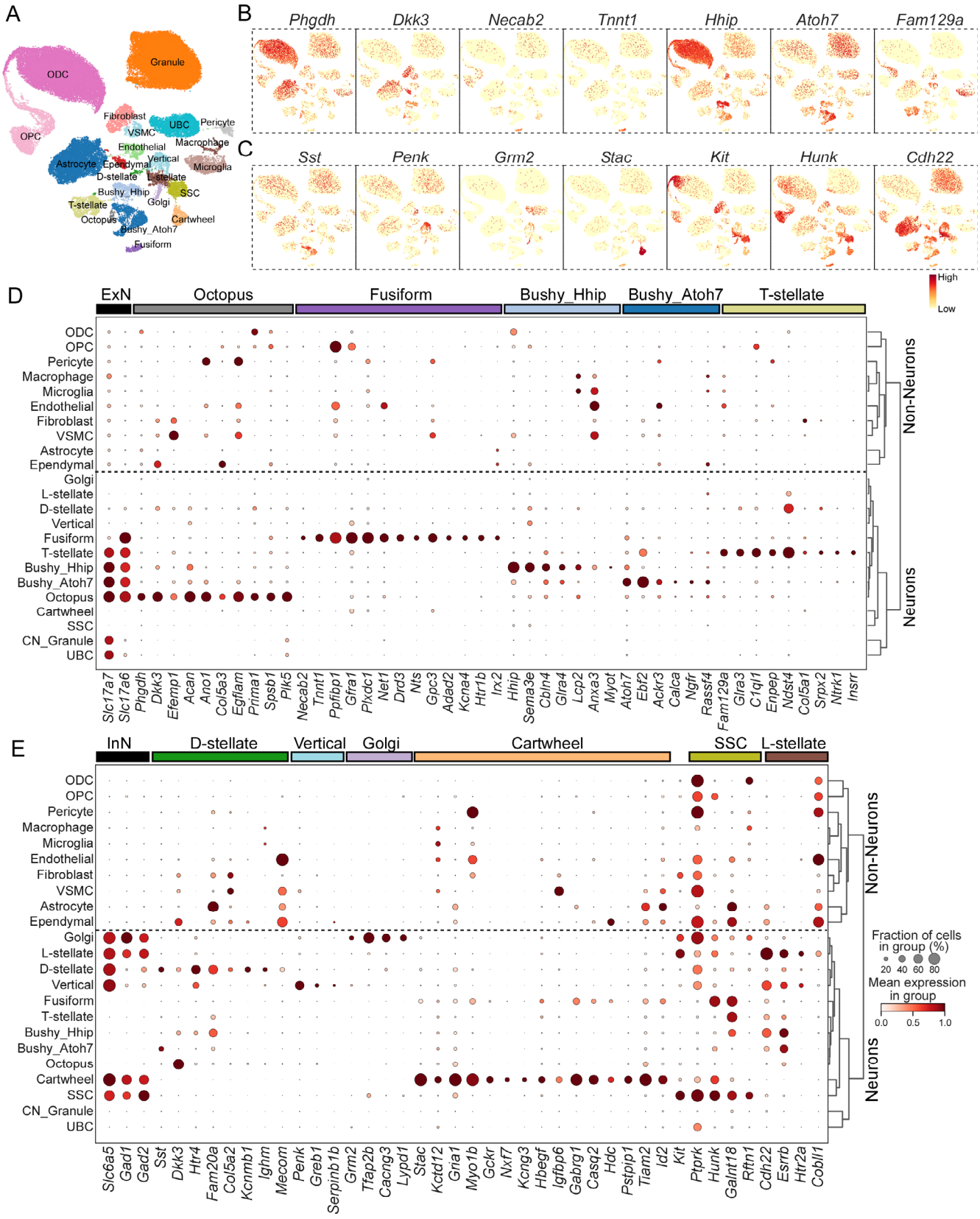

Figure S2. The expression of marker genes for major CN neuronal types. Related to Figure 3-6
(A) UMAP visualization of all CN nuclei (after profile quality control and annotation; Methods), colored by cell type and cluster identity.
(B) UMAP visualization of the normalized expression of the key discriminatory genes for each CN

excitatory cell type across all cell types.

(C) UMAP visualization of the expression of the key discriminatory genes for each CN inhibitory cell type across all cell types.

(D) Dendrogram indicating hierarchical relationships between cell types (or clusters, right) with a dot plot of scaled expression of selected marker genes for major excitatory cell types (left).

(E) Dendrogram indicating hierarchical relationships between cell types (or clusters) with a dot plot of scaled expression of selected marker genes for inhibitory cell types.

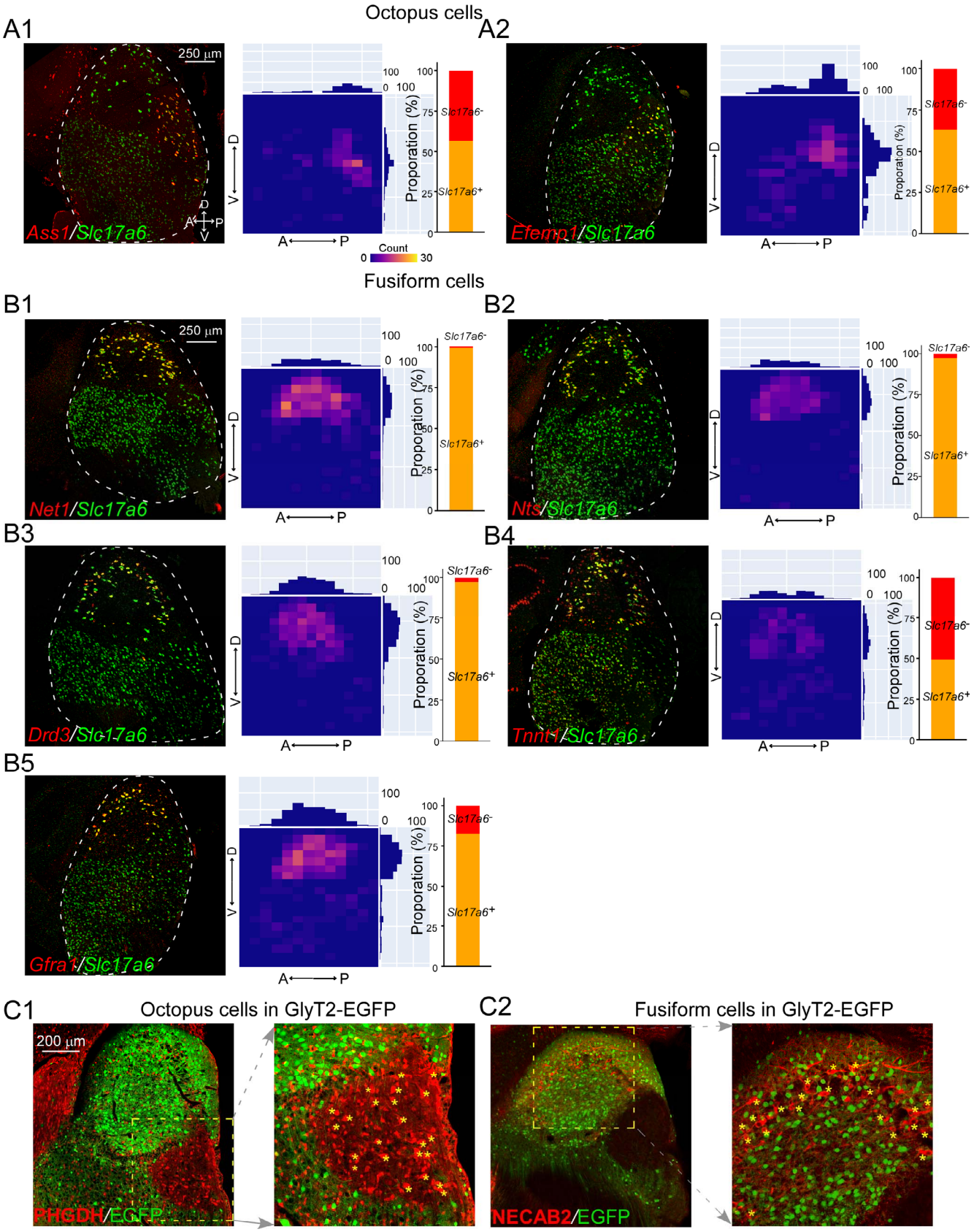

Figure S3: FISH staining and immunostaining of gene markers for fusiform cells and octopus cells. Related to Figure 3.

(A1) FISH co-staining for *Slc17a6* and *Ass1* in a representative CN sagittal section (left). Heatmap shows the density of double-labeled cells across the CN, and bar graph shows proportion of double-

labeled cells in all *Ass1*$^{+}$ cells.

(A2) FISH co-staining for *Slc17a6* and *Efemp1* in a sagittal section (left). Heatmap shows the density of double-labeled cells and bar graph shows proportion of double-labeled cells in all *Efemp1*$^{+}$ cells.

(B1) FISH co-staining for *Slc17a6* and *Net1* in a sagittal section (left). Heatmap shows density of double-labeled cells and bar graph shows proportion of double-labeled cells in all *Net1*$^{+}$ cells.

(B2) FISH co-staining for *Slc17a6* and *Drd3* in a sagittal section (left). Heatmap shows density of double-labeled cells and bar graph shows proportion of double-labeled cells in all *Drd3*$^{+}$ cells.

(B3) FISH co-staining for *Slc17a6* and *Tnnt1* in a sagittal section (left). Heatmap shows density of double-labeled cells and bar graph shows proportion of double-labeled cells in all *Tnnt1*$^{+}$ cells.

(B4) FISH co-staining for *Slc17a6* and *Nts* in a sagittal section (left). Heatmap shows density of double-labeled cells and bar graph shows proportion of double-labeled cells in all *Nts*$^{+}$ cells.

(B5) FISH co-staining for *Slc17a6* and *Gfra1* in a sagittal section (left). Heatmap shows density of double-labeled cells and bar graph shows proportion of double-labeled cells in all *Gfra1*$^{+}$ cells.

(C1) Immunostaining for Phgdh (red) in a sagittal section from GlyT2-EGFP mice (green EGFP indicates glycinergic neurons). Boxed region is magnified as on the right. Star signs (*) point to each soma with Phgdh signals. Labeled neurons are restricted to the OCA, which exhibits as a dark area under the fluorescent microscope due to a lack of glycinergic cells (Ngodup et al., 2020).

(C2) Immunostaining for Necab2 (red) in a sagittal section from GlyT2-EGFP mice. Boxed region is magnified as on the right. Star signs (*) point to each soma with Necab2 signals.

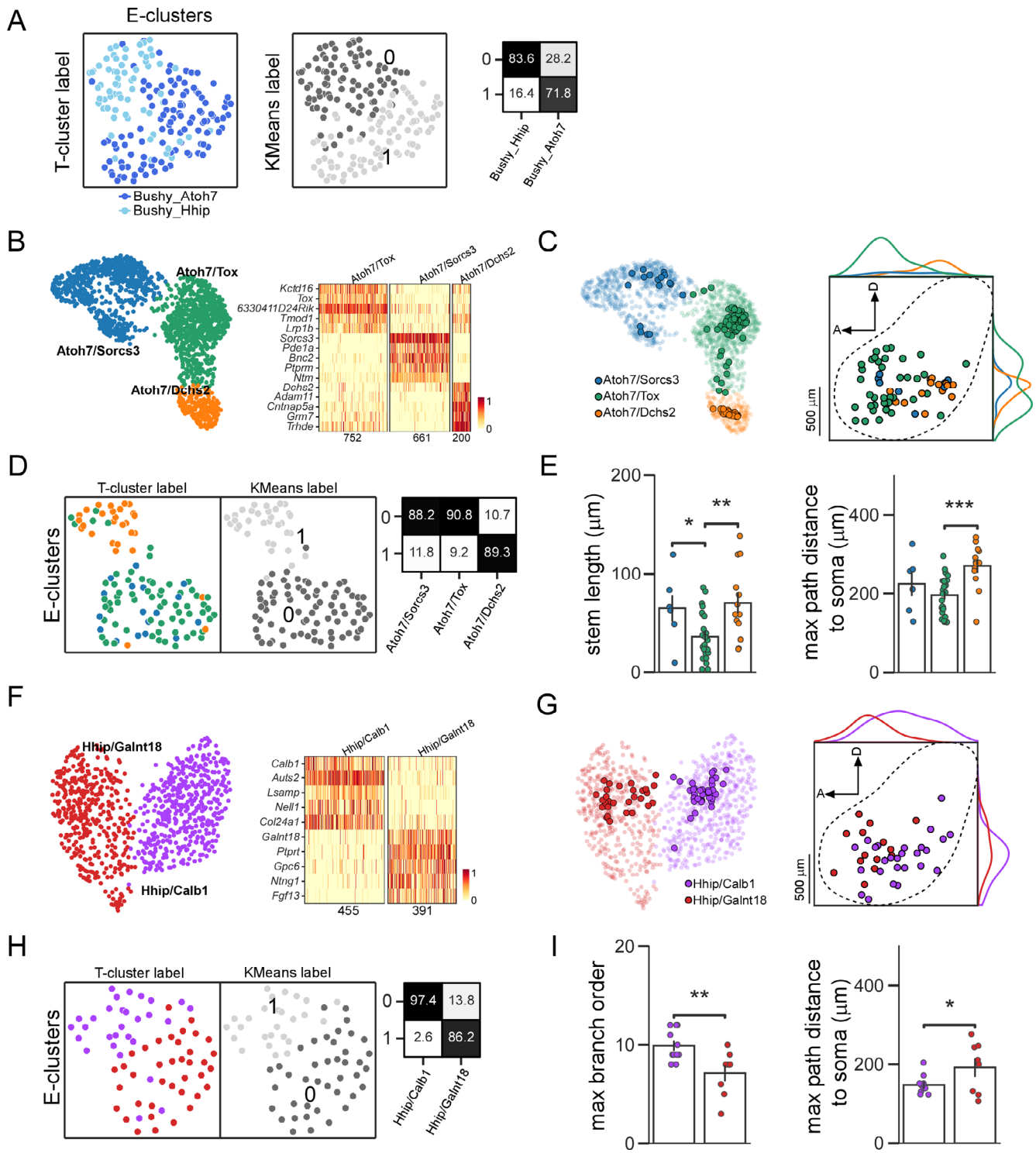

Figure S4. Molecular and phenotypic variability of bushy cells. Related to Figure 4

(A) Left: UMAP visualization of bushy cells by over-dispersed electrophysiological features, colored by subtypes (Bushy-Atoh7 and Bushy-Hhip). Middle: UMAP visualization of bushy cells by electrophysiological features, colored by K-means clusters (cluster 0 and 1). Right: Confusion matrix shows the performance of k-means clustering in distinguishing two molecular subtypes (an average of ~80% accuracy)

(B) Left: UMAP visualization of *Atoh7*$^{+}$ bushy cells, colored by subcluster (Atoh7/Sorcs3, Atoh7/Dchs2 and Atoh7/Tox). Right: Heat map showing normalized expression of the top 15 DEGs for three subclusters. Scalebar: Log2 (Expression level). The cell number in each subcluster is indicated below the figure.

(**C**) Left: All Patch-seq *Atoh7*$^+$ bushy cells mapped to each subcluster. Right: 2D spatial projection of each Patch-seq *Atoh7*$^+$ bushy cell to a sagittal view of CN, colored by the subcluster.

(**D**) Left: UMAP visualization of *Atoh7*$^+$ bushy cells by over-dispersed electrophysiological features, colored by subcluster. Middle: UMAP visualization of *Atoh7*$^+$bushy cells by electrophysiological features, colored by K-means clusters (Cluster 0 and 1). Right: Confusion matrix shows the performance of K-means clustering in distinguishing three subclusters.

(**E**) Two morphological features in three *Atoh7*$^+$ subclusters. For the other features see Table S3.

(F) Left: UMAP visualization of *Hhip*$^+$ bushy cells, colored by subcluster (Hhip/Galnt18; Hhip/Calb1). Right: Heat map showing normalized expression of the top 10 DEGs for two subclusters.

(**G**) Left: All Patch-seq *Hhip*$^+$ bushy cells mapped to each subcluster. Right: 2D spatial projection of each Patch-seq *Hhip*$^+$ bushy cell to a sagittal view of CN, colored by the subcluster.

(**H**) Left: UMAP visualization of *Hhip*$^+$ bushy cells by over-dispersed electrophysiological features, colored by subcluster. Middle: UMAP visualization of *Hhip*$^+$ bushy cells by electrophysiological features, colored by K-means clusters (cluster 0 and 1). Right: Confusion matrix shows the performance of k-means clustering in distinguishing two subclusters.

(**I**) Two morphological features in two *Hhip*$^+$ subclusters. For the other features see Table S3.

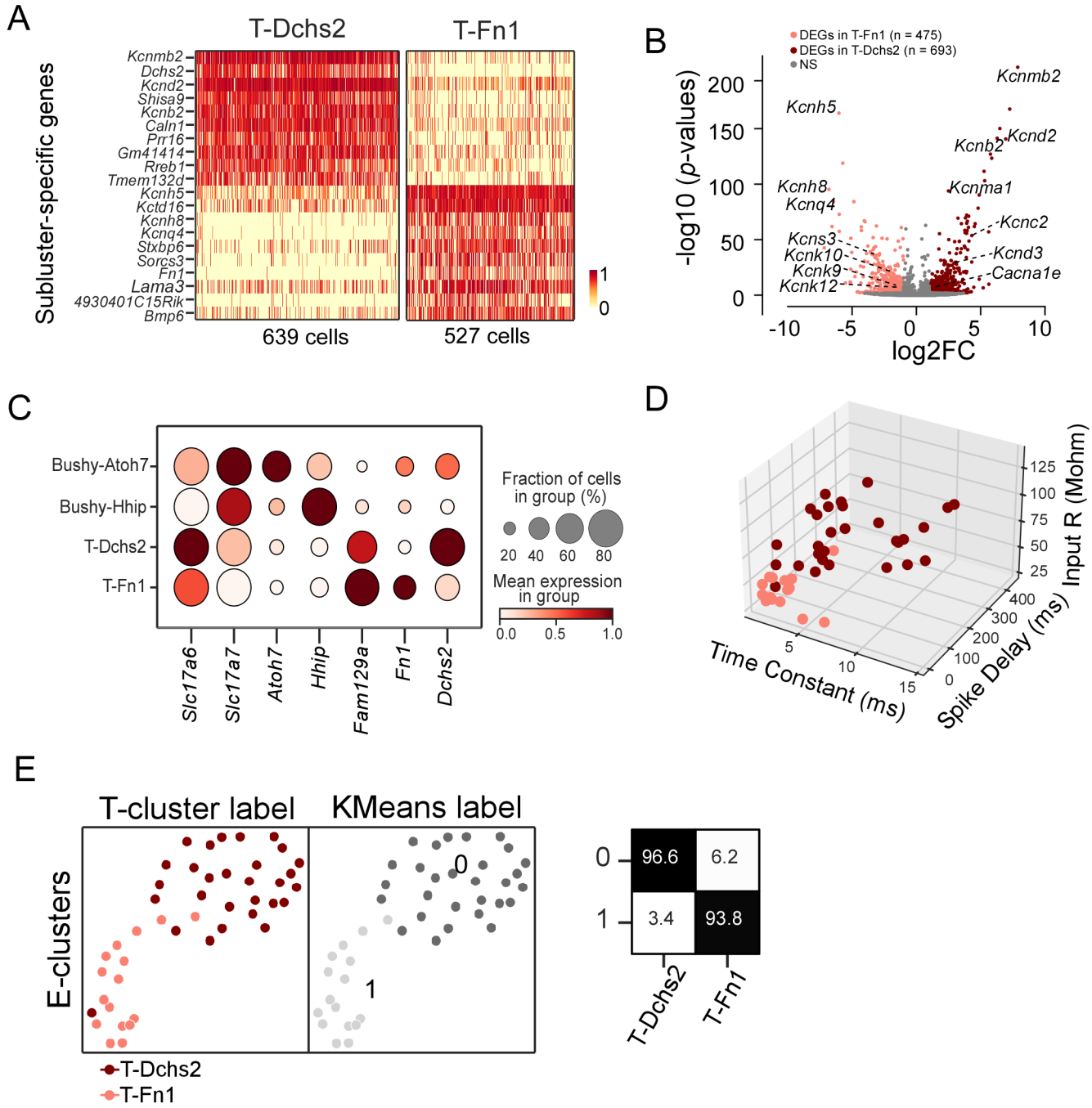

Figure S5. Molecular and phenotypic variation of T-stellate cells. Related to Figure 5

(A) Heat map showing normalized expression of the top 20 DEGs for two T-stellate cell subclusters.

(B) Volcano plot showing the log2 fold change (log2FC) and -log10(*p*-value) of detected genes comparing T-Fn1 to T- Dchs2. Among DEGs are 13 genes related to potassium channels and one gene related to calcium channel as labeled in the plot. NS: not significant

(C) Dot plot showing the expression patterns of each marker gene for bushy cell and T-stellate cell subtype based on Patch-seq.

(D) 3D plot of three electrophysiological features of T-stellate cell.

(E) Left: UMAP visualization of T-stellate cells clustered by over-dispersed electrophysiological features, colored by subtypes. Middle: UMAP visualization of T-stellate cells by electrophysiological features, colored by K-means clusters (Cluster 0 and 1). Right: Confusion matrix shows the performance of K-means clustering in distinguishing two subtypes.

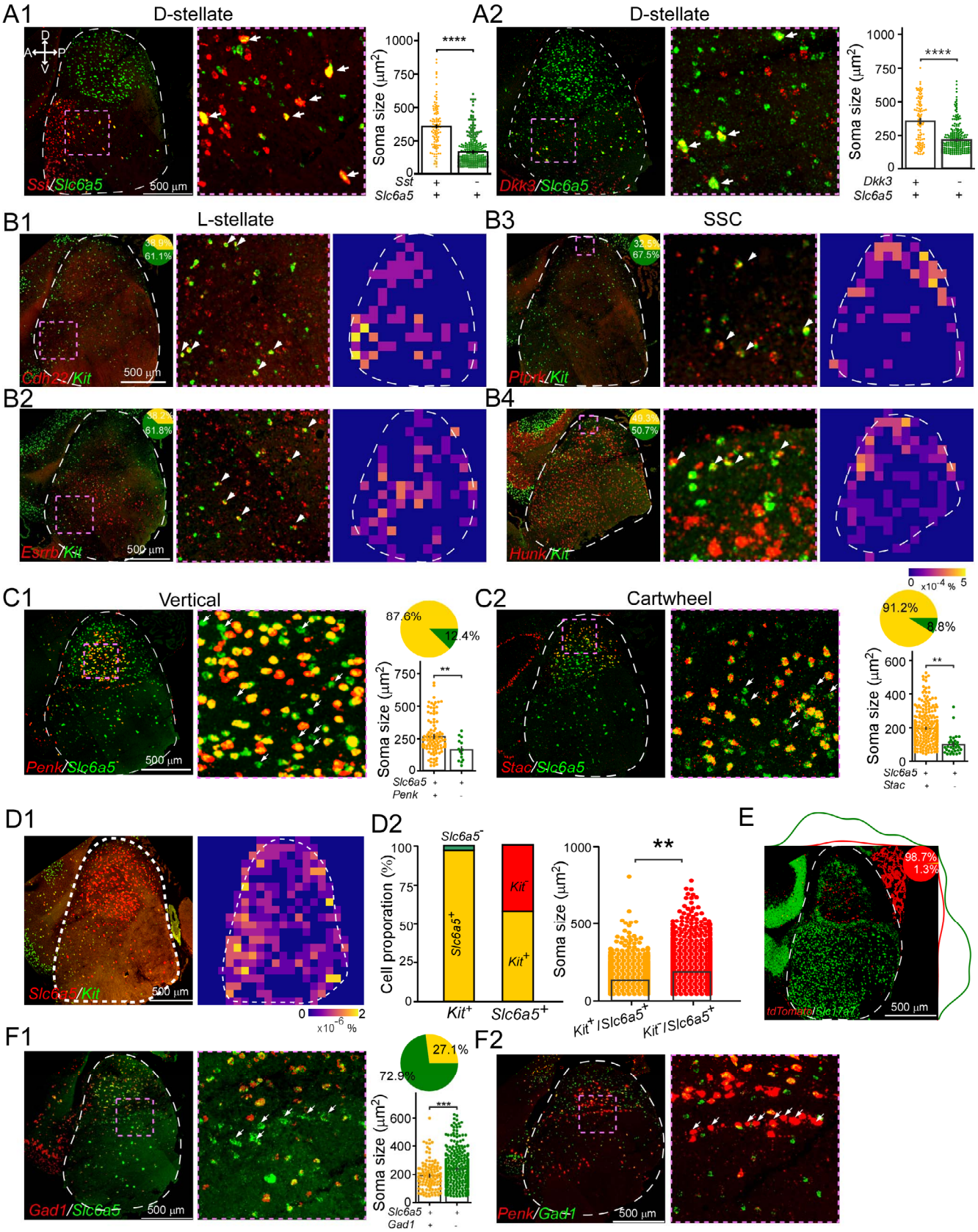

Figure S6: FISH staining for marker genes of inhibitory cell types. Related to Figure 6.

(A1) Left: FISH co-staining for *Sst* and *Slc6a5* in a representative CN sagittal section. Scalebar also applies to A2. Middle: Zoom-in of boxed region shown on the left. Right: soma size of Sst^{+} glycinergic neurons and Sst^{-} glycinergic neurons. ****$p < 0.0001$ with t-test.

(A2) Left: FISH co-staining for *Dkk3* and *Slc6a5*. Middle: zoom-in of boxed area shown on the left. Right: soma size of *Dkk3*$^+$ glycinergic neurons and *Dkk3*$^-$ glycinergic neurons. ****$p < 0.0001$ with t-test.

(B1) Left: FISH co-staining for *Cdh22* and *Kit*. Scalebar applies to B1-B4. Inset pie chart shows proportion of double-labeled cells in all *Kit*$^+$ cells. Middle: zoom-in of boxed region shown on the left. Right: distribution of double-labeled cells.

(B2) Left: FISH co-staining for *Esrrb* and *Kit*. Inset pie chart shows proportion of double-labeled cells in all *Kit*$^+$ cells. Middle: zoom-in of boxed region shown on the left. Right: distribution of double-labeled cells.

(B3) Left: FISH co-staining for *Ptprk* and *Kit*. Inset pie chart shows proportion of double-labeled cells in all *Kit*$^+$ cells. Middle: zoom-in of boxed region shown on the left. Right: distribution of double-labeled cells.

(B4) Left: FISH co-staining for *Hunk* and *Kit*. Inset pie chart shows proportion of double-labeled cells in all *Kit*$^+$ cells. Middle: zoom-in of boxed region shown on the left. Right: distribution of double-labeled cells.

(C1) Left: FISH co-staining for *Slc6a5* and *Penk*. Middle: zoom-in of boxed area shown on the left. Right: soma size of *Penk*$^-$/*Slc6a5*$^+$ cells and *Penk*$^+$/*Slc6a5*$^+$ cells. Pie chart shows proportion of *Penk*$^-$ glycinergic neurons and *Penk*$^+$ glycinergic neurons in deep layer of DCN.

(C2) Left: FISH co-staining for *Slc6a5* and *Stac*. Middle: zoom-in of boxed area shown on the left. Arrows point to those *Stac*$^-$/*Slc6a5*$^+$ cells. Right: soma size of *Stac*$^-$/*Slc6a5*$^+$ cells and *Stac*$^+$/*Slc6a5*$^+$ cells. Pie chart shows proportion of *Stac*$^-$ glycinergic neurons and *Stac*$^+$ glycinergic neurons in DCN.

(D1) Left: FISH co-staining for *Slc6a5* and *Kit*. Right: distribution of double-labeled cells.

(D2) Left: Bar graphs show proportion of double-labeled cells (*Slc6a5*$^+$/*Kit*$^+$) and single-labeled cells (*Slc6a5*$^-$/*Kit*$^+$) in all *Kit*$^+$ cells and proportion of *Kit*$^+$ glycinergic neurons (*Kit*$^+$/*Slc6a5*$^+$) and *Kit*$^-$ glycinergic neurons (*Kit*$^-$/*Slc6a5*$^+$). Note: only 2.8% of *Kit*$^+$ cells are *Slc6a5*$^-$. Right: soma size of *Kit*$^+$ glycinergic neurons and *Kit*$^-$ glycinergic neurons. **$p < 0.01$ with t-test.

(E) FISH co-staining for *Slc17a7* and *tdTomato* in Penk-Cre:Ai9 mice. Inset pie charts show the proportion of double-labeled cells in all *tdTomato*$^+$ cells. Colored lines along images show density of double-labeled neurons or single-labeled cells.

(F1) Left: FISH co-staining for *Slc6a5* and *Gad1*. Middle: zoom-in of boxed area shown on the left. Arrows point to those *Gad1*$^-$/*Slc6a5*$^+$ cells in small-cell cap. Right: soma size of *Gad1*$^-$/*Slc6a5*$^+$ cells and *Gad1*$^+$/*Slc6a5*$^+$ cells. Pie chart shows proportion of *Gad1*$^-$ glycinergic neurons and *Gad1*$^+$ glycinergic neurons in CN.

(F2) Left: FISH co-staining for *Penk* and *Gad1*. Right: zoom-in of boxed area shown on the left. Arrows point to those cells in small-cell cap that are *Penk*$^+$ but *Gad1*$^-$.

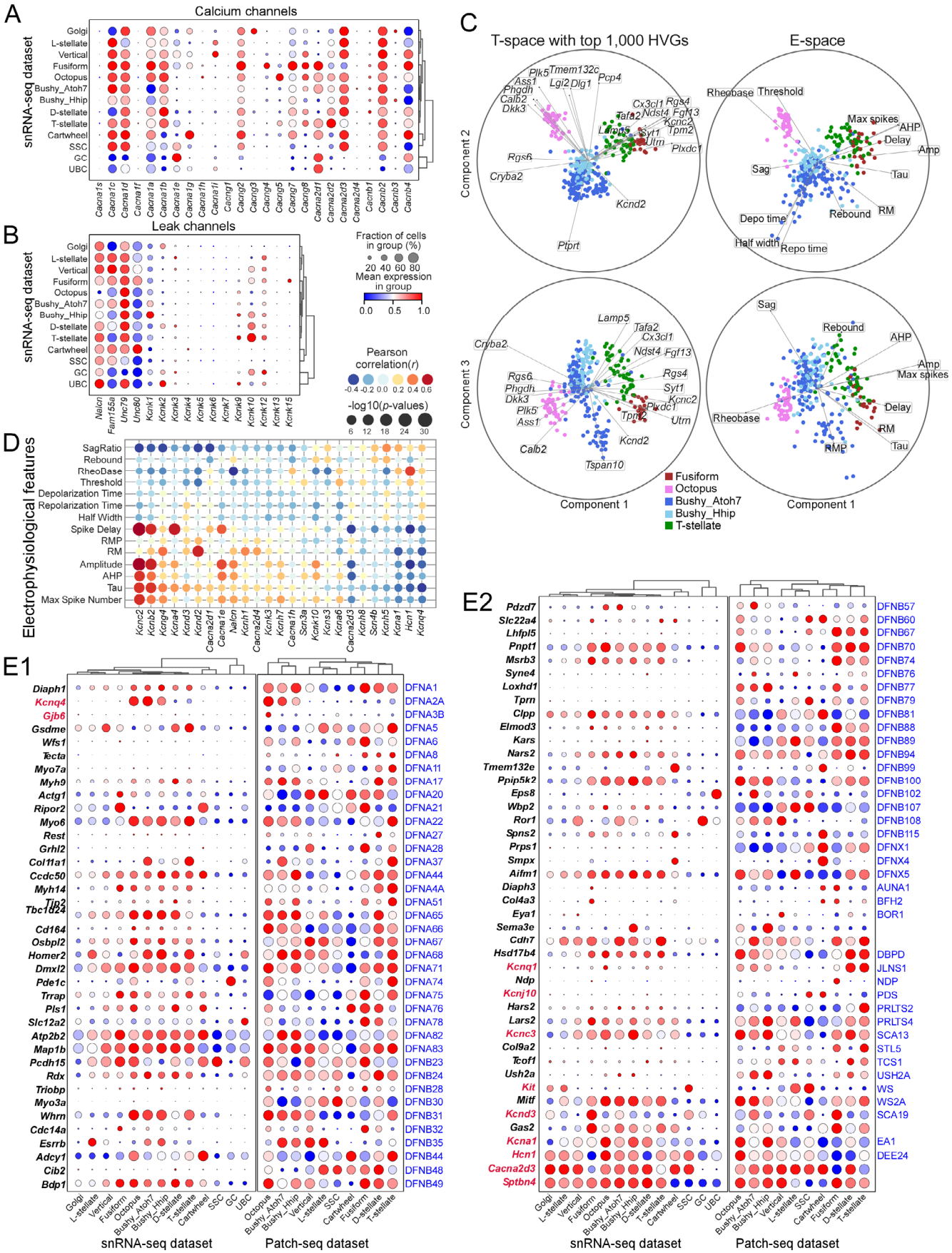

Figure S7: Single-cell transcriptomes provide insights into functional specializations of CN cell types. Related to Figure 7.

(A) Dot plot showing scaled expression of the genes encoding calcium channels (from snRNA-seq dataset).

(B) Dot plot showing scaled expression of the genes encoding leak channels and associated proteins (from snRNA-seq dataset).

(C) RRR model to predict electrophysiological features by top 1,000 highly variable genes (HVGs, cross-validated R^2 of 0.41). The models selected 25 genes and the cross-validated correlations between the first three pairs of projections were 0.87, 0.79, and 0.68.

(D) Dot plot showing the Pearson correlation between the predicted 25 ion channel genes and the electrophysiological features. Dot color depicts the correlation (r), and dot size depicts the -log10(p-values).

(E1-2) Dot plot showing scaled expression of 69 deafness genes (out of 128 known genes) and the genes whose mutations cause hearing loss in human syndromes and mice (Left: snRNA-seq dataset; Right: Patch-seq dataset). Those deafness genes (n=59) with low expression levels (< 20% fraction of the cell in any cell type in both dataset) were not included. AUNA1: auditory neuropathy, autosomal dominant 1; BFH2: benign familial hematuria; BOR1: Branchiooterenal syndrome 1; DBPD: D-bifunctional protein deficiency; JLNS1: Jervell and Lange-Nielsen syndrome; NDP: Norrie disease; PDS: Pendred's syndrome; PRLTS2: Perrault syndrome, type 2; PRLTS4: Perrault syndrome, type 4; SCA13: Spinocerebellar ataxia type 13; STL5: Stickler syndrome, type 5; TCS1: Treacher Collins syndrome-1; USH2A: Usher syndrome type II; WS: Williams syndrome; WS2A: Waardenburg syndrome type 2; SCA19: Spinocerebellar Ataxia Type 19. EA1: Episodic ataxia type 1, DEE24: Developmental and epileptic encephalopathy-24.

References

Apostolides, P.F., and Trussell, L.O. (2014). Chemical synaptic transmission onto superficial stellate cells of the mouse dorsal cochlear nucleus. J Neurophysiol *111*, 1812-1822.

Bal, R., and Oertel, D. (2000). Hyperpolarization-activated, mixed-cation current (I(h)) in octopus cells of the mammalian cochlear nucleus. J Neurophysiol *84*, 806-817.

Bal, R., and Oertel, D. (2001). Potassium currents in octopus cells of the mammalian cochlear nucleus. J Neurophysiol *86*, 2299-2311.

Bauer, C.K., and Schwarz, J.R. (2018). Ether-à-go-go K(+) channels: effective modulators of neuronal excitability. The Journal of physiology *596*, 769-783.

Beisel, K.W., Rocha-Sanchez, S.M., Morris, K.A., Nie, L., Feng, F., Kachar, B., Yamoah, E.N., and Fritzsch, B. (2005). Differential expression of KCNQ4 in inner hair cells and sensory neurons is the basis of progressive high-frequency hearing loss. J Neurosci *25*, 9285-9293.

Bellingham, M.C., Lim, R., and Walmsley, B. (1998). Developmental changes in EPSC quantal size and quantal content at a central glutamatergic synapse in rat. The Journal of physiology *511 (Pt 3)*, 861-869.

Blackburn, C.C., and Sachs, M.B. (1989). Classification of unit types in the anteroventral cochlear nucleus: PST histograms and regularity analysis. J Neurophysiol *62*, 1303-1329.

Bleakley, L.E., McKenzie, C.E., Soh, M.S., Forster, I.C., Pinares-Garcia, P., Sedo, A., Kathirvel, A., Churilov, L., Jancovski, N., Maljevic, S.*, et al.* (2021). Cation leak underlies neuronal excitability in an HCN1 developmental and epileptic encephalopathy. Brain *144*, 2060-2073.

Borges-Merjane, C., and Trussell, L.O. (2015). ON and OFF unipolar brush cells transform multisensory inputs to the auditory system. Neuron *85*, 1029-1042.

Brew, H.M., and Forsythe, I.D. (1995). Two voltage-dependent K+ conductances with complementary functions in postsynaptic integration at a central auditory synapse. J Neurosci *15*, 8011-8022.

Brownell, W.E. (1975). Organization of the cat trapezoid body and the discharge characteristics of its fibers. Brain Res *94*, 413-433.

Butler, B., and Lomber, S. (2013). Functional and structural changes throughout the auditory system following congenital and early-onset deafness: implications for hearing restoration. Frontiers in Systems Neuroscience *7*.

Cadwell, C.R., Palasantza, A., Jiang, X., Berens, P., Deng, Q., Yilmaz, M., Reimer, J., Shen, S., Bethge, M., Tolias, K.F.*, et al.* (2016). Electrophysiological, transcriptomic and morphologic profiling of single neurons using Patch-seq. Nat Biotechnol *34*, 199-203.

Cadwell, C.R., Scala, F., Fahey, P.G., Kobak, D., Mulherkar, S., Sinz, F.H., Papadopoulos, S., Tan, Z.H., Johnsson, P., Hartmanis, L.*, et al.* (2020). Cell type composition and circuit organization of clonally related excitatory neurons in the juvenile mouse neocortex. Elife *9*.

Cadwell, C.R., Scala, F., Li, S., Livrizzi, G., Shen, S., Sandberg, R., Jiang, X., and Tolias, A.S. (2017). Multimodal profiling of single-cell morphology, electrophysiology, and gene expression using Patch-seq. Nat Protoc *12*, 2531-2553.

Callaway, E.M., Dong, H.-W., Ecker, J.R., Hawrylycz, M.J., Huang, Z.J., Lein, E.S., Ngai, J., Osten, P., Ren, B., Tolias, A.S.*, et al.* (2021). A multimodal cell census and atlas of the mammalian primary motor cortex. Nature *598*, 86-102.

Campos, M.L., de Cabo, C., Wisden, W., Juiz, J.M., and Merlo, D. (2001). Expression of GABAA receptor subunits in rat brainstem auditory pathways: cochlear nuclei, superior olivary complex and nucleus of the lateral lemniscus. Neuroscience *102*, 625-638.

Cant, N.B. (1993). The synaptic organization of the ventral cochlear nucleus of the cat: the peripheral cap of small cells. In The Mammalian Cochlear Nuclei (Springer), pp. 91-105.

Cao, X.J., and Oertel, D. (2011). The magnitudes of hyperpolarization-activated and low-voltage-activated potassium currents co-vary in neurons of the ventral cochlear nucleus. J Neurophysiol *106*, 630-640.
Cao, X.J., Shatadal, S., and Oertel, D. (2007). Voltage-sensitive conductances of bushy cells of the Mammalian ventral cochlear nucleus. J Neurophysiol *97*, 3961-3975.
Chi, T., Ru, P., and Shamma, S.A. (2005). Multiresolution spectrotemporal analysis of complex sounds. The Journal of the Acoustical Society of America *118*, 887-906.
Clayton, K.K., Williamson, R.S., Hancock, K.E., Tasaka, G.I., Mizrahi, A., Hackett, T.A., and Polley, D.B. (2021). Auditory Corticothalamic Neurons Are Recruited by Motor Preparatory Inputs. Curr Biol *31*, 310-321 e315.
Connor, J.A., and Stevens, C.F. (1971). Prediction of repetitive firing behaviour from voltage clamp data on an isolated neurone soma. The Journal of physiology *213*, 31-53.
Dobin, A., Davis, C.A., Schlesinger, F., Drenkow, J., Zaleski, C., Jha, S., Batut, P., Chaisson, M., and Gingeras, T.R. (2013). STAR: ultrafast universal RNA-seq aligner. Bioinformatics *29*, 15-21.
Doucet, J.R., and Ryugo, D.K. (1997). Projections from the ventral cochlear nucleus to the dorsal cochlear nucleus in rats. The Journal of comparative neurology *385*, 245-264.
Doucet, J.R., and Ryugo, D.K. (2006). Structural and functional classes of multipolar cells in the ventral cochlear nucleus. Anat Rec A Discov Mol Cell Evol Biol *288*, 331-344.
Eatock, R.A., Xue, J., and Kalluri, R. (2008). Ion channels in mammalian vestibular afferents may set regularity of firing. J Exp Biol *211*, 1764-1774.
Englund, C., Kowalczyk, T., Daza, R.A.M., Dagan, A., Lau, C., Rose, M.F., and Hevner, R.F. (2006). Unipolar Brush Cells of the Cerebellum Are Produced in the Rhombic Lip and Migrate through Developing White Matter. The Journal of Neuroscience *26*, 9184-9195.
Futai, K., Okada, M., Matsuyama, K., and Takahashi, T. (2001). High-fidelity transmission acquired via a developmental decrease in NMDA receptor expression at an auditory synapse. J Neurosci *21*, 3342-3349.
Gardner, S.M., Trussell, L.O., and Oertel, D. (1999). Time course and permeation of synaptic AMPA receptors in cochlear nuclear neurons correlate with input. J Neurosci *19*, 8721-8729.
Gardner, S.M., Trussell, L.O., and Oertel, D. (2001). Correlation of AMPA receptor subunit composition with synaptic input in the mammalian cochlear nuclei. J Neurosci *21*, 7428-7437.
Gates, T.S., Weedman, D.L., Pongstaporn, T., and Ryugo, D.K. (1996). Immunocytochemical localization of glycine in a subset of cartwheel cells of the dorsal cochlear nucleus in rats. Hear Res *96*, 157-166.
Gayoso, A., Lopez, R., Xing, G., Boyeau, P., Valiollah Pour Amiri, V., Hong, J., Wu, K., Jayasuriya, M., Mehlman, E., Langevin, M.*, et al.* (2022). A Python library for probabilistic analysis of single-cell omics data. Nature Biotechnology *40*, 163-166.
Golding, N.L., Ferragamo, M.J., and Oertel, D. (1999). Role of intrinsic conductances underlying responses to transients in octopus cells of the cochlear nucleus. J Neurosci *19*, 2897-2905.
Goyer, D., Kurth, S., Gillet, C., Keine, C., Rübsamen, R., and Kuenzel, T. (2016). Slow Cholinergic Modulation of Spike Probability in Ultra-Fast Time-Coding Sensory Neurons. eNeuro *3*.
Griffiths, T.D. (2002). Central auditory processing disorders. Curr Opin Neurol *15*, 31-33.
Grothe, B., Pecka, M., and McAlpine, D. (2010). Mechanisms of Sound Localization in Mammals. Physiological Reviews *90*, 983-1012.
Guo, C., Huson, V., Macosko, E.Z., and Regehr, W.G. (2021). Graded heterogeneity of metabotropic signaling underlies a continuum of cell-intrinsic temporal responses in unipolar brush cells. Nature Communications *12*, 5491.
Hancock, K.E., and Voigt, H.F. (2002a). Intracellularly labeled fusiform cells in dorsal cochlear nucleus of the gerbil. I. Physiological response properties. J Neurophysiol *87*, 2505-2519.

Hancock, K.E., and Voigt, H.F. (2002b). Intracellularly labeled fusiform cells in dorsal cochlear nucleus of the gerbil. II. Comparison of physiology and anatomy. J Neurophysiol *87*, 2520-2530.
Heidenreich, M., Lechner, S.G., Vardanyan, V., Wetzel, C., Cremers, C.W., De Leenheer, E.M., Aránguez, G., Moreno-Pelayo, M.Á., Jentsch, T.J., and Lewin, G.R. (2012). KCNQ4 K+ channels tune mechanoreceptors for normal touch sensation in mouse and man. Nature Neuroscience *15*, 138-145.
Henze, D.A., and Buzsaki, G. (2001). Action potential threshold of hippocampal pyramidal cells in vivo is increased by recent spiking activity. Neuroscience *105*, 121-130.
Irie, T., Fukui, I., and Ohmori, H. (2006). Activation of GIRK channels by muscarinic receptors and group II metabotropic glutamate receptors suppresses Golgi cell activity in the cochlear nucleus of mice. J Neurophysiol *96*, 2633-2644.
Ison, J.R., Allen, P.D., and Oertel, D. (2017). Deleting the HCN1 Subunit of Hyperpolarization-Activated Ion Channels in Mice Impairs Acoustic Startle Reflexes, Gap Detection, and Spatial Localization. Journal of the Association for Research in Otolaryngology : JARO *18*, 427-440.
Jiang, X., Shen, S., Cadwell, C.R., Berens, P., Sinz, F., Ecker, A.S., Patel, S., and Tolias, A.S. (2015). Principles of connectivity among morphologically defined cell types in adult neocortex. Science *350*, aac9462.
Johnston, J., Forsythe, I.D., and Kopp-Scheinpflug, C. (2010). Going native: voltage-gated potassium channels controlling neuronal excitability. The Journal of physiology *588*, 3187-3200.
Johnston, J., Griffin, S.J., Baker, C., Skrzypiec, A., Chernova, T., and Forsythe, I.D. (2008). Initial segment Kv2.2 channels mediate a slow delayed rectifier and maintain high frequency action potential firing in medial nucleus of the trapezoid body neurons. The Journal of physiology *586*, 3493-3509.
Kalluri, R., Xue, J., and Eatock, R.A. (2010). Ion channels set spike timing regularity of mammalian vestibular afferent neurons. J Neurophysiol *104*, 2034-2051.
Kanold, P.O., and Manis, P.B. (1999). Transient potassium currents regulate the discharge patterns of dorsal cochlear nucleus pyramidal cells. J Neurosci *19*, 2195-2208.
Karcz, A., Allen, P.D., Walton, J., Ison, J.R., and Kopp-Scheinpflug, C. (2015). Auditory deficits of Kcna1 deletion are similar to those of a monaural hearing impairment. Hear Res *321*, 45-51.
Kharkovets, T., Hardelin, J.P., Safieddine, S., Schweizer, M., El-Amraoui, A., Petit, C., and Jentsch, T.J. (2000). KCNQ4, a K+ channel mutated in a form of dominant deafness, is expressed in the inner ear and the central auditory pathway. Proceedings of the National Academy of Sciences of the United States of America *97*, 4333-4338.
Kobak, D., and Berens, P. (2019). The art of using t-SNE for single-cell transcriptomics. Nature Communications *10*, 5416.
Kobak, D., Bernaerts, Y., Weis, M.A., Scala, F., Tolias, A.S., and Berens, P. (2021). Sparse reduced‐rank regression for exploratory visualisation of paired multivariate data. Journal of the Royal Statistical Society Series C *70*, 980-1000.
Kolston, J., Osen, K.K., Hackney, C.M., Ottersen, O.P., and Storm-Mathisen, J. (1992). An atlas of glycine- and GABA-like immunoreactivity and colocalization in the cochlear nuclear complex of the guinea pig. Anat Embryol (Berl) *186*, 443-465.
Kopp-Scheinpflug, C., and Tempel, B.L. (2015). Decreased temporal precision of neuronal signaling as a candidate mechanism of auditory processing disorder. Hear Res *330*, 213-220.
Korsunsky, I., Millard, N., Fan, J., Slowikowski, K., Zhang, F., Wei, K., Baglaenko, Y., Brenner, M., Loh, P.R., and Raychaudhuri, S. (2019). Fast, sensitive and accurate integration of single-cell data with Harmony. Nat Methods *16*, 1289-1296.
Kozareva, V., Martin, C., Osorno, T., Rudolph, S., Guo, C., Vanderburg, C., Nadaf, N., Regev, A., Regehr, W.G., and Macosko, E. (2021). A transcriptomic atlas of mouse cerebellar cortex comprehensively defines cell types. Nature *598*, 214-219.

Krishnaswami, S.R., Grindberg, R.V., Novotny, M., Venepally, P., Lacar, B., Bhutani, K., Linker, S.B., Pham, S., Erwin, J.A., Miller, J.A., *et al.* (2016). Using single nuclei for RNA-seq to capture the transcriptome of postmortem neurons. Nat Protoc *11*, 499-524.
Laturnus, S., von Daranyi, A., Huang, Z., and Berens, P. (2020). MorphoPy: A python package for feature extraction of neural morphologies. Journal of Open Source Software *5*, 2339.
Lau, D., Miera, E.V.-S.d., Contreras, D., Ozaita, A., Harvey, M., Chow, A., Noebels, J.L., Paylor, R., Morgan, J.I., Leonard, C.S., *et al.* (2000). Impaired Fast-Spiking, Suppressed Cortical Inhibition, and Increased Susceptibility to Seizures in Mice Lacking Kv3.2 K⁺ Channel Proteins. The Journal of Neuroscience *20*, 9071-9085.
Lauer, A.M., Connelly, C.J., Graham, H., and Ryugo, D.K. (2013). Morphological characterization of bushy cells and their inputs in the laboratory mouse (Mus musculus) anteroventral cochlear nucleus. PLoS One *8*, e73308.
Leão, R.M. (2019). The ion channels and synapses responsible for the physiological diversity of mammalian lower brainstem auditory neurons. Hearing Research *376*, 33-46.
Lein, E.S., Hawrylycz, M.J., Ao, N., Ayres, M., Bensinger, A., Bernard, A., Boe, A.F., Boguski, M.S., Brockway, K.S., Byrnes, E.J., *et al.* (2007). Genome-wide atlas of gene expression in the adult mouse brain. Nature *445*, 168-176.
Liao, Y., Smyth, G.K., and Shi, W. (2014). featureCounts: an efficient general purpose program for assigning sequence reads to genomic features. Bioinformatics *30*, 923-930.
Liberman, M.C. (1991). Central projections of auditory-nerve fibers of differing spontaneous rate. I. Anteroventral cochlear nucleus. The Journal of comparative neurology *313*, 240-258.
Lin, S., and Xie, R. (2019). Principal Neurons in the Anteroventral Cochlear Nucleus Express Cell-Type Specific Glycine Receptor alpha Subunits. Neuroscience *415*, 77-88.
Lu, H.W., Smith, P.H., and Joris, P.X. (2022). Mammalian octopus cells are direction selective to frequency sweeps by excitatory synaptic sequence detection. Proceedings of the National Academy of Sciences of the United States of America *119*, e2203748119.
Luecken, M.D., and Theis, F.J. (2019). Current best practices in single-cell RNA-seq analysis: a tutorial. Mol Syst Biol *15*, e8746.
Macosko, E.Z., Basu, A., Satija, R., Nemesh, J., Shekhar, K., Goldman, M., Tirosh, I., Bialas, A.R., Kamitaki, N., Martersteck, E.M., *et al.* (2015). Highly Parallel Genome-wide Expression Profiling of Individual Cells Using Nanoliter Droplets. Cell *161*, 1202-1214.
Manis, P., Xie, R., Wang, Y., Marrs, G., Spirou, G., Trussell, L., Popper, A., and Fay, R. (2011). Synaptic mechanisms in the auditory system (Springer New York), pp. 61-93.
Manis, P.B., Kasten, M.R., and Xie, R. (2019). Classification of neurons in the adult mouse cochlear nucleus: Linear discriminant analysis. PLoS One *14*, e0223137.
Manis, P.B., and Marx, S.O. (1991). Outward currents in isolated ventral cochlear nucleus neurons. J Neurosci *11*, 2865-2880.
Martin, M.R. (1981). Morphology of the cochlear nucleus of the normal and reeler mutant mouse. The Journal of comparative neurology *197*, 141-152.
Martin, M.R., and Rickets, C. (1981). Histogenesis of the cochlear nucleus of the mouse. The Journal of comparative neurology *197*, 169-184.
McGinley, M.J., Liberman, M.C., Bal, R., and Oertel, D. (2012). Generating synchrony from the asynchronous: compensation for cochlear traveling wave delays by the dendrites of individual brainstem neurons. J Neurosci *32*, 9301-9311.
Mickelsen, L.E., Bolisetty, M., Chimileski, B.R., Fujita, A., Beltrami, E.J., Costanzo, J.T., Naparstek, J.R., Robson, P., and Jackson, A.C. (2019). Single-cell transcriptomic analysis of the lateral hypothalamic area reveals molecularly distinct populations of inhibitory and excitatory neurons. Nat Neurosci *22*, 642-656.

Middlebrooks, J.C., Nick, H.S., Subramony, S.H., Advincula, J., Rosales, R.L., Lee, L.V., Ashizawa, T., and Waters, M.F. (2013). Mutation in the kv3.3 voltage-gated potassium channel causing spinocerebellar ataxia 13 disrupts sound-localization mechanisms. PLoS One *8*, e76749.
Ming Hu, X.J. (2022). PatchView: A Python Package for Patch-clamp Data Analysis and Visualization. Journal of Open Source Software *7*, 4706.
Mukamel, E.A., and Ngai, J. (2019). Perspectives on defining cell types in the brain. Curr Opin Neurobiol *56*, 61-68.
Ngodup, T., Goetz, J.A., McGuire, B.C., Sun, W., Lauer, A.M., and Xu-Friedman, M.A. (2015). Activity-dependent, homeostatic regulation of neurotransmitter release from auditory nerve fibers. Proceedings of the National Academy of Sciences of the United States of America *112*, 6479-6484.
Ngodup, T., Romero, G.E., and Trussell, L.O. (2020). Identification of an inhibitory neuron subtype, the L-stellate cell of the cochlear nucleus. Elife *9*.
Oertel, D., McGinley, M., and and Cao, X.-J. (2009). Temporal processing in the auditory pathway. In Encylopedia of Neuroscience.
Oertel, D., Wu, S.H., Garb, M.W., and Dizack, C. (1990). Morphology and physiology of cells in slice preparations of the posteroventral cochlear nucleus of mice. The Journal of comparative neurology *295*, 136-154.
Palmer, A.R. (1987). Physiology of the cochlear nerve and cochlear nucleus. British Medical Bulletin *43*, 838-855.
Perney, T.M., and Kaczmarek, L.K. (1997). Localization of a high threshold potassium channel in the rat cochlear nucleus. The Journal of comparative neurology *386*, 178-202.
Petralia, R.S., Rubio, M.E., Wang, Y.X., and Wenthold, R.J. (2000). Differential distribution of glutamate receptors in the cochlear nuclei. Hear Res *147*, 59-69.
Petralia, R.S., Wang, Y.X., Zhao, H.M., and Wenthold, R.J. (1996). Ionotropic and metabotropic glutamate receptors show unique postsynaptic, presynaptic, and glial localizations in the dorsal cochlear nucleus. The Journal of comparative neurology *372*, 356-383.
Polański, K., Young, M.D., Miao, Z., Meyer, K.B., Teichmann, S.A., and Park, J.-E. (2019). BBKNN: fast batch alignment of single cell transcriptomes. Bioinformatics *36*, 964-965.
Rhode, W.S., and Greenberg, S. (1992). Physiology of the Cochlear Nuclei. In The Mammalian Auditory Pathway: Neurophysiology, A.N. Popper, and R.R. Fay, eds. (New York, NY: Springer New York), pp. 94-152.
Rhode, W.S., Oertel, D., and Smith, P.H. (1983). Physiological response properties of cells labeled intracellularly with horseradish peroxidase in cat ventral cochlear nucleus. The Journal of comparative neurology *213*, 448-463.
Romero, G.E. (2021). CENTRAL CIRCUITRY UNDERLYING THE MEDIAL OLIVOCOCHLEAR EFFERENT SYSTEM. In Department of Physiology & Pharmacology (Oregon Health & Science University School of Medicine).
Roos, M.J., and May, B.J. (2012). Classification of unit types in the anteroventral cochlear nucleus of laboratory mice. Hear Res *289*, 13-26.
Rothman, J.S., and Manis, P.B. (2003). The roles potassium currents play in regulating the electrical activity of ventral cochlear nucleus neurons. J Neurophysiol *89*, 3097-3113.
Ruan, H.B., Zhang, N., and Gao, X. (2005). Identification of a novel point mutation of mouse proto-oncogene c-kit through N-ethyl-N-nitrosourea mutagenesis. Genetics *169*, 819-831.
Rubio, M.E., Matsui, K., Fukazawa, Y., Kamasawa, N., Harada, H., Itakura, M., Molnár, E., Abe, M., Sakimura, K., and Shigemoto, R. (2017). The number and distribution of AMPA receptor channels containing fast kinetic GluA3 and GluA4 subunits at auditory nerve synapses depend on the target cells. Brain structure & function *222*, 3375-3393.
Rudy, B., and McBain, C.J. (2001). Kv3 channels: voltage-gated K+ channels designed for high-frequency repetitive firing. Trends in Neurosciences *24*, 517-526.

Saint Marie, R.L., Benson, C.G., Ostapoff, E.M., and Morest, D.K. (1991). Glycine immunoreactive projections from the dorsal to the anteroventral cochlear nucleus. Hearing Research *51*, 11-28.
Saunders, A., Macosko, E.Z., Wysoker, A., Goldman, M., Krienen, F.M., de Rivera, H., Bien, E., Baum, M., Bortolin, L., Wang, S.*, et al.* (2018). Molecular Diversity and Specializations among the Cells of the Adult Mouse Brain. Cell *174*, 1015-1030.e1016.
Scala, F., Kobak, D., Bernabucci, M., Bernaerts, Y., Cadwell, C.R., Castro, J.R., Hartmanis, L., Jiang, X., Laturnus, S., Miranda, E.*, et al.* (2021). Phenotypic variation of transcriptomic cell types in mouse motor cortex. Nature *598*, 144-150.
Scala, F., Kobak, D., Shan, S., Bernaerts, Y., Laturnus, S., Cadwell, C.R., Hartmanis, L., Castro, J., Tan, Z.H., Sandberg, R.*, et al.* (2018). Neocortical layer 4 in adult mouse differs in major cell types and circuit organization between primary sensory areas. bioRxiv, 507293.
Schweitzer, L., and Cant, N.B. (1985). Differentiation of the giant and fusiform cells in the dorsal cochlear nucleus of the hamster. Brain Res *352*, 69-82.
Shibata, R., Nakahira, K., Shibasaki, K., Wakazono, Y., Imoto, K., and Ikenaka, K. (2000). A-Type K⁺ Current Mediated by the Kv4 Channel Regulates the Generation of Action Potential in Developing Cerebellar Granule Cells. The Journal of Neuroscience *20*, 4145-4155.
Spritz, R.A., and Beighton, P. (1998). Piebaldism with deafness: molecular evidence for an expanded syndrome. American journal of medical genetics *75*, 101-103.
Tasic, B., Yao, Z., Graybuck, L.T., Smith, K.A., Nguyen, T.N., Bertagnolli, D., Goldy, J., Garren, E., Economo, M.N., Viswanathan, S.*, et al.* (2018). Shared and distinct transcriptomic cell types across neocortical areas. Nature *563*, 72-78.
Tolbert, L.P., Morest, D.K., and Yurgelun-Todd, D.A. (1982). The neuronal architecture of the anteroventral cochlear nucleus of the cat in the region of the cochlear nerve root: horseradish peroxidase labelling of identified cell types. Neuroscience *7*, 3031-3052.
Tomlinson, S.E., Rajakulendran, S., Tan, S.V., Graves, T.D., Bamiou, D.E., Labrum, R.W., Burke, D., Sue, C.M., Giunti, P., Schorge, S.*, et al.* (2013). Clinical, genetic, neurophysiological and functional study of new mutations in episodic ataxia type 1. J Neurol Neurosurg Psychiatry *84*, 1107-1112.
Trussell, L.O. (1999). Synaptic mechanisms for coding timing in auditory neurons. Annual review of physiology *61*, 477-496.
Trussell, L.O. (2019). 123In Vitro Studies of Neuromodulation and Plasticity in the Dorsal Cochlear Nucleus. In The Oxford Handbook of the Auditory Brainstem, K. Kandler, ed. (Oxford University Press), p. 0.
Trussell, L.O., and Oertel, D. (2018). Microcircuits of the Dorsal Cochlear Nucleus. In The Mammalian Auditory Pathways: Synaptic Organization and Microcircuits, D.L. Oliver, N.B. Cant, R.R. Fay, and A.N. Popper, eds. (Cham: Springer International Publishing), pp. 73-99.
Varecka, L., Wu, C.-H., Rotter, A., and Frostholm, A. (1994). GABAA/benzodiazepine receptor α6 subunit mRNA in granule cells of the cerebellar cortex and cochlear nuclei: Expression in developing and mutant mice. Journal of Comparative Neurology *339*, 341-352.
Wang, L.Y., Gan, L., Forsythe, I.D., and Kaczmarek, L.K. (1998a). Contribution of the Kv3.1 potassium channel to high-frequency firing in mouse auditory neurones. The Journal of physiology *509 (Pt 1)*, 183-194.
Wang, Y.-X., Wenthold, R.J., Ottersen, O.P., and Petralia, R.S. (1998b). Endbulb Synapses in the Anteroventral Cochlear Nucleus Express a Specific Subset of AMPA-Type Glutamate Receptor Subunits. The Journal of Neuroscience *18*, 1148-1160.
Watanabe, T., Shimazaki, T., and Oda, Y. (2017). Coordinated Expression of Two Types of Low-Threshold K(+) Channels Establishes Unique Single Spiking of Mauthner Cells among Segmentally Homologous Neurons in the Zebrafish Hindbrain. eNeuro *4*.
Webster, D.B., and Trune, D.R. (1982). Cochlear nuclear complex of mice. The American journal of anatomy *163*, 103-130.

Wickesberg, R.E., and Oertel, D. (1990). Delayed, frequency-specific inhibition in the cochlear nuclei of mice: a mechanism for monaural echo suppression. J Neurosci *10*, 1762-1768.
Wolf, F.A., Angerer, P., and Theis, F.J. (2018). SCANPY: large-scale single-cell gene expression data analysis. Genome Biol *19*, 15.
Wolock, S.L., Lopez, R., and Klein, A.M. (2019). Scrublet: Computational Identification of Cell Doublets in Single-Cell Transcriptomic Data. Cell Syst *8*, 281-291 e289.
Wong, K., Kozin, E.D., Kanumuri, V.V., Vachicouras, N., Miller, J., Lacour, S., Brown, M.C., and Lee, D.J. (2019). Auditory Brainstem Implants: Recent Progress and Future Perspectives. Frontiers in neuroscience *13*, 10.
Xie, R., and Manis, P.B. (2013). Target-Specific IPSC Kinetics Promote Temporal Processing in Auditory Parallel Pathways. The Journal of Neuroscience *33*, 1598-1614.
Xie, R., and Manis, P.B. (2014). GABAergic and glycinergic inhibitory synaptic transmission in the ventral cochlear nucleus studied in VGAT channelrhodopsin-2 mice. Frontiers in neural circuits *8*, 84.
Xie, R., and Manis, P.B. (2017). Radiate and Planar Multipolar Neurons of the Mouse Anteroventral Cochlear Nucleus: Intrinsic Excitability and Characterization of their Auditory Nerve Input. Frontiers in neural circuits *11*, 77.
Yaeger, D.B., and Trussell, L.O. (2015). Single granule cells excite Golgi cells and evoke feedback inhibition in the cochlear nucleus. J Neurosci *35*, 4741-4750.
Yang, H., and Xu-Friedman, M.A. (2008). Relative roles of different mechanisms of depression at the mouse endbulb of Held. Journal of neurophysiology *99*, 2510-2521.
Yang, Y., Ramamurthy, B., Neef, A., and Xu-Friedman, M.A. (2016). Low Somatic Sodium Conductance Enhances Action Potential Precision in Time-Coding Auditory Neurons. J Neurosci *36*, 11999-12009.
Yaylaoglu, M.B., Titmus, A., Visel, A., Alvarez-Bolado, G., Thaller, C., and Eichele, G. (2005). Comprehensive expression atlas of fibroblast growth factors and their receptors generated by a novel robotic in situ hybridization platform. Dev Dyn *234*, 371-386.
Yin, T.C.T., Smith, P.H., and Joris, P.X. (2019). Neural Mechanisms of Binaural Processing in the Auditory Brainstem. Comprehensive Physiology *9*, 1503-1575.
Young, E.D. (1998). Parallel processing in the nervous system: evidence from sensory maps. Proceedings of the National Academy of Sciences of the United States of America *95*, 933-934.
Yu, F.H., and Catterall, W.A. (2003). Overview of the voltage-gated sodium channel family. Genome Biol *4*, 207.
Zeilhofer, H.U., Studler, B., Arabadzisz, D., Schweizer, C., Ahmadi, S., Layh, B., Bösl, M.R., and Fritschy, J.M. (2005). Glycinergic neurons expressing enhanced green fluorescent protein in bacterial artificial chromosome transgenic mice. The Journal of comparative neurology *482*, 123-141.
Zeng, H., and Sanes, J.R. (2017). Neuronal cell-type classification: challenges, opportunities and the path forward. Nature Reviews Neuroscience *18*, 530-546.
Zhao, Y., Chen, S., Swensen, A.C., Qian, W.J., and Gouaux, E. (2019). Architecture and subunit arrangement of native AMPA receptors elucidated by cryo-EM. Science *364*, 355-362.
Zheng, G.X., Terry, J.M., Belgrader, P., Ryvkin, P., Bent, Z.W., Wilson, R., Ziraldo, S.B., Wheeler, T.D., McDermott, G.P., Zhu, J.*, et al.* (2017). Massively parallel digital transcriptional profiling of single cells. Nat Commun *8*, 14049.
Zou, A., Lin, Z., Humble, M., Creech, C.D., Wagoner, P.K., Krafte, D., Jegla, T.J., and Wickenden, A.D. (2003). Distribution and functional properties of human KCNH8 (Elk1) potassium channels. Am J Physiol Cell Physiol *285*, C1356-1366.

Supplemental materials

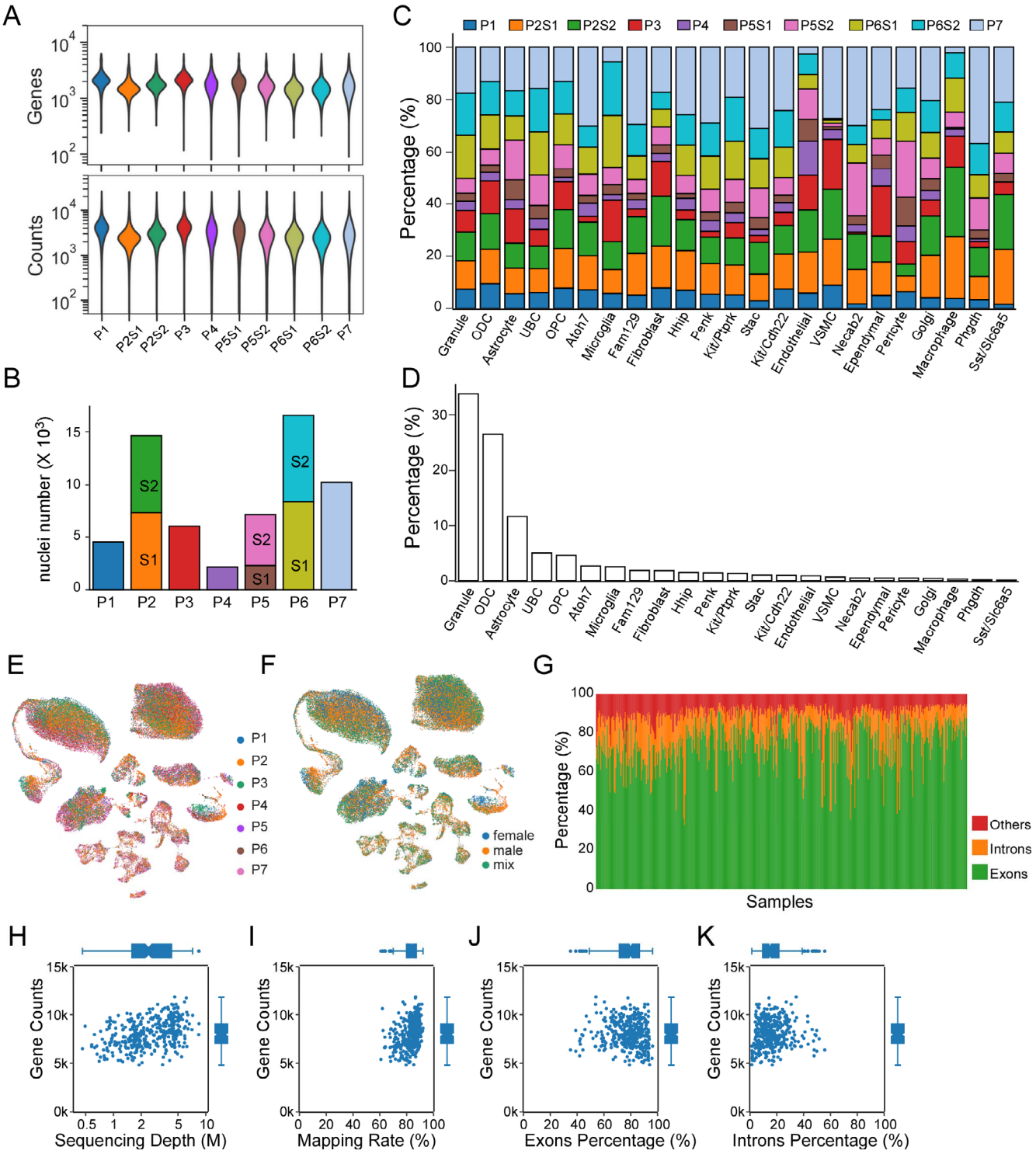

Data S1. Quality control analysis for snRNA-seq and Patch-seq data. Related to Figures 1-2. (A) Violin plots of the gene counts (top) and UMI counts (bottom) of each sample sequenced with Drop-seq. P1, P3, P5, P7: the sample from Preparation 1, 3, 5, and 7 respectively. P2S1 and P2S2: Sample 1 and 2 from Preparation 2; P5S1 and P5S2: Sample 1 and 2 from Preparation 5; P6S1 and P6S2: Sample 1 and 2 from Preparation 6. **(B)** Sample size (the number of nuclei) of each preparation and sample in snRNA-seq. Preparation 2, 5, and 6 has two samples (S1, S2). **(C)** The contribution of

each sample (represented as a percentage) to the total population of each cell type (or cluster). See Figure 1 and Figure S1 for annotation of cell types and clusters. **(D)** The proportion of each cell type (or cluster) in the total sequenced population (i.e., combining all samples). **(E)** UMAP visualization of all nuclei from CN, colored by preparations (P1-P7). **(F**) UMAP visualization of all nuclei from CN, colored by gender. **(G)** The proportion of sequencing reads mapped to exons (CDS, 5'UTR, 3'UTR), introns, and other intergenic regions in each Patch-seq cell. As expected, most reads map to exons regions rather than introns and intergenic regions. **(H**) Correlations of gene counts with sequencing depth in Patch-seq cells. **(I)** Correlations of gene counts with STAR mapping rate in Patch-seq cells. **(J)** Correlations of gene counts with the percentage of reads mapped to exons in Patch-seq cells. (**K)** Correlations of gene counts with the percentage of reads mapped to introns in Patch-seq cells.

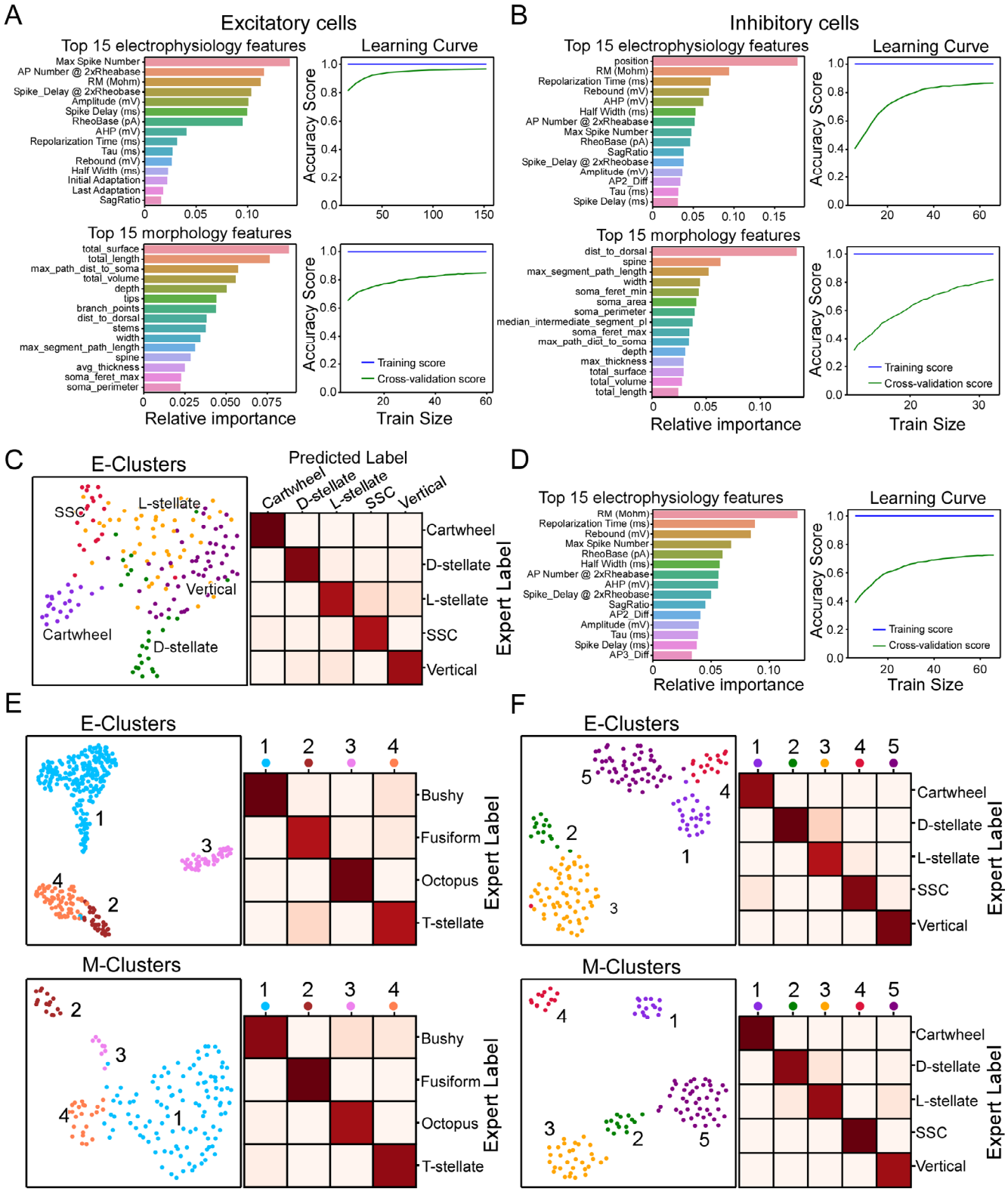

Data S2. Distinguish cell types by electrophysiological or morphological features. Related to Figure 2, 6

(A) Left: Weights of the top 15 electrophysiological (top) or morphological (bottom) features contributing to the overall performance of the cell type classifier (for excitatory cell types). Right: The performance of the classifier trained with electrophysiological (top) or morphological (bottom) features. Note: its performance improves as the training dataset size increases, indicating a good cell

type classifier. **(B)** Left: Weights of top 15 electrophysiological (top) or morphological (bottom) features contributing to the overall performance of the cell type classifier (for inhibitory cell types). Right: The performance of the classifier trained with electrophysiological (top) or morphological (bottom) features. The performance with electrophysiological features is weighted in with location supervision. **(C)** Left: UMAP visualization of CN inhibitory neurons (n=163) clustered by selected electrophysiological features (without location supervision). Each cell type is colored as in Figure 2C. Right: Confusion matrix shows the performance (an average of 86.18% accuracy) of the cell-type classifier trained with electrophysiological features only (without location supervision). **(D)** Right: Weights of the top 15 electrophysiology features contributing to the overall performance of the cell-type classifier (for inhibitory cell types). Right: The performance of the classifier trained with electrophysiological features only (without location supervision). **(E)** Top left: UMAP visualization of 404 CN excitatory neurons clustered by selected electrophysiological features, colored by k-means clusters. Top right: Confusion matrix shows the performance of k-means clustering (with electrophysiological features) in distinguishing CN excitatory cell types as labeled manually (an average of 92.33% accuracy). Bottom left: UMAP visualization of 157 CN excitatory neurons clustered by selected morphological features, colored by k-means clusters. Bottom right: Confusion matrix shows the performance of k-means clustering (with morphological features) in distinguishing CN excitatory cell types (an average of 92.99% accuracy). **(F)** Top left: UMAP visualization of 163 CN inhibitory neurons clustered by selected electrophysiological features, colored by k-means clusters. Top right: Confusion matrix shows the performance of k-means clustering (with electrophysiological features) in distinguishing CN inhibitory cell types as labeled manually (an average of 90.18% accuracy). Bottom left: UMAP visualization of 95 CN inhibitory neurons clustered by selected morphological features, colored by k-means clusters. Bottom right: Confusion matrix shows the performance of k-means clustering (with morphological features) in distinguishing CN inhibitory cell types (an average of 90.53% accuracy).

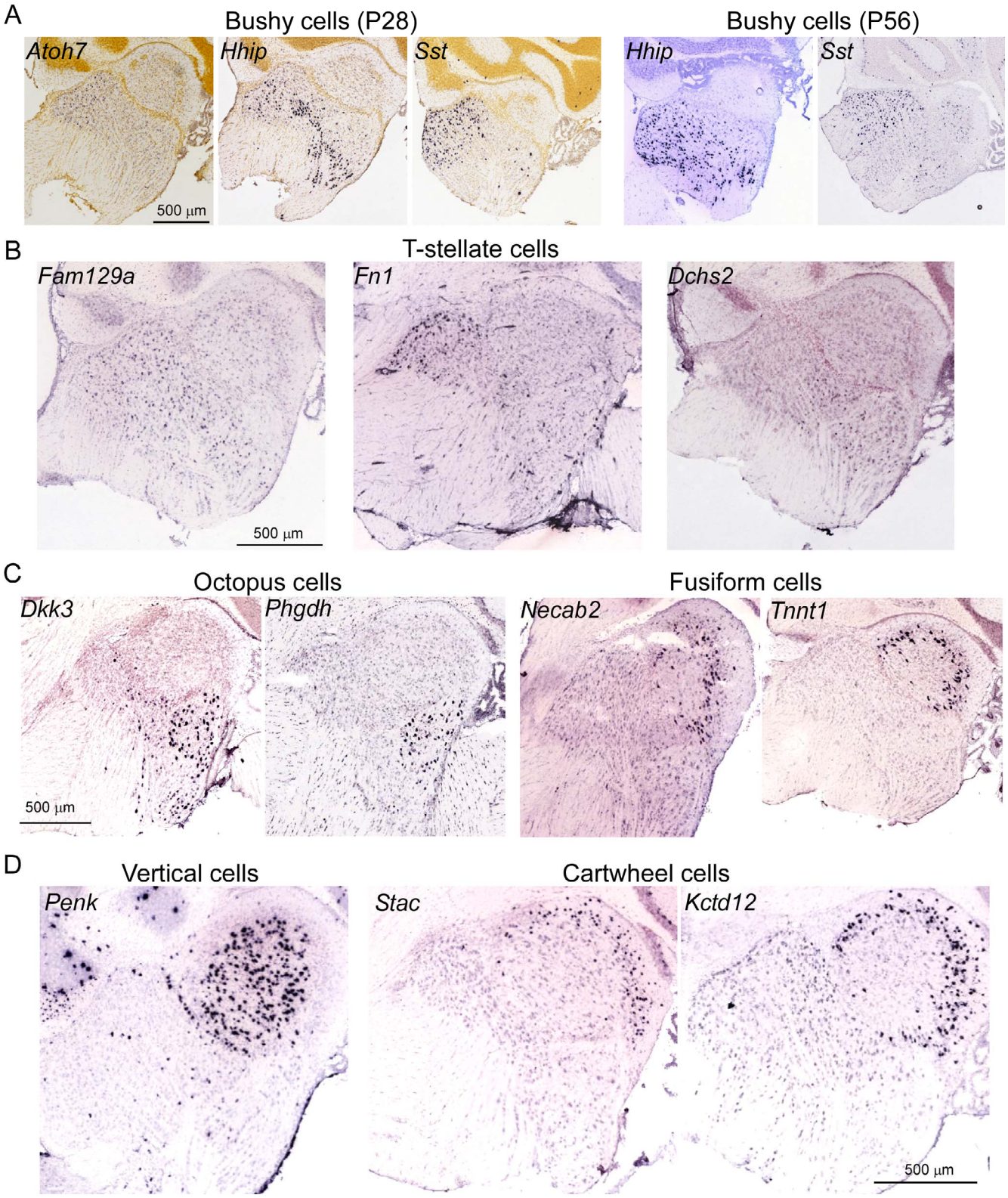

Data S3. Allen Brain Atlas ISH expression of single discriminatory markers for major CN cell types. Related to Figures 3-6.

(A) Representative micrographs of ISH expression of single discriminatory markers (*Atoh7*, *Hhip,* and *Sst*) for bushy cell subtypes in sagittal sections containing CN (corresponding to middle CN) at P28 (left) and P56 (right). The expression data of *Atoh7* at P56 are not available. **(B)** Representative micrographs of ISH expression of *Fam129a*, a general discriminatory marker for T-stellate cells

(right), and of the subtype-specific markers (*Fn1* and *Dchs2*) in the CN sagittal sections. **(C)** Representative micrographs of ISH expression of single discriminatory markers (*Dkk3* and *Phgdh*) for octopus cells or single discriminatory markers for fusiform cells (*Necab2* and *Tnnt1*) in the CN sagittal sections. **(D)** Representative micrographs of ISH expression of single discriminatory marker for vertical cells (*Penk*, Left) or for cartwheel cells (*Stac* and *Kctd12*) in CN sagittal sections. Image credit for all ISH images: Allen Institute.

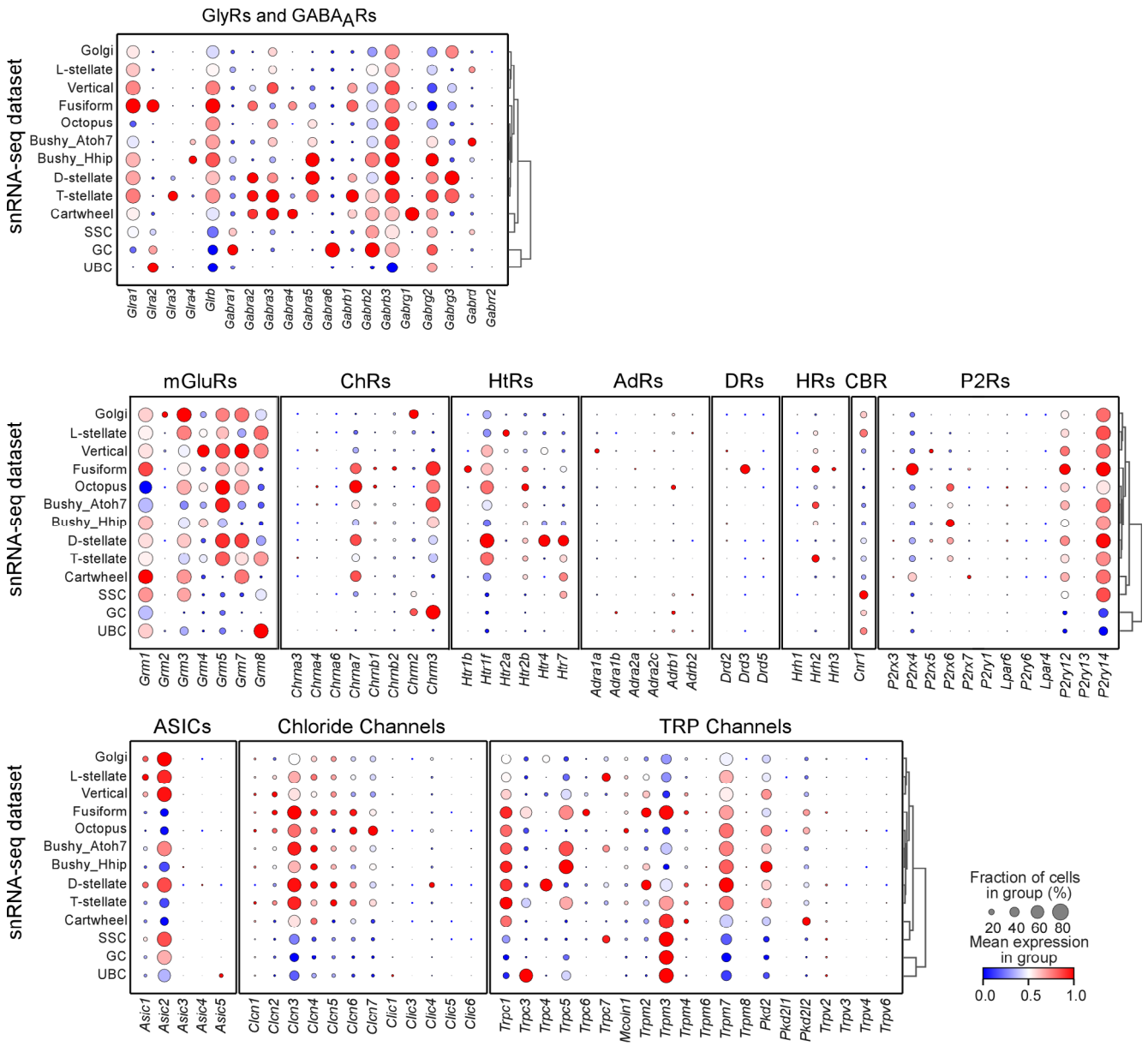

Data S4. The expression of GABA$_A$ receptor, glycine receptors, metabotropic receptors, and ion channels in CN. Related to Figures 7 and S7.

(Top) Dot plot showing scaled expression of the genes encoding glycine and GABA$_A$ receptors (from snRNA-seq dataset).

(Middle) Dot plot showing scaled expression of the genes encoding metabotropic glutamate receptors (mGluR), cholinergic receptors (ChRs), serotonergic receptors (HtRs), adrenergic receptors (AdRs), dopaminergic receptors (DRs), histaminergic receptors (HRs), cannabinoid receptors (CBR), and purinergic receptors (P2Rs) across CN cell types (from snRNA-seq dataset). The Patch-seq data (not shown) generally agree with snRNA-seq data but detected a higher expression of several receptors in additional cell types, consistent with the more sequencing depth in Patch-seq compared to the 10X drop-seq protocol.

(Bottom) Dot plot showing scaled expression of the genes encoding acid-sensing ion channel (ASICs), chloride channels, and transient receptor potential (TRP) channels across CN cell types (from snRNA-seq dataset).

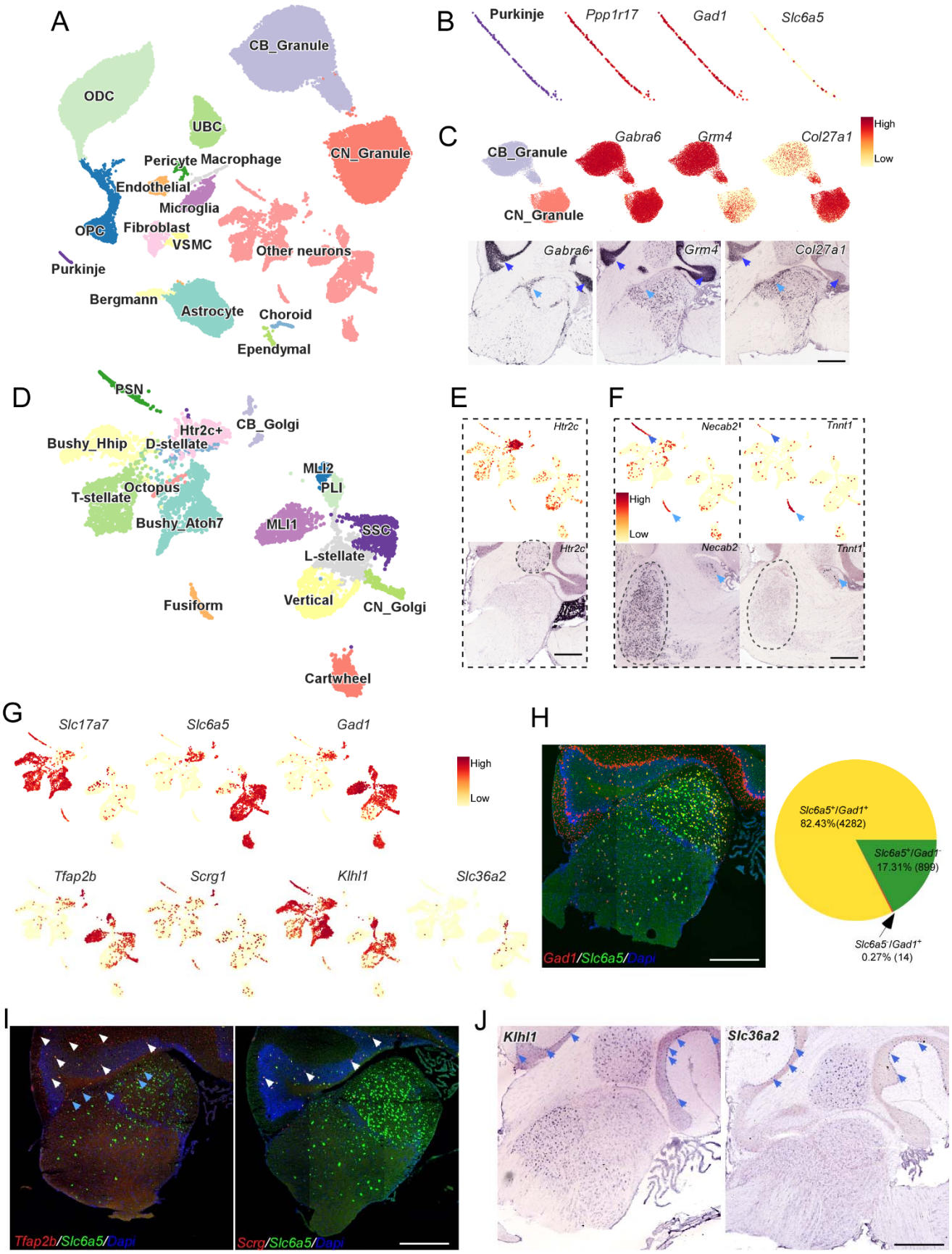
A
CB_Granule
ODC
UBC
CN_Granule
Pericyte
Macrophage
Endothelial
Microglia
OPC
Fibroblast
VSMC
Other neurons
Purkinje
Bergmann
Astrocyte
Choroid
Ependymal
B
Purkinje
Ppp1r17
Gad1
Slc6a5
C
CB_Granule
Gabra6
Grm4
Col27a1
High
Low
CN_Granule
Gabra6
Grm4
Col27a1
D
PSN
CB_Golgi
Htr2c+
Bushy_Hhip
D-stellate
MLI2
PLI
Octopus
T-stellate
Bushy_Atoh7
MLI1
SSC
L-stellate
Fusiform
Vertical
CN_Golgi
Cartwheel
E
Htr2c
Htr2c
F
Necab2
Tnnt1
High
Low
Necab2
Tnnt1
G
Slc17a7
Slc6a5
Gad1
High
Low
Tfap2b
Scrg1
Klhl1
Slc36a2
H
Gad1/Slc6a5/Dapi
Slc6a5+/Gad1+
82.43%(4282)
Slc6a5+/Gad1-
17.31% (899)
Slc6a5-/Gad1+
0.27% (14)
I
Tfap2b/Slc6a5/Dapi
Scrg/Slc6a5/Dapi
J
Klhl1
Slc36a2

Method S1. Identification of cell populations from adjoining brain tissues. Related to Figures 1, S1.

(A) UMAP visualization of 93,644 nuclei (after quality control) reveals major cell types and clusters from the cochlear nuclei (CN) and neighboring cerebellum (CB). Cell type and cluster identity is color coded. Identification of cell types and clusters from CB, including cerebellar granule cells (CB_Granule), Purkinje cells, and Bergmann cells was based on their previously-identified molecular signatures (Kozareva et al. 2021) and ISH data from Allen Brain Atlas. **(B)** UMAP visualization of the expression of *Ppp1r17*, *Gad1*, and *Slc6a5* in the cluster as labeled as Purkinje in (A). **(C)** Top: UMAP visualization of the expression of *Gabra6*, *Grm4*, and *Col27a1* in two clusters assigned to granule cells in (A) reveals a granule cell population from CB (CB_Granule) (i.e., *Grm4*$^+$/*Col27a1*$^-$, Kozareva et al. 2021). Bottom: Representative Allen Brain Atlas micrographs of ISH expression of Gabra6, Grm4, and Col27a1 in representative sagittal sections containing the CN and CB indicate that granule cells in CN (CN_Granule) could be discriminated from CB granule cells (CB_Granule) by their lack of *Grm4* expression. Note: Dark blue arrows point to granule cell layers in CB and light blue arrows point to granule cell layers in CN. Image credit for all ISH images: Allen Institute. **(D)** Subclustering of the neuronal population (except for granule cells and UBC) reveals distinct neuronal clusters from the CN and adjoining regions including CB, the principal sensory nucleus of the trigeminal nerve (PSN), and the dentate nucleus. Cell type and cluster identity is color coded. Identification of neuronal clusters from CB, PSN and the dentate nucleus is based on identified molecular signatures of CB cell types (Kozareva et al. 2021) and ISH data from Allen Brain Atlas. **(E)** Top: UMAP visualization of the expression of *Htr2c* reveals a *Htr2c*-enriched cluster corresponding to cells from the dentate nucleus. Bottom: A representative micrograph (from Allen Brain Atlas) of ISH expression of *Htr2c* in a sagittal section containing CN and CB shows that *Htr2c* expression is restricted to the dentate nucleus (dash circle). **(F)** Top: UMAP visualization of the expression of *Necab2* and *Tnnt1* reveals two *Necab2*-enriched clusters, one of which corresponds to cells from the PSN (*Necab2*$^+$/*Tnnt1*$^-$ cluster). Bottom: Micrograghs of ISH expression of *Necab2* (right) or *Tnnt1* (left) in a sagittal section containing a small region of DCN and PSN show that *Necab2*$^+$/*Tnnt1*$^-$ cells are restricted to the PSN (dash circles), while *Necab2*$^+$/*Tnnt1*$^+$ cells (light blue arrows) are restricted to the DCN (i.e., fusiform cells; see Figure 2) **(G)** UMAP visualization of the expression of gene markers for excitatory neurons (*Slc17a7*), for inhibitory neurons (*Gad1* and *Slc6a5*), for CB interneuron cell types (*Tfap2b*, *Scrg1*, *Klhl1*, and *Slc36a2*) reveals four *Tfap2b*-enriched inhibitory clusters, and one inhibitory cluster co-enriched with Klhl1 and Slc36a2. Two of *Tfap2b*-enriched clusters are pure GABAergic (*Gad1*$^+$/*Slc6a5*$^-$), which correspond to MLI1 and MLI2 from the CB (Kozareva et al. 2021, also see below). The other two *Tfap2b*-enriched are glycine/GABA combinatorial clusters (*Scrg1*$^+$or *Scrg1*$^-$), which correspond to Golgi cells in the CB (CB_Golgi, Kozareva et al. 2021, also see below) and CN (CN_Golgi, also see below). An inhibitory cluster is co-enriched with *Klhl1* and *Slc36a2*, reminiscent of PLI in the CB (Kozareva et al. 2021). **(H)** Left: Double FISH staining of Gad1 and Slc6a5 in a sagittal section containing CN and CB. Right: Pie chart indicates the proportion of pure GABAergic neurons (*Gad1*$^+$/*Slc6a5*$^-$), pure glycinergic neurons (*Gad1*$^-$/*Slc6a5*$^+$), and glycine/GABA neurons (*Gad1*$^+$/*Slc6a5*$^+$). Note: *Gad1*$^+$/*Slc6a5*$^-$ neurons in the CN are absent or very sparse. **(I)** Double FISH staining of Golgi cell marker gene (*Tfap2b* or *Scrg1*) and *Slc6a5* in representative sagittal sections containing CN and CB. Note: *Scrg1* expression is restricted to the CB. White arrows indicate the gene expression in CB and light blue arrows indicate the expression in CN. **(J)** Representative micrographs (from Allen Brain Atlas) of ISH expression of *Klhl1* and *Slc36a2* (CB PLI marker gene) in the sagittal section containing the CN and CB. Note: *Slc36a2* is not expressed in CN. Arrows indicate the gene expression in CB Purkinje cell layer.

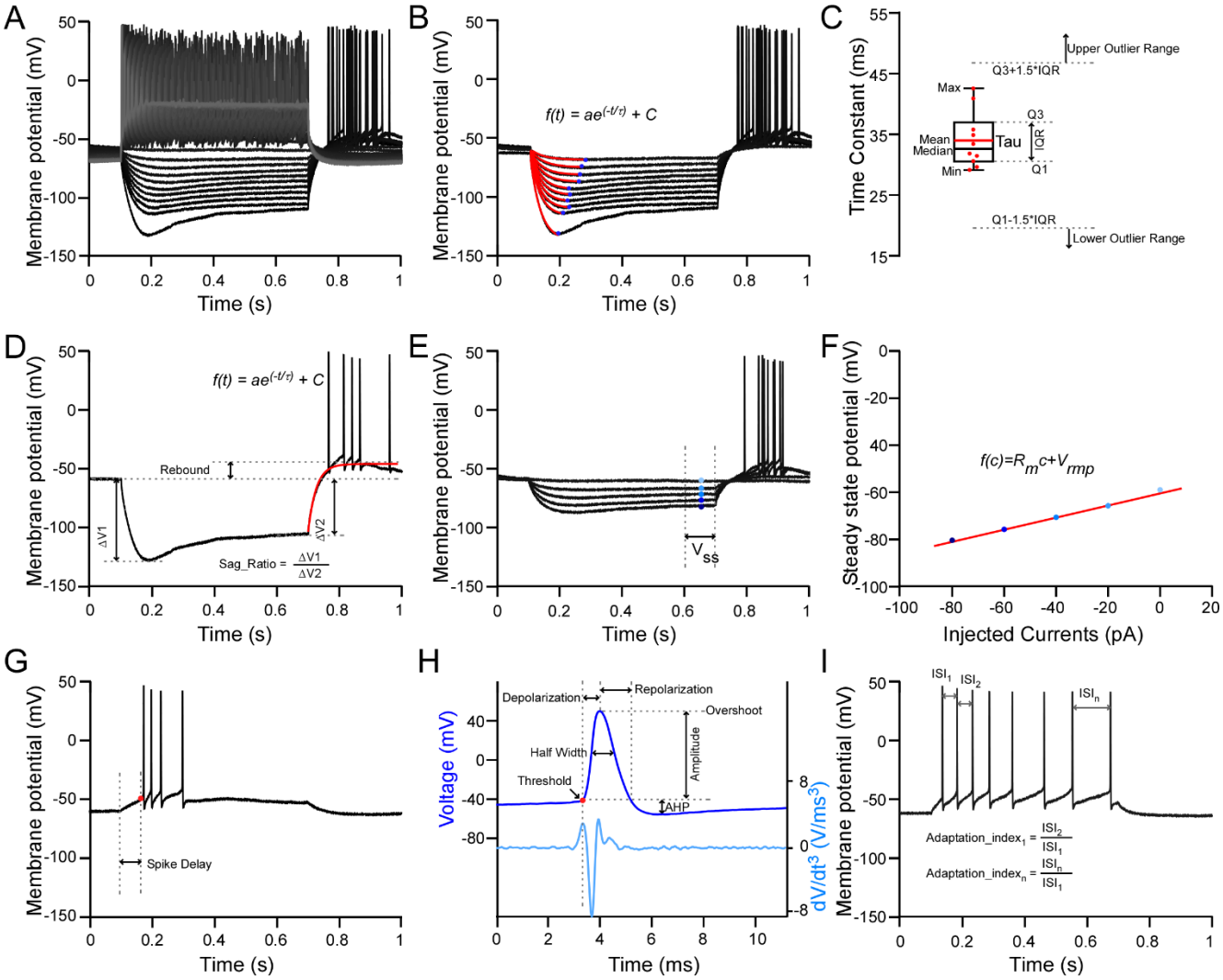

Method S2. Extraction of the electrophysiological features. Related to Figures 2, 4-6
(**A**) Membrane potential responses of an example neuron to the consecutive step current injections. (**B**) A series of membrane potential traces in response to hyperpolarizing current steps are fitted with an exponential function. The tau (t) is calculated for each trace. (**C**) A box plot shows a series of Tau values from one sample neuron, including maximum (Max), minimum (Min), mean, median, the first quartile (Q1), the third quartile (Q3), the interquartile range (IQR) values. The Tau values falling above the upper range (> Q3+1.5*IQR) or below the low range (< Q1-1.5*IQR) are considered outliers and removed before averaging for the mean value. (**D**) The first hyperpolarizing trace in the step protocol is used to calculate the sag ratio and rebound voltage as shown with inset equations. (**E**) The membrane potential responses to the last five negative current injections in the step protocol. The steady-state potential for each trace (V_{ss}) is indicated with dash lines. (**F**) The steady-state potentials (V_{ss}) are fitted with a linear function by the injected currents. The rest membrane potential (V_{rmp}) and input resistance (R_m) are calculated with the inset equation. (**G**) A representative trace with action potentials (AP) evoked during consecutive step current injections. Spike delay is defined as a time duration between two dash lines. (**H**) A representative AP trace (top) and its third derivative (dV/dt^3, bottom). The AP threshold is the membrane potential where the third derivative of the AP trace is maximal, as indicated with a red dot. AP depolarization time, AP amplitude, AP repolarization time,

AP half-width, and the afterhyperpolarization (AHP) amplitude are defined as shown with double-arrow lines and dash lines. (**I**) The membrane potential trace in response to 2x rheobase current injection. The initial (adaptation_index1) and last adaptation index (adaptation_index2) are calculated with inset equations after the interspike interval (ISI) between each AP is determined.

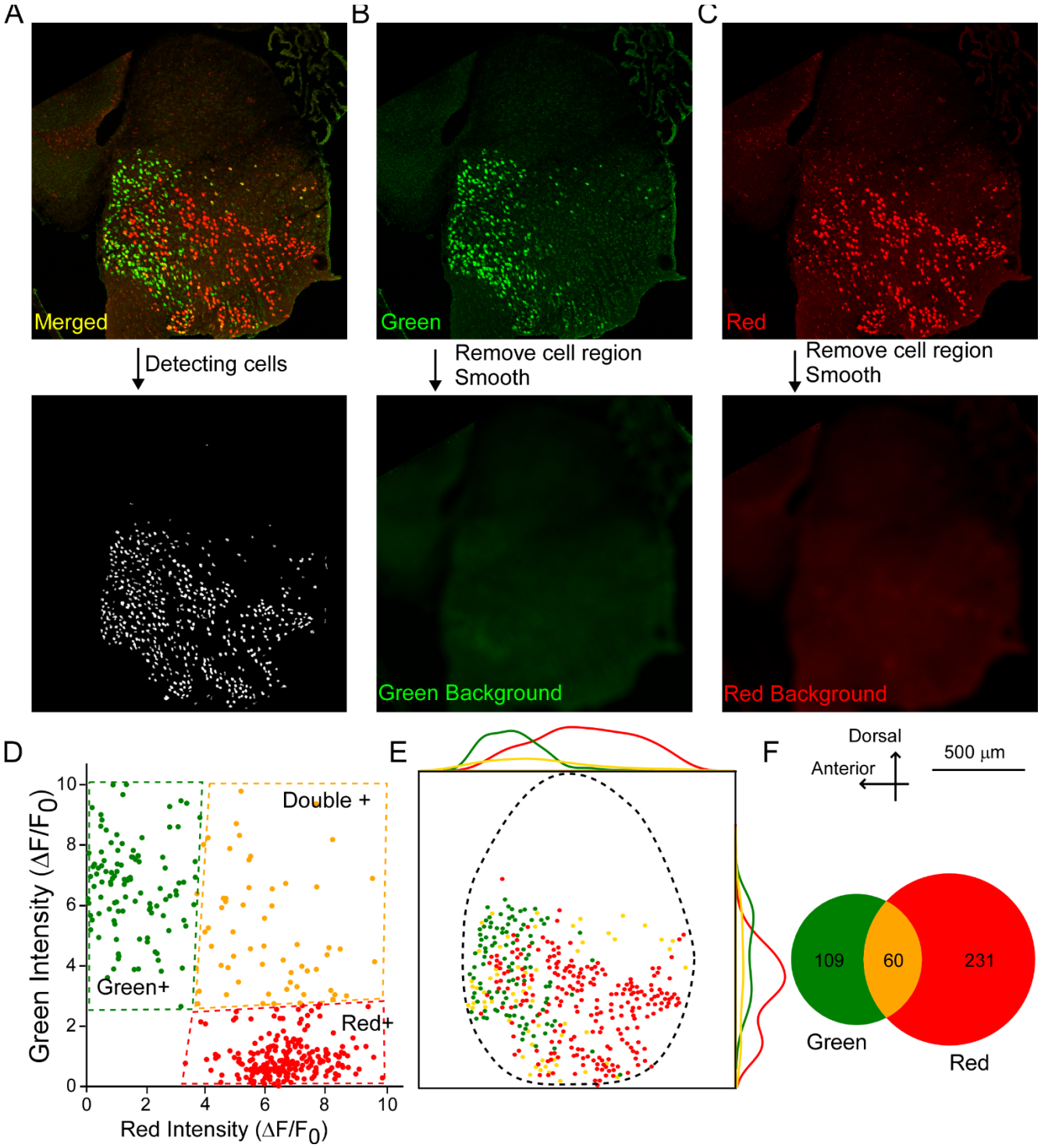

Method S3. Analysis of dual-color fluorescence in situ hybridization (FISH). Related to Figures 3-6

(**A**) Top: A representative dual-color FISH staining image (merged). Green channel represents the FITC-labeled RNA probe and red channel represents the DIG-labeled RNA probe. Bottom: each cell with green and/or red signals (F) is detected with a custom-made IDL code, as indicated with a white dot. (**B**) Top: A green signal-only image. Bottom: the image indicates the background green signals (Green F_0), derived by subtracting the signals of detected cells from the images on the top, smoothed by a 60 μm length window. (**C**) Top: A red signal-only image. Bottom: the image indicates the background red signals (Red F_0), derived by subtracting the signals of detected cells from the images

on the top, smoothed by a 60 μm length window. (**D**) A 2-D scatter plot: the intensity differences (ΔF) between F and F0 divided by F0 of a detected cell from one channel (ΔF/F0) are plotted against ΔF/F0 from another channel. Quadrilateral gates are drawn on the plot to determine whether a cell was single-labeled or double-labeled. (**E**) Each identified cells (Red^+, $Green^+$, or $Double^+$) in their real CN anatomic location, and 2-D density histograms are plotted through the anterior to posterior and dorsal to the ventral axis to show the distribution of Red^+, $Green^+$, and $Double^+$ cells along the two axes. (**F**) Venn diagrams show the number of Red^+, $Green^+$, and $Double^+$ cells in the images shown in A.